DEVELOPMENT OF A ROTOR MODEL FOR THE NUMERICAL SIMULATION OF HELICOPTER EXTERIOR FLOW-FIELDS

by

Paul Hotchkiss

Dissertation presented for the degree of Master of Science in the Department of Mechanical Engineering at the University of Cape Town

Supervisors:

Dr C.J. Meyer

Prof. T.W. von Backström

Department of Mechanical Engineering

University of Cape Town

South Africa

August 2004

Declarations

(i) I hereby grant the University of Cape Town free licence to reproduce for the purpose of research either the whole or any portion of the contents in any manner whatsoever of the above dissertation. I am presenting this dissertation in partial fulfilment of the requirements for my degree.

(ii) I know the meaning of plagiarism and declare that all of the work in the document, save for that which is properly acknowledged. is my own.

SIGNATURE : Signed by candidate

DATE : 31 AUGUST 2004

Objectives

The aim of this dissertation is to develop and validate a numerical rotor model suitable for use in modeling the exterior flow-field of a helicopter, including the rotor downwash. The model should be suitable for simulations of the helicopter in hover, vertical and forward flight. Objectives which need to be met during this process may be summarized as follows:

- Formulate and describe an appropriate numerical modeling methodology for representing a rotor, or axial-fan, in a CFD code
- Write a computer code based on the described modeling methodology
- Implement the coded rotor model in a CFD code, modeling both axially aligned and non-aligned flow into an axial-flow fan, and validating the numerical results against experimental data
- Implement the rotor model in the qualitative analysis of the flow field around a helicopter

Abstract

A numerical methodology is developed to model the effect of a rotor on the surrounding flow-field. The model calculates the time-averaged aerodynamic forces exerted on the air by the fan blades within the blade-swept region, and permits the user to specify blade properties such as cross-sectional profile and orientation at a particular radial and azimuthal location. The calculated forces are included as source terms within the Reynolds-averaged Navier-Stokes equations for an incompressible fluid, which are solved by the commercial CFD solver, FLUENT. The effects of turbulence are incorporated through the use of Launder and Spalding's k-ε turbulence model. This method is selected as being the most efficient use of the resources available, giving the economical advantages of a steady simulation, while allowing radial and azimuthal variations of rotor characteristics.

In order to validate the accuracy of the numerical model for both aligned and non-aligned inflow conditions, results are compared with experimental data reported for an axial flow fan. Agreement between experimental and numerical results is excellent to good. Fan static pressure rise is closely predicted by the numerical solution, while fan power consumption and fan static efficiency are under and over-predicted respectively. This error may be attributed to frictional losses not accounted for in the numerical model. These include physical rotational instabilities, leading to increased mechanical losses, and tip effects due to the clearance between the fan blade tips and the fan casing. Trends are nevertheless consistently predicted by the numerical model for inflow angles up to 45°, and for the range of blade pitch settings used. The adverse effect of off-axis inflow on the fan static pressure rise is numerically predicted, while fan power consumption is found to remain independent of inflow angle, as had been experimentally observed.

The rotor model is finally integrated with the fuselage of the CIRSTEL (Combined Infra-Red Suppression and Tail rotor Elimination) prototype in an analysis of the helicopter exterior flow-field. No experimental data for this configuration was available for validation purposes. However, the model is used in the simulation of several common helicopter flight conditions. Results are presented graphically, and generally indicate good agreement with physically observed phenomena.

Acknowledgements

I would like to express my thanks and gratitude towards the following individuals and institutions for contributing towards this work

- Mary, my wife, who has given me motivation and encouragement throughout
- Dr. Chris Meyer, my supervisor, whose guidance has shaped the form and nature of this work.
- Prof. von Backström, my supervisor, whose insightful observations have added to the value of this work
- René Heise, for providing the CIRSTEL helicopter geometry used in this work
- Nick Gibson, for providing technical support in the CFD lab
- The CFD research group, for providing the resources that made this work possible

Table of Contents

List of Illustrations

List of Tables

Nomenclature

Symbols

A	Area, m^2
A_0	Root pitch angle (collective pitch), °
A_1	Cyclic pitch constant
$\overline{B_t}$	Blade element tangent-forward orientation vector
$\overline{B_n}$	Blade element normal- upward orientation vector
B_1	Cyclic pitch constant
C	Constant
C_d	Airfoil drag coefficient
C_l	Airfoil lift coefficient
C_ε	κ–ε Turbulence model constants
C_μ	κ–ε Turbulence model constant
c	Chord, m
d	Diameter, mm
D	Drag force, N
g	Gravitational acceleration, m/s^2
k	Turbulent kinetic energy per unit volume, m^2/s^2
L	Lift force, N
$\bar{n}$	Rotor plane unit normal vector
N	Rotor/fan rotation speed, rpm
p	Pressure, N/m^2
P_R	Power consumption of axial flow fan, Nm/s
P_{Fs}	Static pressure rise of axial flow fan, N/m^2
Q	Rotor torque, Nm
$\bar{r}$	Blade element radial position, or radial unit vector, m
R	Rotor radius, m
Re	Reynolds number
S	Source term
$\bar{t}$	Blade unit tangent vector
t	Rotor disk thickness, m, or time, s
T	Rotor thrust, N

$\bar{v}$	Velocity vector, m/s
V	Volume flow rate, m^3/s

Greek Symbols

α_t	Blade angle of twist at tip, °
α_e	Effective angle of attack, °
δr	Blade element radial dimension, m
ε	Rate of dissipation of turbulent kinetic energy per unit volume, m^2/s^3
γ	Geometric angle of attack, ° or rad
η_{Fs}	Static efficiency of axial flow fan, %
ψ	Azimuth angle, ° or rad
μ	Molecular dynamic viscosity, $N.s/m^2$
ρ	Density, $kg.m^{-3}$
σ	Solidity ratio
τ_{ij}	Stress tensor, N/m^2
$\overline{\Omega}$	Rotor rotation vector, rad/s

Subscripts

1,2,...	Coordinate system
d	Drag
e	Effective
FC	Fan Casing
FH	Fan Hub
Fs	Fan static conditions
Ft	Fan total conditions
i	i-index, or inlet
j	j-index
k	k-index
l	Lift
n	Normal
o	Outlet
rel	Relative
t	Tangential, total, or turbulent

1 AN OVERVIEW OF ROTARY-WING MODELLING TECHNIQUES

During a development stretching back several decades, various techniques have been suggested for the modeling of rotary-wing flow fields. Early attempts to describe the rotor characteristics were based on momentum theories, while the rotor wake was usually approximated with various classical and prescribed vortex theories. In more recent times, the availability of powerful computers has permitted the use of Computational Fluid Dynamics (CFD) to solve increasingly complex flow problems. At this time however, a complete solution of the rotor flow-field, using the unsteady, turbulent, three dimensional Navier-Stokes equations, remains prohibitively expensive. The present method therefore reduces the problem to a steady one, combining momentum and blade element theories to model the rotor as an actuator disk, while solving the steady, incompressible, viscous, Reynolds-averaged conservation equations for the exterior flow-field.

1.1 One Dimensional Momentum Methods

Early attempts to model helicopter rotor characteristics were based on one dimensional momentum theory developed for aeroplane propellers. The rotor is considered to be an infinitely thin actuator disk, generating a uniform induced velocity, v_i, at the rotor disk [1]. Although this method allowed basic simulation of rotor performance characteristics such as thrust and torque, and was later improved by accounting for rotation in the wake, it is deficient in two very important aspects: momentum theory assumes uniform flow in the rotor wake, with no facility for defining azimuthal variations; and it makes no provision for information about the characteristics of the rotor blades. For these reasons, one dimensional (1D) momentum theories are not suitable for any but the most basic of simulations.

1.2 Wake Methods

Classic vortex theories were introduced in early attempts to model wakes induced by a rotary wing. Potential flow is usually assumed, with the rotor blade being represented

by a system of bound and trailing vortices, and the wake by a rigid non-contracting helical vortex sheet. According to Rajagopalan and Mathur [2], results obtained by this method were satisfactory for cases such as an aeroplane in cruise. However, for cases where the velocity induced by the rotor was much greater than the free-stream, such as a helicopter in hover, the results were poor.

Prescribed wake methods were introduced in an attempt to improve the classical vortex methods with the aid of experimental data. These methods use experimental observations to relate the vortex structure to the rotor-blade geometry and rotor performance coefficients. The limitation with this approach is that the flight conditions being modelled need to be similar to the experimental conditions under which the wake data was obtained.

A more recent approach is the use of free wake methods, which allow the wake to develop iteratively, based on physical constraints. Rajagopalan and Mathur [2] state that these methods do not have the limitations of prescribed wake methods, and may thus be used in a greater range of problems. However, they also caution that for conventional geometries, free wake methods provide no greater accuracy than prescribed wake methods.

Recently, further developments in the field of wake prediction have allowed modelling of unsteady wake effects in time-dependent rotor simulations. Le Bouar et al. [3] reported the use of a relaxation method to compute the free wake geometry, coupled with an unsteady lifting-line method. Lifting-line methods usually follow the quarter chord line path of each blade, with aerodynamic moments and loads being read directly from 2D airfoil tables.

The major shortfall of wake methods in general, is the assumption of potential flow. Important features of the flow, such as the tip vortices, cannot be easily described, since vorticity cannot be defined within the governing transport equations. Despite these limitations, wake methods remain valuable tools for rotor modelling, largely due to their ability to predict major flow characteristics in a cost efficient manner.

1.3 Numerical Methods

Computational Fluid Dynamics describes a relatively new discipline in fluid dynamics, made possible by the increasing power and availability of computing resources. The basis of this technique is the use of some form of discretisation scheme to permit the numerical solution of certain governing equations over the domain of interest. The governing equations may be chosen to suit the problem under investigation.

At this time, the use of the full, unsteady Navier-Stokes equations for fluid flow around the individual rotor blades is beyond the capacity of computing resources available to most CFD users. The high grid density required to capture flow data around the blades and in the wake, renders the process prohibitively expensive, especially since the analysis is an unsteady one.

Various approaches have been demonstrated as means of modelling the effects of a rotary-wing, without necessarily modelling the individual blades themselves. A method recently attempted is the use of the lifting-line concept coupled with an unsteady Euler or Navier-Stokes solver for the flow-field [4]. This approach permits many unsteady effects of the flow to be captured, while reducing the need for an overly dense mesh. However, the numerical cost of the analysis remains that of an unsteady one.

The need for a more efficient solution, while still retaining the ability to predict the characteristics of the rotor wake, has led many authors to use a time-averaged approach to model rotary-wing flow-fields. This method is greatly favoured in cases where the wake and its interactions are the primary focus for the investigation, with the exact flow around the individual blades of no direct significance.

While several approaches exist for representing time-averaged rotor effects, the fundamentals are commonly based on the calculation of aerodynamic loads directly from 2D blade-element theory. The most common methods used for accounting for the rotor's influence on the flow-stream, are the application of either internal boundary conditions, or momentum source terms, in the form of an actuator disk.

1.3.1 Internal Boundary Conditions

Several authors have used internal boundary conditions to represent a rotor in a time-averaged manner, commonly in the form of a disk-like pressure boundary, coupled with an induced swirl velocity. This approach was used by Fetjek and Roberts [5] to simulate the wing/rotor interaction for a tilt rotor in hover, using the thin-layer Navier-Stokes equations to describe the flow-field. In the region of the rotor, the computational domain was excluded from the implicit solution, with flow properties being updated explicitly with values calculated by an independent rotor model. This model was able to incorporate the effects of blade-geometry, airfoil aerodynamic characteristics, blade twist and pitch angles, and rotor rotational speed. These effects were described by distributions of local pressure rise through the actuator disk, and locally induced swirl velocity, and incorporated in the flow solution process at the internal boundaries.

Chaffin and Berry [6] modified this approach to represent the rotor with a disk-boundary of zero thickness (i.e. a disk-surface). Overset grids were used, permitting the rotor and fuselage geometry to be generated independently. The incompressible Navier-Stokes equations were solved for the flow-field, with compressibility effects included implicitly when determining the forces generated by the rotor-blades. The effect of the rotor was imposed on the flow solution using boundary conditions on the rotor-surface, describing the difference in pressure and tangential velocities between the upper and lower regions. This model included a trimming algorithm, matching the total rotor thrust to a prescribed value, and allowing the moments on the rotor to be balanced by adjusting the collective and cyclic pitch angles in an iterative manner during the solution process.

A very similar method was later developed by Lee and Kwon [7] to study rotor-fuselage aerodynamic interactions, this time using a 3D Euler solver based on unstructured meshes. The rotor effects were again imposed by use of internal boundary conditions in the actuator-disk region.

1.3.2 Momentum Sources

The use of momentum source terms to represent a rotor is less complicated than the application of internal boundary conditions. The region in which the rotor lies is included within the computational domain like any other region, the only difference being the inclusion of an additional term in each of the three momentum equations. This source term has units of force per unit volume, and may be calculated directly from the aerodynamic forces obtained using 2D airfoil look-up tables. The rotor is therefore represented simply by an actuator disk of finite thickness, whereby the rotor's influence is modelled in terms of the momentum it imparts to the fluid flowing though it.

Rajagopalan and Mathur [2] were early exponents of this theory in a rotary-wing application, the three dimensional analysis of a rotor in forward flight. The steady, incompressible, laminar Navier-Stokes equations were solved for the flow domain, the momentum source terms being explicitly added to the appropriate cells in the region of the actuator disk. Blade element theory was used to determine the aerodynamic loads with respect to radial and azimuth location, with blade pitch harmonics explicitly defined from experimental values, and with a constant blade cone angle.

Momentum source terms have also been used to represent the aerodynamic influence of fans and rotors in other applications. Combes and Marie [8] applied this concept to the study of a cross-flow fan, replacing the blade row action with a rotating force field by including a momentum source term in the governing Navier-Stokes equations. Further authors, who have used source terms to model the effect of various fans and propellers, are Pericleous and Patel [9], Schetz et al. [10], Thiart and Von Backström [11] and Löstedt [12]. More recently, Meyer and Kröger [13] modelled an axial flow fan using momentum source terms, incorporating several important features which form the basis for the present method.

Le Chuiton [14] investigated the use of both boundary condition and source term methods for rotor modelling in helicopter analyses. A variety of boundary methods were presented, all exhibiting degrees of numerical instability. A source term formulation was finally adopted, despite reported problems with numerical fluctuations in the region of the actuator disk, as providing the best compromise for study of the

helicopter exterior flow-field. These characteristics are notable in light of the findings presented in Appendix A, where a possible reason for such numerical fluctuations is discussed.

1.4 Present Method

The rotor model presented in this report is based on a representation of the rotor using momentum sources. As the main area of interest is not the rotor itself, but rather the downstream wake and its interaction with the helicopter fuselage, the problem is simplified by the use of time-averaged equations, reducing the numerical cost of the solution significantly.

The rotor model is coupled with a commercially available CFD code, *Fluent*, through the use of user defined functions, written in the C programming language. The region of the computational domain in which the rotor lies is defined using a structured grid, during construction of the geometry. Other regions may be meshed in an unstructured manner. Given the geometric details of the rotor, the momentum source terms are calculated by the rotor model, which receives flow data from the solver, calculates the aerodynamic loads from 2D blade element theory, and returns the source terms to the flow solver. The steady, incompressible, viscous, Reynolds-averaged conservation equations are solved.

At this stage, no rotor trimming algorithm is incorporated to achieve a pre-defined thrust value. Rather, the pitch harmonics are specified explicitly, as described by Rajagopalan and Mathur [2]

The modelling procedure itself is similar to that of Meyer and Kröger [13], but modified to incorporate the effects of azimuthal variations of blade geometry present in a helicopter rotor in forward flight. A feature of this model is the use of both upstream and downstream flow-field velocities to determine the relative velocity vector at the actuator disk. The reason for this is to reproduce as closely as possible the conditions under which the values in the 2D lift and drag airfoil tables are obtained. This arrangement was found to yield better results than if the flow-field velocity within the actuator disk was used to determine the relative velocity (see Appendix A).

Another feature of the model is the use of the lift and drag characteristics of a flat plate for angles of attack which fall outside the documented range of the airfoil. This permits the model to deal with reverse flow conditions over the rotor-blades, a realistic expectation when studying a helicopter rotor in forward flight.

Since the solution in the vicinity of the rotor itself is of no direct consequence, the present method is rather aimed at providing a realistic representation of the influence rotor on the surrounding flow-field, particularly the downwash, without a prohibitive investment of time and resources.

2 ROTOR MODEL FORMULATION

The present rotor model is greatly simplified by the use of a time averaged approach with a combination of 2D blade element and actuator disk theory. Two aspects need to be considered when implementing this technique. The regions in the computational domain where the rotor's influence is directly felt must be clearly specified, and the momentum source terms at these locations must be determined from the rotor and blade characteristics, and flow properties. In this chapter, the mathematical formulation of the rotor model, written in the C programming language, is described.

2.1 Rotor Discretisation

In the computational domain, the rotor is represented by a disk of finite thickness, corresponding to the physical dimensions of the disk described by a rotor-blade path. The disk is discretised by a number of regular annuli, which are further divided into elements, depicted in Figure 2-1. Blade properties, such as chord length, twist, thickness, and lift and drag characteristics, at the centre of each element, are assumed constant throughout that element. The region containing the actuator disk is defined during construction of the computational grid, and the particular elements to which the momentum sources are to be applied are identified by a linking algorithm during the solution initialisation process.

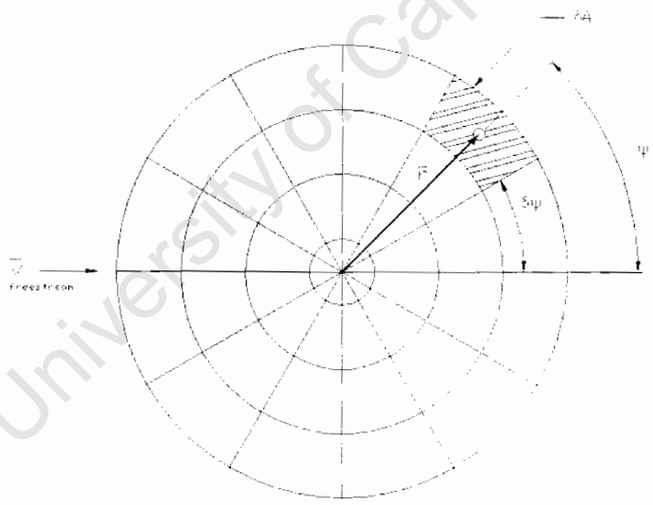

Figure 2-1: Rotor discretisation representation with shaded blade element and centroid shown

2.2 Coordinate systems

In order to simplify calculation of the momentum source terms, four coordinate systems are used to describe the rotor and blade elements. The Cartesian coordinate system 1, $(\bar{X},\bar{Y},\bar{Z})$, is the global coordinate system for the computational domain. Two coordinate systems are then used based on the rotor-disk centre. A Cartesian system 2 is defined, $(\bar{x},\bar{y},\bar{z})$, with $\bar{z}$ pointing along the axis of rotation, in the upstream direction, and $\bar{x}$ defined relative to the helicopter fuselage. A rotor based cylindrical coordinate system, $(\bar{r},\bar{\psi},\bar{z})$, is also used, with $\bar{\psi}$, the azimuth angle, defined relative to $\bar{x}$. During calculation of the blade element forces, a third Cartesian coordinate system is defined for each element, $(\bar{t},\bar{r},\bar{n})$, where $\bar{t}$ is tangential and opposite to the direction of blade rotation, and $\bar{r}$ is a radial vector corresponding to the rotor cylindrical system. $\bar{n}$ is an axial vector parallel to $\bar{z}$. This co-ordinate system is shown in Figure 2-2.

Because $\bar{r}$ is perpendicular to $\bar{n}$, $\bar{t}$ may be easily determined using the vector cross product

$$\bar{t} = \bar{r} \times \bar{n}; \qquad \bar{r} = \frac{\vec{r}}{|\vec{r}|} \tag{1}$$

Transformation tensors are used to change the description of vectors from one coordinate system to another as convenient.

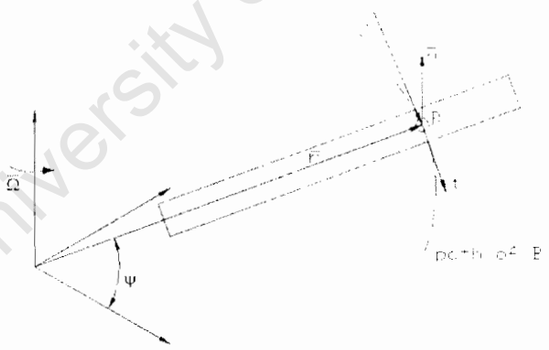

Figure 2-2: Blade-Element based coordinate system

2.3 Calculation of Momentum Source Terms

Values for the momentum source terms are determined at the beginning of every iteration of the flow-field solution. Blade element theory is used to determine the forces imparted on the fluid by the rotor blades, which may, with little manipulation, be directly substituted into the governing momentum equations as source terms.

According to Von Mises [1], the force exerted on the fluid stream at any location within the actuator disk is a function of the fluid velocity vector relative to the rotor-blade, $\bar{v}_R$, as well as the lift and drag characteristics of the blade cross-sectional profile. Figure 2-3 depicts the relative velocity vector, as well as the resulting elemental lift, δL, and elemental drag force, δD, on a blade element, at a blade radius $\bar{r}$.

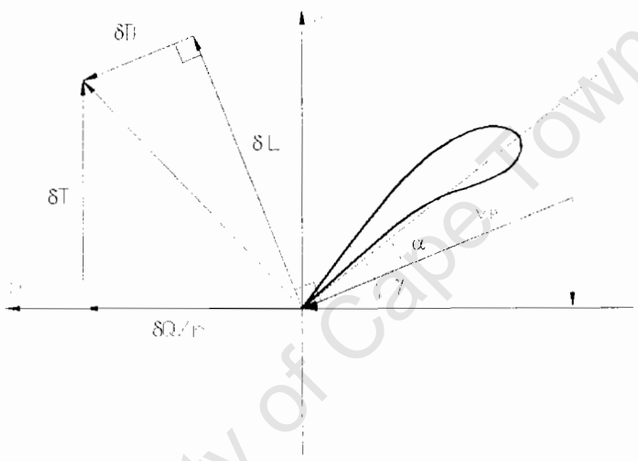

Figure 2-3: Blade element representation showing the relative velocity vector, $\bar{v}_R$, and the resulting aerodynamic loads

The lift and drag force are determined according to

$$\delta L = \tfrac{1}{2}\rho\left|\overline{v_R}\right|^2 C_l \cdot c \cdot \delta \mathrm{r} \qquad (2)$$

$$\delta D = \tfrac{1}{2}\rho\left|\overline{v_R}\right|^2 C_d \cdot c \cdot \delta \mathrm{r} \qquad (3)$$

where C_l and C_d are the coefficients of lift and drag respectively, c the rotor blade chord length, v_R the relative velocity, and δr the blade element radial thickness.

The lift and drag coefficients are determined from look-up tables based on the effective angle of attack and Reynolds number. The first step in calculating the blade element forces is therefore to determine the relative velocity vector.

The flow solver provides the flow-field velocity relative to the global coordinate system 1, at any prescribed location within the flow domain. The velocity vectors at the actuator disk may therefore be known directly. However, this velocity field encountered by the two-dimensional blade elements of the rotor model differs considerably from the uniform velocity field for which the lift and drag coefficients, used in equations (2) and (3) respectively, are valid. The most notable difference is the tangential velocity component of the velocity field on the downstream side of the blade element. In order to compensate for this discrepancy, the flow velocity vector at each disk element, $\overline{v}_l$, is calculated as the average of the trailing edge velocity vector, $\overline{v}_{out}$, and the free-stream velocity vector upstream of the blade element, $\overline{v}_{in}$. This arrangement is found to yield better results than when the free stream velocity vector upstream of blade element is used exclusively to determine $\overline{v}_l$ (see Appendix A).

$$\overline{v_l} = \tfrac{1}{2}(\overline{v_{in}} + \overline{v_{out}}) \qquad (4)$$

The relative velocity vector, $\bar{v}_R$, may now be calculated by accounting for the rotation of the rotor, using the rotor and blade-element based coordinate systems previously defined.

$$\overline{v_{R\ n}} = \bar{v} \bullet \bar{n} \qquad (5)$$

where $\bar{v} \bullet \bar{n}$ is the component of the free-stream velocity normal to the blade path, and is therefore the normal component of the relative velocity vector.

$$\overline{v_{R\ t}} = \bar{v} \bullet \bar{t} + (\bar{r} \times \overline{\Omega}) \bullet \bar{t} \qquad (6)$$

where $\bar{v} \bullet \bar{t}$ is the component of the free-stream velocity parallel to the blade path, at the element centroid. $(\bar{r} \times \overline{\Omega}) \bullet \bar{t}$ is the velocity due to the blade rotation in the direction parallel to the blade path at the element centroid, where $\overline{\Omega}$ is the rotor rotation vector.

Once the relative velocity vector is known, it only remains to calculate the coefficient of lift and drag to resolve equations (2) and (3). Within a specified range of Mach numbers, the lift and drag characteristics of a profile section is a function of the Reynolds number and the effective angle of attack, α_e, alone. The effective angle of attack is determined by the relative velocity vector, and the rotor geometric orientation.

During high advance ratios, a retreating blade may encounter reverse flow conditions near the hub. In addition, modelling of right and left hand blade profiles, as well as reverse rotations, may be desired. For this reason it is critical that the orientation of the blade-element profile be correctly defined. This is accomplished by defining two perpendicular vectors in the plane of the two-dimensional blade profile; $\overline{B}_t$, along the profile chord in the direction of the leading edge, and $\overline{B}_n$, in the direction of the upper surface of the airfoil profile. These vectors are determined based on the rotor characteristics, including the geometric angle of attack, γ, described according to

$$\gamma = A_0 - A_1 \cos\psi - B_1 \sin\psi - \frac{r}{R}\alpha_t \qquad (7)$$

where A_0 is the collective pitch angle, A_1 and B_1 define the cyclic pitch angle, r is the element radial position, R is the rotor tip radius, and α_t the angle of twist at the rotor tip.

Using the relative velocity components and blade orientation vectors, the effective angle of attack may be calculated.

$$\alpha_e = a\cos(-(\overline{v_R} \bullet \overline{B_t})/|\overline{v_R}|) \qquad \alpha_e = -\alpha_e \text{ if } \overline{v_R} \bullet \overline{B_n} < 0 \qquad (8)$$

The Reynolds number is calculated as

$$Re = \frac{\rho \cdot v_R \cdot c}{\mu} \qquad (9)$$

where the density, ρ, and the dynamic viscosity, μ, are flow properties obtained directly from the flow solver, $|\overline{v_R}|$ is the relative velocity magnitude, and c is the profile chord dimension.

Depending on the particular rotor being modelled, lift and drag profiles may be experimentally obtained as a function of angle of attack, α, for a range of values of both α and Reynolds number. For α values falling outside the range of experimental data, lift and drag characteristics for a flat plate are used. According to Hoerner and Borst [15], and Hoerner [16], the dimensionless lift and drag coefficients for a flat plate are given respectively as

$$C_l = C_{d\,max} \cdot \sin\alpha \cdot \cos\alpha \qquad (10)$$

and

$$C_d = C_{d\,max} \cdot sin^2\alpha \qquad (11)$$

where $C_{d\,max}$ = 1.98.

A smooth transition between the airfoil and flat plate lift and drag characteristics is ensured with the introduction of fourth order polynomial and trigonometric functions in the overlap regions. The resulting lift and drag curves are shown in Figure 3-4, as a function of angle-of-attack, α. Linear interpolation is used to determine C_l and C_d values at intermediate Reynolds numbers.

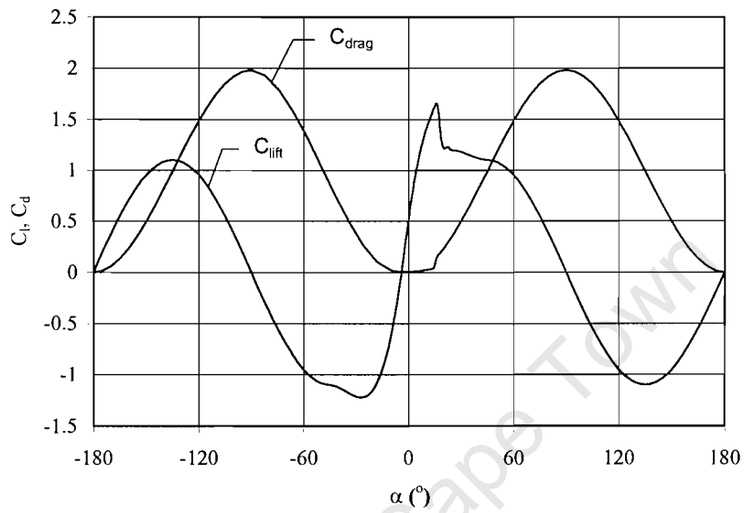

Figure 2-4: An example of the lift and drag airfoil tables used to determine blade-element aerodynamic loads [22]

With C_l and C_d now known, in addition to the relative velocity magnitude, the elemental lift and drag forces, δL and δD, may now be calculated according to equations (2) and (3). The direction of these vectors is determined relative to the blade-element orientation vectors, $\overline{B}_t$ and $\overline{B}_n$, to obtain lift and drag vectors, $\overline{\delta L}$ and $\overline{\delta D}$.

From Figure 2-3, the blade element thrust, δT, and torque, δQ, are given as

$$\delta T = \sigma (\overline{\delta L} \bullet \overline{n} + \overline{\delta D} \bullet \overline{n}) \quad (12)$$

$$\delta Q = \sigma (\overline{\delta L} \bullet \overline{t} + \overline{\delta D} \bullet \overline{t}) \cdot r \quad (13)$$

The blade solidity factor, σ, is defined as

$$\sigma = \frac{N \cdot c}{2\pi \cdot r} \quad (14)$$

where N is the number of rotor-blades.

The blade forces are expressed as momentum sources/sinks in the governing equations, and the blade element thrust and torque need therefore to be expressed as force per unit volume. It follows that

$$\frac{\delta T}{\delta V} = \frac{\delta T}{c \cdot \delta r \cdot t_{Rdisk}} \quad (15)$$

$$\frac{\delta Q}{\delta V} = \frac{\delta Q}{c \cdot \delta r \cdot t_{Rdisk}} \quad (16)$$

where δr is the element radial dimension, and t_{Rdisk} the rotor-disk thickness.

Substitution of equations (2), (3), (12) and (13) into equations (15) and (16) yields

$$\frac{\delta T}{\delta V} = \frac{\sigma \cdot \rho \cdot v_R^2}{2 \cdot t_{Rdisk}} \cdot (\overline{Cl} \bullet \overline{n} + \overline{Cd} \bullet \overline{n}) \quad (17)$$

$$\frac{\delta Q}{\delta V} = \frac{\sigma \cdot \rho \cdot v_R^{\,2}}{2 \cdot t_{Rdisk}} \cdot (\overline{Cl} \bullet \bar{t} + \overline{Cd} \bullet \bar{t}) \cdot r \qquad (18)$$

These expressions are defined relative to the blade-element, and must be transformed back to the global coordinate system. The components of the momentum source vector may then be substituted directly into the momentum equations within the flow solver.

3 NUMERICAL MODELLING STRATEGY FOR VALIDATION OF THE ROTOR MODEL

The numerical modeling strategy used in validating the rotor model is described in the following sections. The steady, time-averaged Navier-stokes governing equations where used, combined with a standard k-ε turbulence model. A second-order upwind discretisation scheme was used for pressure and momentum convection terms, and a first-order scheme for the convection terms of the turbulence model. It was found that consistently accurate results were obtained for a variety of flow-rates and blade pitch angles using 2500 to 3000 cells in the actuator disk. Flow-field velocity readings were taken at positions 10mm upstream and downstream of the actuator disk centre-plane.

3.1 Governing Equations

The steady, incompressible, viscous, Reynolds-averaged conservation equations are solved by the CFD solver, *Fluent*, in a Cartesian coordinate system. The equations may be represented in vector notation as follows [17].

3.1.1 Conservation of mass

Mass conservation is expressed by

$$div\,\bar{v} = 0 \qquad (19)$$

3.1.2 Conservation of momentum

The Navier-Stokes equations for the conservation of momentum may be simplified for the case of incompressible viscous flow, with constant transport properties, to

$$\rho\frac{D\bar{v}}{Dt} = -\bar{\nabla}\hat{p} + \bar{v}\bullet\tau_{ij} + \bar{S} \qquad (20)$$

where ρ is the fluid density, $\bar{S}$ the momentum source vector, and $\hat{p}$ the total hydrostatic pressure

$$\overline{\nabla}\hat{p} = \overline{\nabla}p - \rho\overline{g} \qquad (21)$$

Note that the total derivative is expanded by the expression

$$\frac{D\overline{v}}{Dt} = \frac{\partial\overline{v}}{\partial t} + \overline{v} \bullet \nabla\overline{v} \qquad (22)$$

For steady flows, the first term on the right hand side falls away.

The stress tensor, τ_{ij}, may be written as follows:

$$\tau_{ij} = \mu\left(\frac{\partial v_i}{\partial x_j} + \frac{\partial v_j}{\partial x_i}\right) - \rho\overline{v'_i v'_j} \qquad (23)$$

where μ is the molecular dynamic fluid viscosity. From this expression it is apparent that mathematically, the turbulent inertia terms act as a combination of the Newtonian viscous stresses, the first term, and a turbulent "Reynolds" stress tensor component, the second term.

3.2 Turbulence Model

A standard k-ε turbulence model was used for the requirements of validation. Widespread commercial use has shown the k-ε turbulence model to provide a good approximation of the effects of turbulence for a wide variety of flow conditions. The values used in the standard k- ε model in *Fluent* are given in Table 3-1 below.

Table 3-1: Values assigned to the standard k- ε turbulence model coefficients

C_μ	σ_k	σ_ε	$C_{\varepsilon 1}$	$C_{\varepsilon 2}$
0.09	1.00	1.30	1.44	1.92

3.3 Discretisation Practices

For a given computational grid, the choice of a particular discretisation scheme is a compromise between numerical stability and accuracy. While first-order discretisation is generally numerically more stable than the second-order scheme, it will usually yield less accurate results, especially when the flow is not aligned with the grid. In this situation numerical or false diffusion may arise, leading to inaccurate results. In *Fluent*, several options are given for discretisation of the convection terms. Second-order accuracy is automatically used for the viscous terms.

In the current investigation a second-order upwind difference scheme was selected in *Fluent* for calculation of the momentum and pressure convection terms. This option is in fact a blend of first-order upwind and central differencing schemes, in the conventional sense of these terms. The QUICK scheme [22] was investigated for discretisation of the momentum terms, with no significant improvement in accuracy. This scheme is used to compute a higher-order value of the convected variable at a cell face, and will typically be more accurate on structured grids aligned with the flow direction.

Discretisation of the turbulence kinetic energy and turbulence dissipation rate terms was accomplished using a first order upwind difference scheme. The k-ε model is at best an approximation of the effects of turbulence, while the rotor model itself is only a representation of an axial flow fan. Detailed resolution of the turbulent flow was therefore not deemed necessary for this investigation, provided the global characteristics were captured with sufficient accuracy.

3.4 Boundary Conditions

Several flow boundary options are offered in *Fluent*, in addition to the impermeable *wall* boundary. Flow boundaries, as described below, are generally surfaces through which flow enters or exits the computational domain. Depending on the boundary type chosen, the user is able to specify certain flow properties to flow crossing the boundary. The boundary types used in the current investigation are the *wall, velocity inlet, pressure inlet, pressure outlet,* and *outflow* boundaries. Each of these is briefly discussed below.

3.4.1 Wall Boundary

Wall boundary conditions are used to define bounded limits for the flow in the computational domain. In viscous flows, the no-slip boundary condition is applied at walls by default. However, varying degrees of slip and/or wall-velocities may be specified by the user. The shear stress and heat transfer between the fluid and wall are computed based on the flow details in the local flow-field.

3.4.2 Velocity Inlet Boundary

Velocity Inlet boundary conditions are used to define the velocity vectors and scalar properties of flow crossing the specified boundary. Generally, this condition is applied to flow entering the computational domain, and in the present investigation, is used to define a volumetric flow rate through the actuator disk.

3.4.3 Pressure Inlet Boundary

Pressure Inlet boundary conditions are used to define the total pressure and other scalar quantities of flow entering through the boundary. The velocity direction may also be specified. In the case of flow exiting through the boundary, the specified total pressure is used as the static pressure.

3.4.4 Pressure Outlet Boundary

Pressure Outlet boundary conditions are used to define the static pressure at flow boundaries. Generally, this condition is applied to flow exiting the computational domain, but for flows entering through the boundary, the specified static pressure is again used. An advantage of the Pressure Outlet condition is that it allows the user to define scalar quantities such as turbulence variables, as well as velocity direction, in the case of backflow.

3.4.5 Outflow Boundary

Outflow boundary conditions are used to model flow boundaries where details of the velocity and pressure of flow exiting the computational domain are not known prior to solution of the flow problem. The Outflow boundary assumes a zero normal gradient for all flow variables except pressure, and therefore is most suited to exit flow close to a fully developed condition. Importantly, any re-circulation across the boundary may lead to inaccurate results, since when flow enters the domain through an outflow boundary, scalar properties of the flow are not defined.

4 EXPERIMENTAL DATA USED FOR VALIDATION OF THE ROTOR MODEL

The experimental data against which the current model has been validated was obtained from Bruneau [18] and Stinnes and von Backström [19]. These authors measured flow variables for the axial-flow condition for the so called B-fan, an axial-flow fan with characteristics described in Table 4-1. The hub-to-tip ratio describes the ratio of the hub diameter to the fan casing diameter. The root blade pitch angle is the geometric angle of attack of the fan blades at their root on the hub diameter. This is measured as the included angle between the profile chord and the plane of rotation.

Table 4-1: B-Fan characteristics

Fan Casing Diameter, d_{FC} (mm)	No. of blades	Rotational Speed (rpm)	Hub-to-tip diameter ratio, d_{FH}/d_{FC}	Blade profile	Root stagger angle (°)
1542	8	750	0.40	NASA-LS	28-32

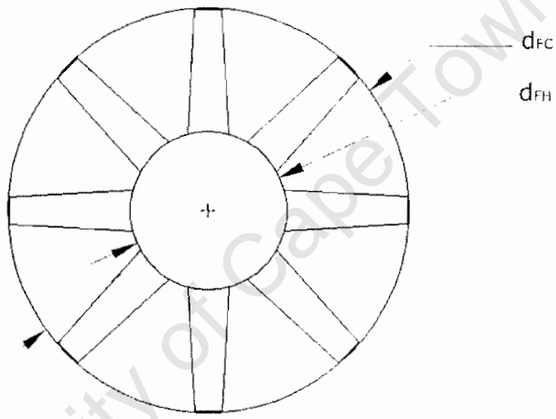

Figure 5: Schematic representation of the B-fan

In addition, Stinnes and von Backström [19] investigated the effect of off-axis upstream conditions on this fan. This data was used to validate the ability of the current model to deal with an angled upstream flow component, the condition encountered by a helicopter rotor in forward flight.

The experimental model with which these results were obtained is represented in Figure 4-1 below, with the physical details of the duct sections given in Table 4-2. This data was used to reproduce the experimental model within the computational grid.

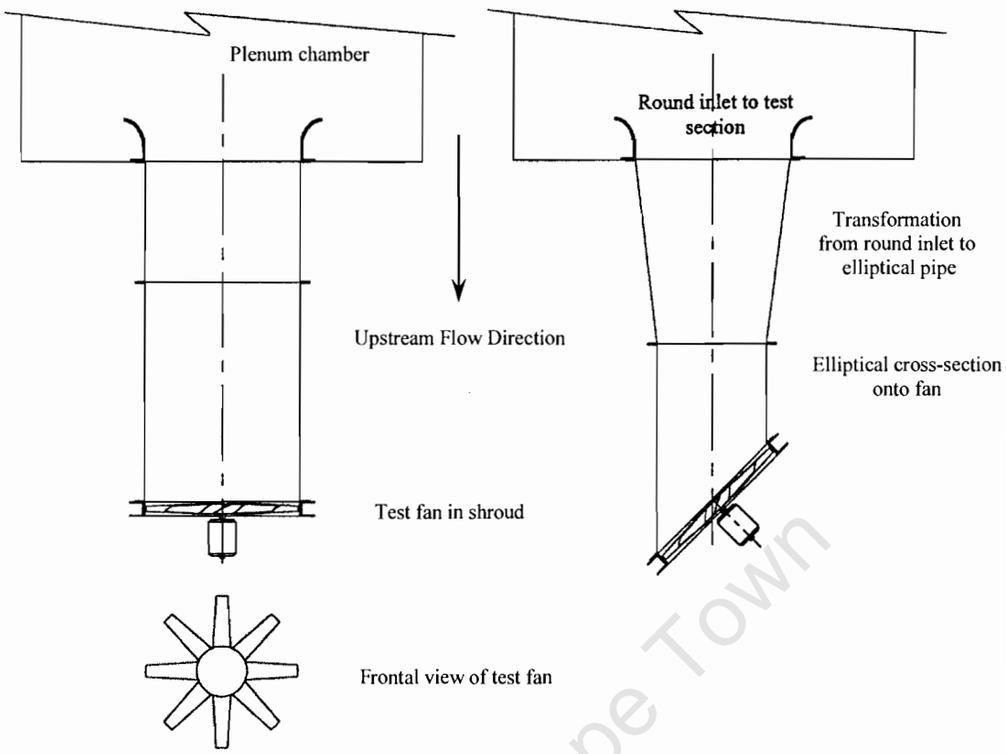

Figure 4-6: Plan view of the experimental fan inlet section (00° and 45° pipe angle) [19]

Table 4-2: Inlet pipe sections [19]

Cross-flow component to on-flow component (%)	0	12.5	25	50	100
Pipe angle (nominal) (°)	00	7	14	27	45
Length of transformation section (mm)	1840				
Length of elliptical section at centreline (mm)	1542				
Shortest side of elliptica duct section (mm)	1542	1446	1355	1197	997

5 MODEL VALIDATION FOR UPSTREAM FLOW ALIGNED WITH THE FAN AXIS

The initial validation process was carried out for the case of axially aligned upstream flow conditions. The computational grid used for the simulations is presented below, followed by a description of the method used to calculate the fan performance characteristics. Finally, a comparison between the numerical results and experimental data is presented

5.1 Computational Grid

A structured grid was used throughout the validation process, the grid density being determined primarily by the grid structure used for the actuator disk. If too few cells were specified in the disk, the fan characteristics were not accurately captured, as the model assumes uniform properties throughout each element, based on the cell-centroid values. For a course disk-mesh, convergence problems were experienced for this reason. In the opposite extreme though, a very fine disk-mesh would require computing and time resources beyond those which were available for this investigation.

It was found that using 2500 to 3000 elements in the actuator disk, using incrementally increasing spacing in the radial direction, provided consistently accurate results. The difference between this grid geometry, and results obtained using a 7000-cell actuator disk, were negligible. An example of the rotor disk computation grid is shown in Figure 5-1 below.

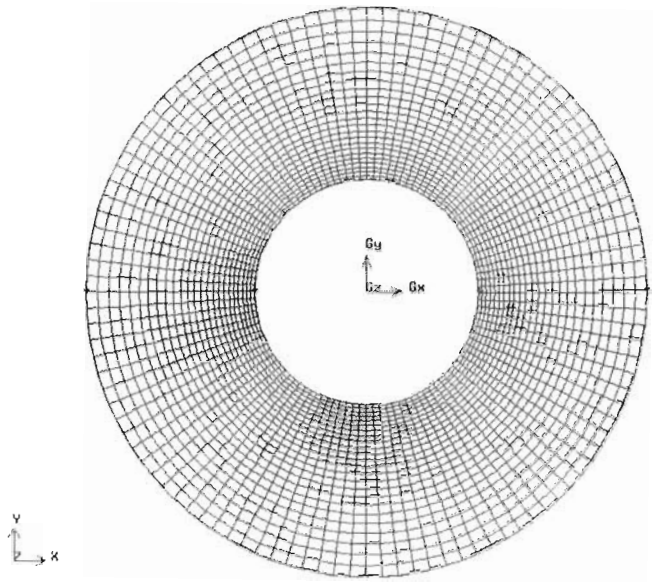

Figure 5-1: Actuator disk computation grid, comprising 2592 cells

In the axial direction, the grid refinement was increased incrementally towards the actuator disk region, with the smallest spacing corresponding with the actuator disk thickness of 5 mm. The computational grid for the rotor disk with annular outlet duct is shown in Figure 5-2 below.

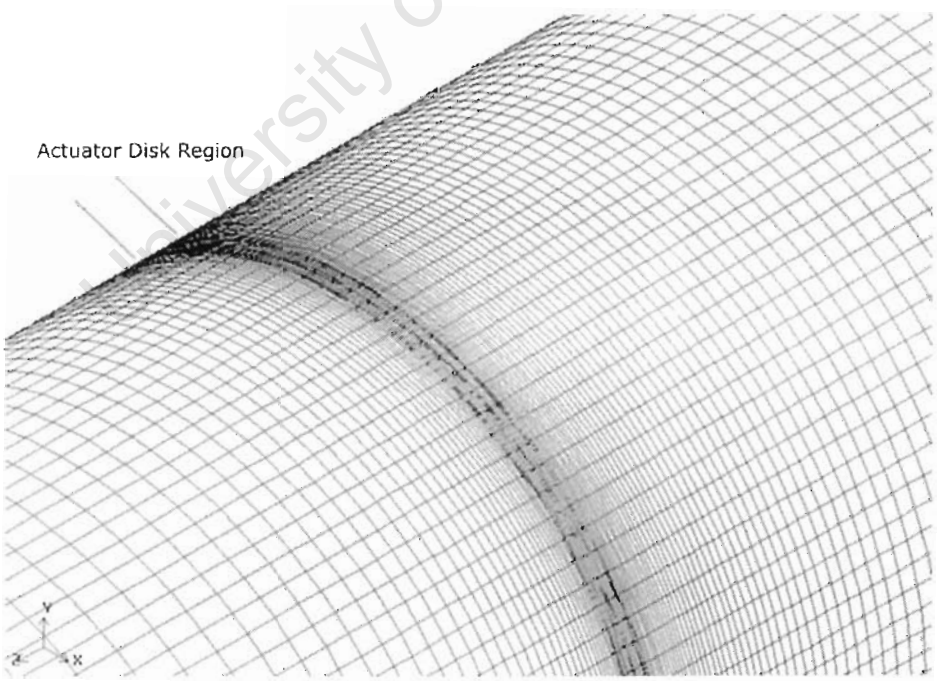

Figure 5-2: Axial mesh refinement in the region of the actuator disk

Meyer and Kröger [13] reported fan performance characteristics for an actuator disk fan model very similar to the present model. They had earlier demonstrated that the addition of an annular section downstream of the fan did not affect the performance characteristics of the fan in any way, and that this configuration could indeed be used to model the fan according to the specification set in BS 848 [20]. Significantly, the use of this outlet duct, as opposed to modelling a region of atmosphere downstream of the fan, greatly reduced the size of the computational domain. An Outflow boundary was specified at the downstream end of the outlet duct. The upstream boundary was specified with a Velocity Inlet condition, determining the flow rate through the fan.

Based on the reported success of this model, a similar configuration was used for validation of the present model for the axially aligned upstream flow condition. The computational grid included the actuator disk, with axial thickness 5 mm, in which the momentum source terms were applied. Spaced 20 mm upstream and downstream, identical disks were defined in which the upstream and downstream flow velocity vectors were obtained. The upstream duct length was 1542 mm, or one fan casing diameter, with a downstream duct length of two fan casing diameters, or 3084 mm, as depicted in figures 5-3 to 5-5 below.

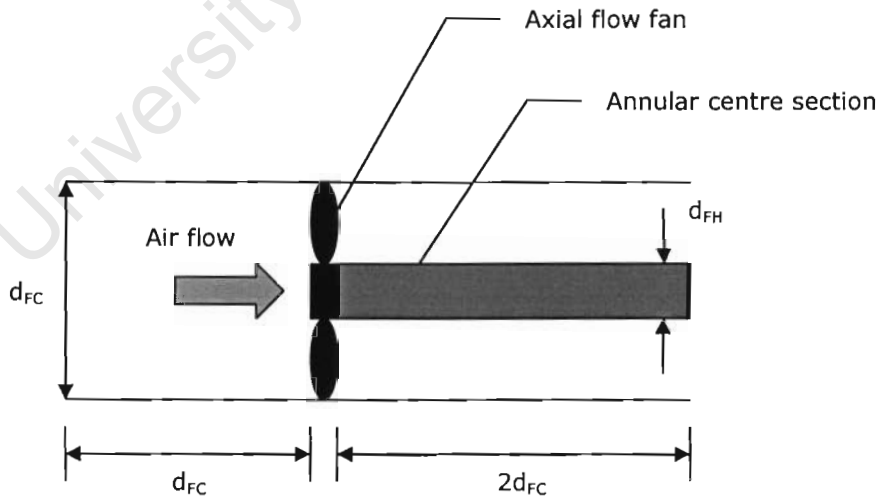

Figure 5-3: Geometry modelled by Meyer and Kröger [20]

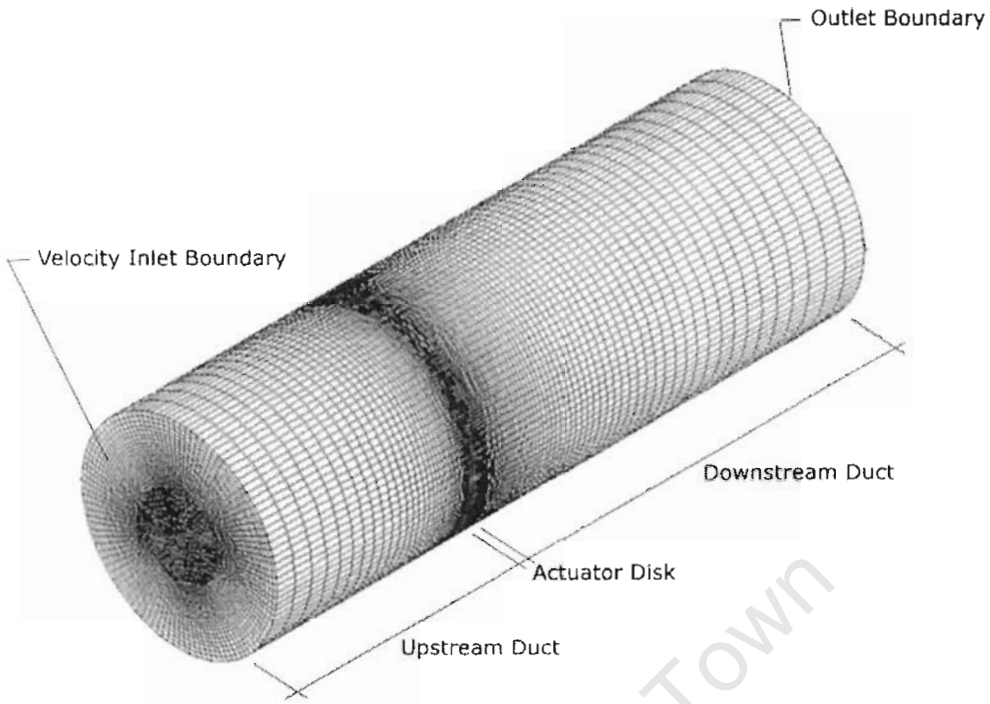

Figure 5-4: Computational grid used for the annular-ducted downstream flow configuration

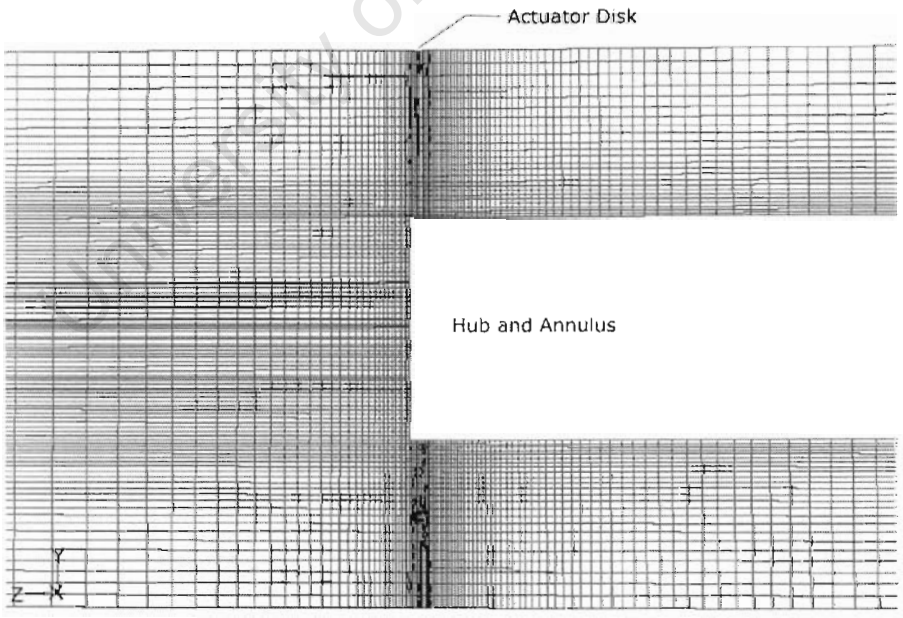

Figure 5-5: Computational grid used for the annular-ducted downstream flow configuration (Cross-section on the YZ-Plane)

5.2 Calculation of Fan Performance Characteristics

The fan performance characteristics were determined according to specifications set in BS848 [20] of the British Standards Organisation, for a type A (free inlet, free outlet) installation. The fan performance characteristics include fan static pressure rise, Δp_{Fs}, fan power consumption, P_R, and the fan static efficiency, η_{Fs}, plotted as a function of the volumetric flow rate, V. The definition of these fan parameters is given below.

Fan static pressure rise is calculated as

$$\Delta p_{Fs} = p_o - (p + 0.5\rho v^2)_i \tag{24}$$

where the inlet and outlet static pressures are taken as area-weighted averages over the upstream and downstream flow boundaries respectively. The volumetric flow rate, V, is specified by choosing the upstream flow boundary condition as a Velocity Inlet boundary, and specifying an inlet velocity, v_i, with respect to a known inlet area.

Fan power consumption is calculated as

$$P_R = \frac{2\pi}{60} NQ \tag{25}$$

where the fan torque, Q, is obtained from the UDF, while the rotational speed of the fan, N, is specified in rpm. The symbol Q is used for torque, as T will be used later for rotor thrust.

Fan static efficiency is calculated as

$$\eta_{Fs} = \frac{\Delta P_{Fs} V}{P_R} * 100 \tag{26}$$

where V is the volumetric flow rate.

5.3 Results and discussion

Results obtained for axially aligned upstream flow, using the annular outlet duct, are represented below, together with experimental data obtained from Bruneau [18] and Stinnes and von Backström [19].

5.3.1 Fan static pressure rise

The correlation between numerical and experimental results for fan static pressure rise was excellent over the range of flow rates and blade angles tested. The results are given below in graphic form, and numerically in Appendix B.

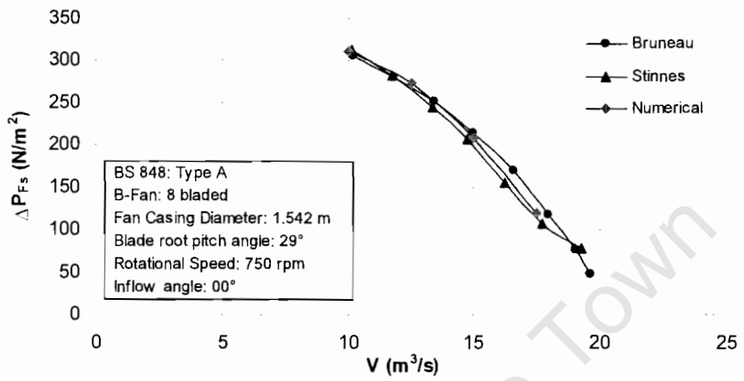

Figure 5-6: Fan static pressure rise vs. Volume flow rate for a blade root pitch angle of 29°

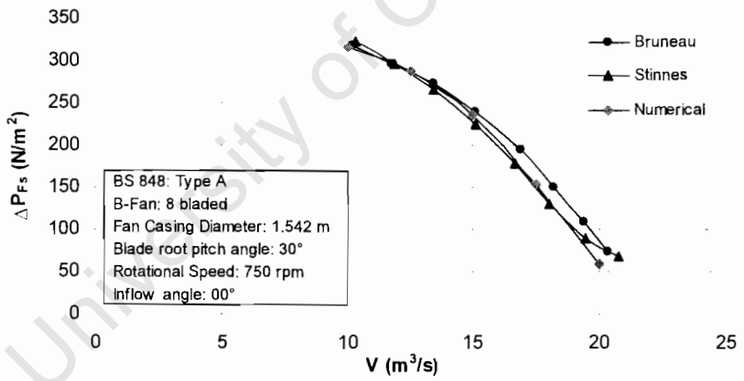

Figure 5-7: Fan static pressure rise vs. Volume flow rate for a blade root pitch angle of 30°

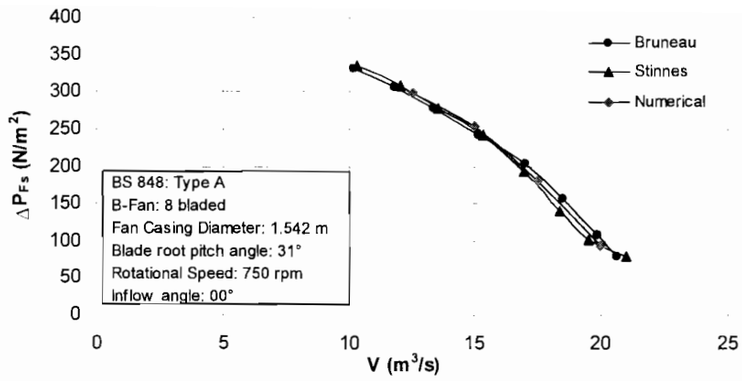

Figure 5-8: Fan static pressure rise vs. Volume flow rate for a blade root pitch angle of 31°

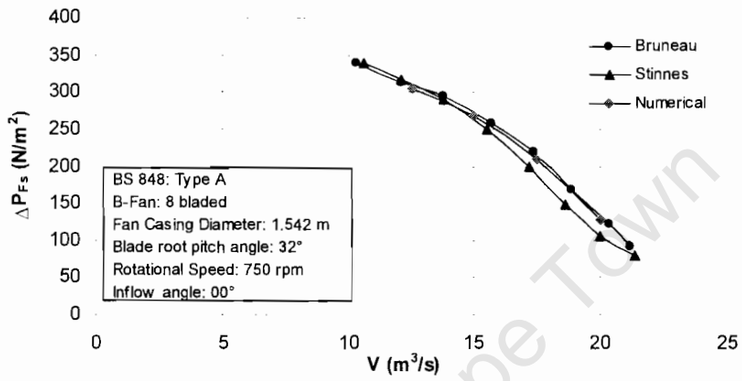

Figure 5-9: Fan static pressure rise vs. Volume flow rate for a blade root pitch angle of 32°

5.3.2 Fan power consumption

The fan power consumption is under-predicted by the numerical model. This may be attributed to frictional losses not accounted for in the numerical model. These include physical rotational instabilities, leading to increased mechanical losses, and tip effects due to the clearance between the fan blade tips and the fan casing. Power consumption trends are nevertheless consistently predicted by the numerical model for pitch angles ranging from 29° to 32°, and for flow rates between 10 and 20 m^3/s.

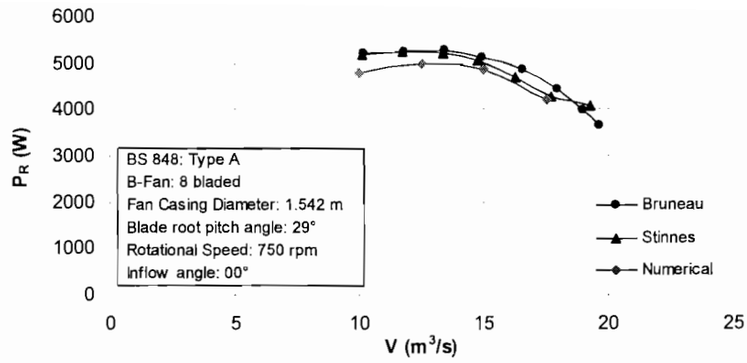

Figure 5-10: Fan power consumption vs. Volume flow rate for a blade root pitch angle of 29°

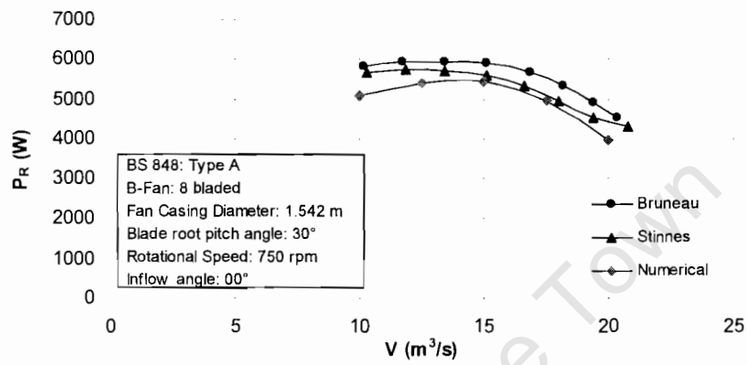

Figure 5-11: Fan power consumption vs. Volume flow rate for a blade root pitch angle of 30°

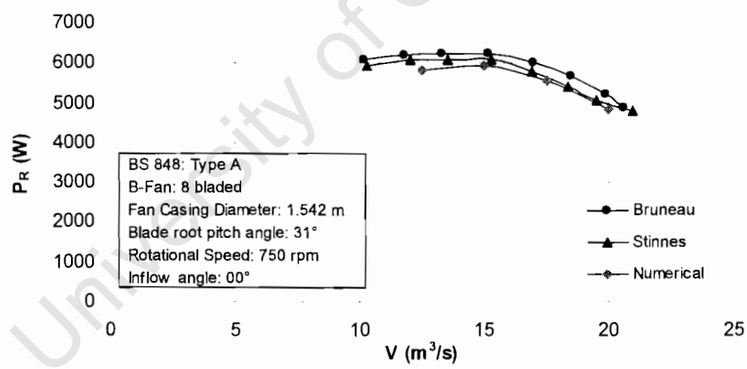

Figure 5-12: Fan power consumption vs. Volume flow rate for a blade root pitch angle of 31°

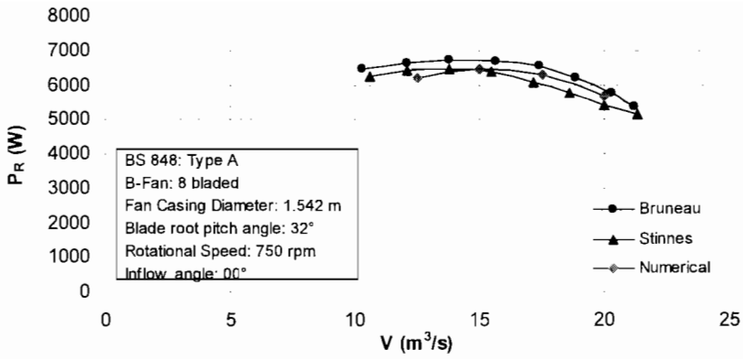

Figure 5-13: Fan power consumption vs. Volume flow rate for a blade root pitch angle of 32°

5.3.3 Fan static efficiency

Due to the low fan power consumption values predicted by the rotor model, the numerically predicted fan static efficiency is slightly elevated. However, comparison with experimental data demonstrates that the global trends are consistently well predicted over the range of flow rates and blade angles tested.

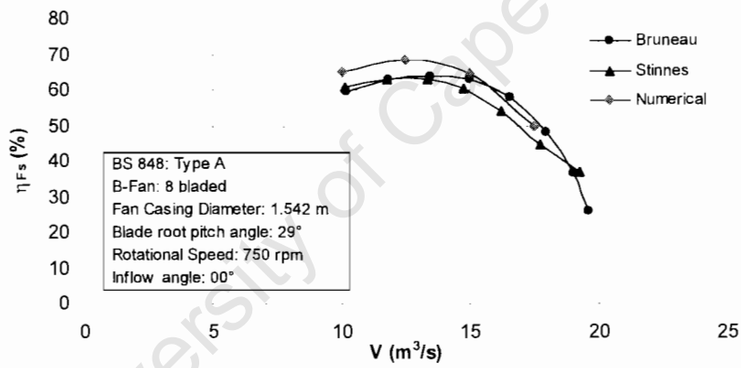

Figure 5-14: Fan static efficiency vs. Volume flow rate for a blade root pitch angle of 29°

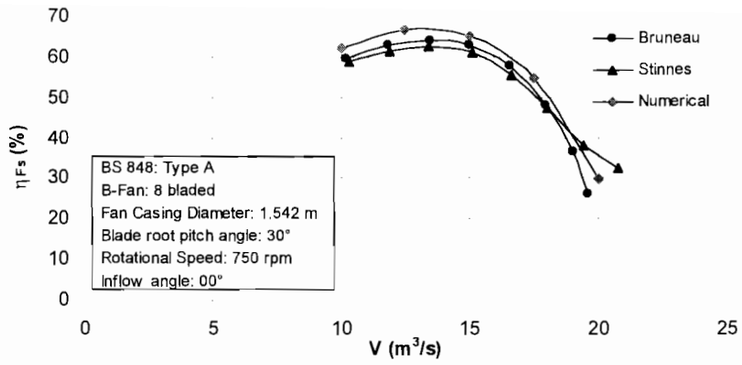

Figure 5-15: Fan static efficiency vs. Volume flow rate for a blade root pitch angle of 30°

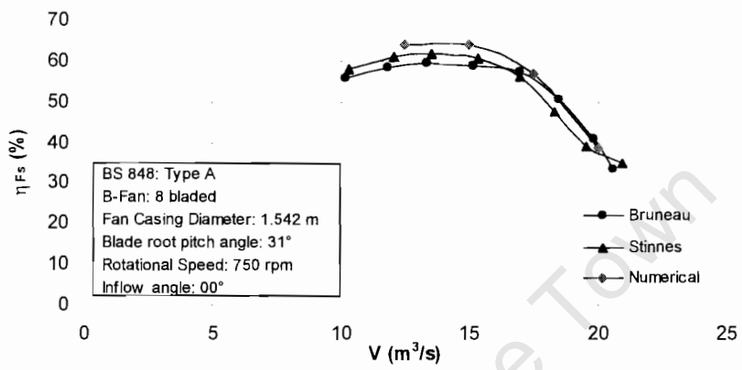

Figure 5-16: Fan static efficiency vs. Volume flow rate for a blade root pitch angle of 31°

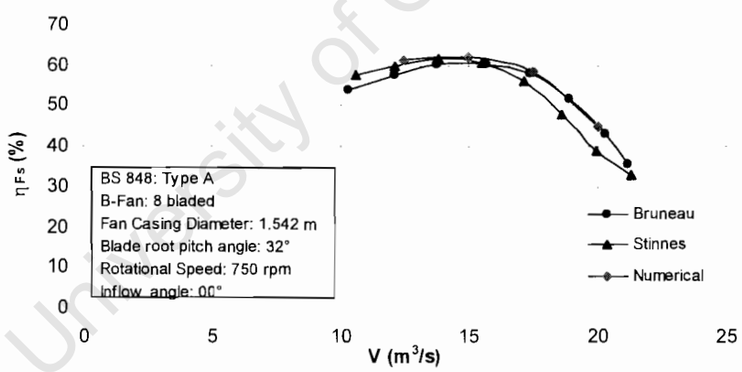

Figure 5-17: Fan static efficiency vs. Volume flow rate for a blade root pitch angle of 32°

6 MODEL VALIDATION FOR UPSTREAM FLOW NOT ALIGNED WITH THE FAN AXIS

A critical test of the rotor model's suitability to model a helicopter in forward flight was its performance when subjected to an off-axis upstream flow component. A variety of angled upstream ducts were used to create off-axis inflow conditions, and the predicted fan performance characteristics were compared with experimental data reported by Stinnes and von Backström [19] for similar flow conditions.

6.1 Computational grid

Due to the expectation of off-axis flow downstream of the fan for angled upstream flow conditions, the use of a duct downstream of the fan was no longer desirable. A region of atmosphere was therefore created downstream of the actuator disk, replacing the annular duct in modelling a free exit in the computational domain. In order to determine the effect of this modification, a series of simulations were carried out with this new configuration, coupled with the axially aligned upstream duct.

6.1.1 Validation of the computational model with a free downstream exit

Simulations were carried out using a free exit atmospheric region downstream of the fan, with sufficiently distant boundaries that their effect on the solution should be minimal. The upstream duct and actuator disk regions were retained from previous simulations. The atmospheric free exit region was created with dimensions of 10 fan casing diameters length, and an outside diameter 5.6 times the fan casing diameter.

As before, a Velocity Inlet boundary condition was imposed on the upstream flow boundary. On the atmospheric boundaries, a Pressure Inlet boundary was defined to model the re-circulating flows expected in the region of the fan. However, a Pressure Outlet boundary condition was found to produce almost identical results. The computational grid is shown in figures 6-1 to 6-3 below.

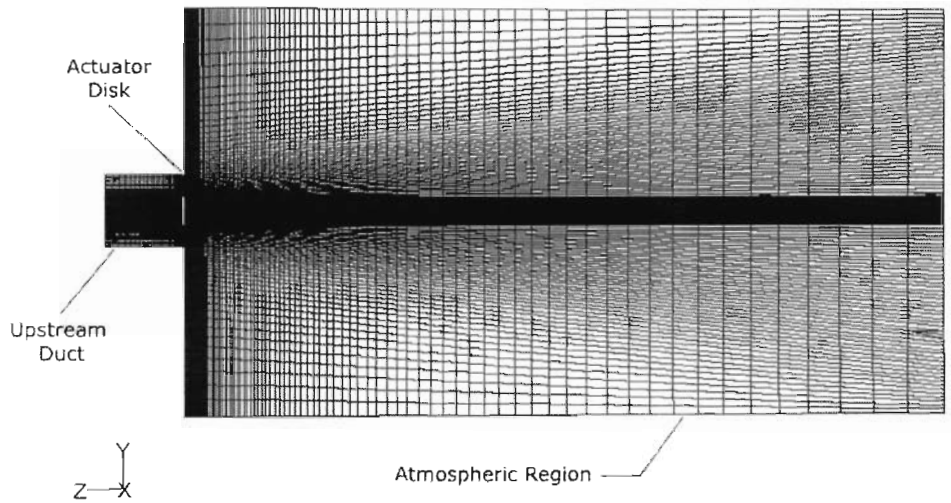

Figure 6-1: Computation grid with free exit atmospheric region

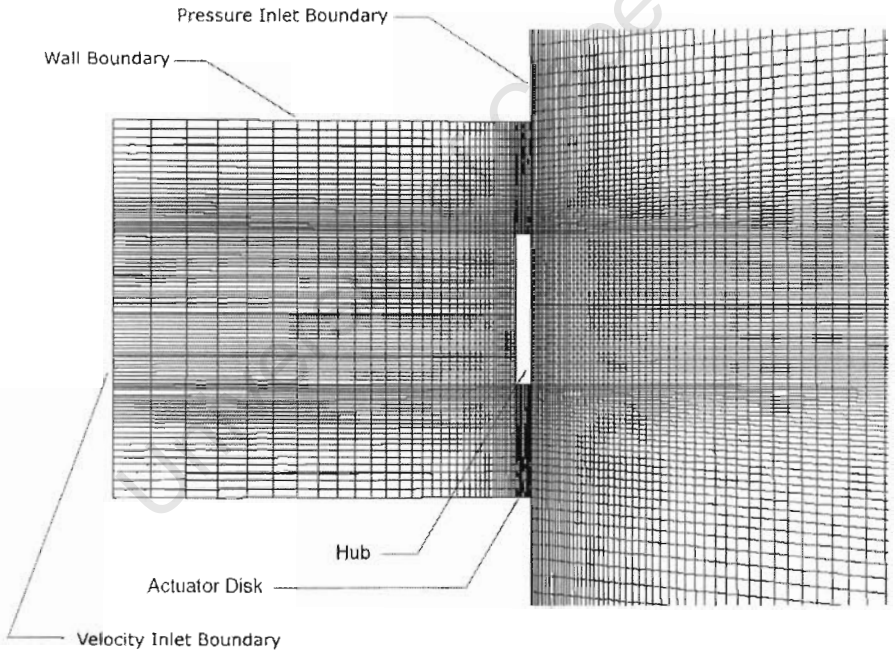

Figure 6-2: Computational grid showing boundary conditions around the actuator disk region

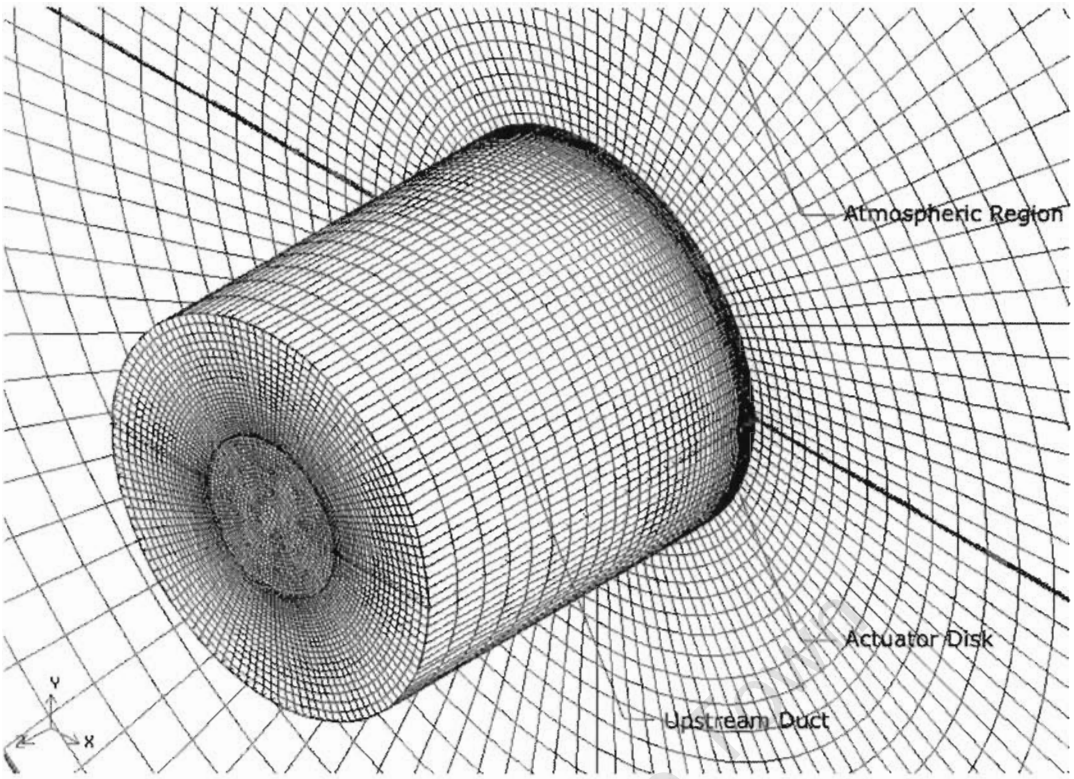

Figure 6-3: Exterior geometry with superimposed grid structure

Once again, the fan performance characteristics of interest were fan static pressure rise, fan power consumption, and fan static efficiency. The results shown below, in figures 6-4 to 6-9, were obtained as described in section *5.2 Calculation of Fan Performance Characteristics,* and are once again presented together with experimental data obtained from Bruneau [18] and Stinnes and von Backström [19].

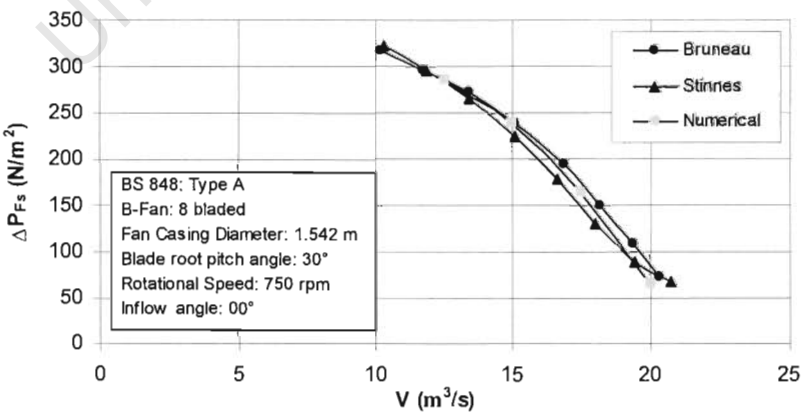

Figure 6-4: Fan static pressure rise vs. Volume flow rate for a blade root pitch angle of 30°

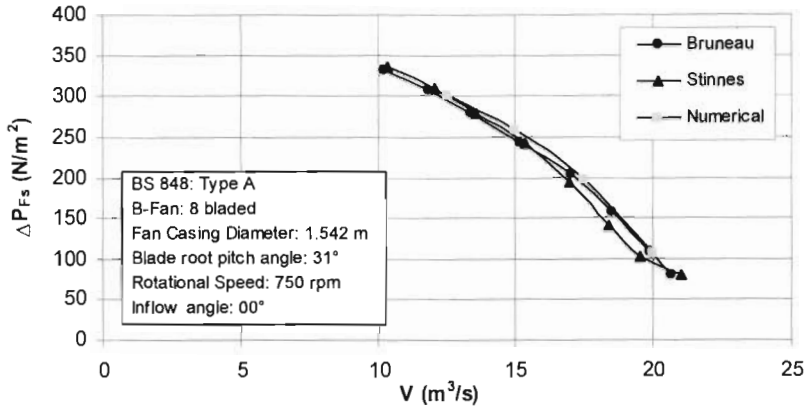

Figure 6-5: Fan static pressure rise vs. Volume flow rate for a blade root pitch angle of 31°

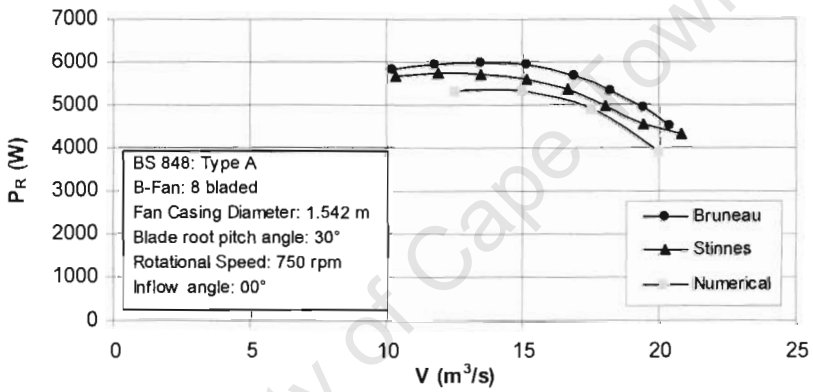

Figure 6-6: Fan power consumption vs. Volume flow rate for a blade root pitch angle of 30°

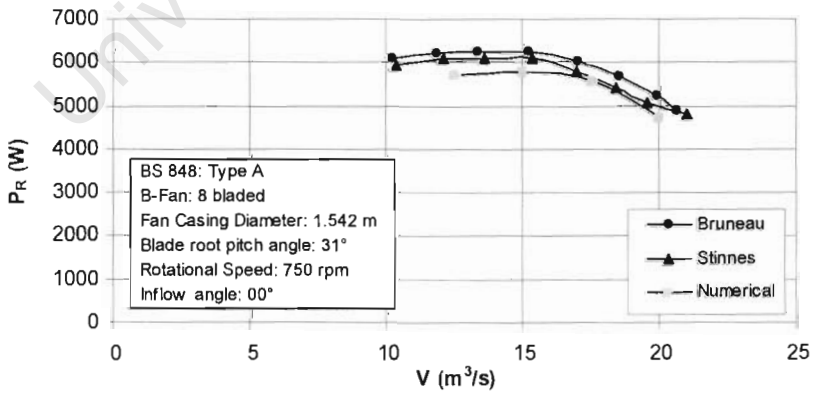

Figure 6-7: Fan power consumption vs. Volume flow rate for a blade root pitch angle of 31°

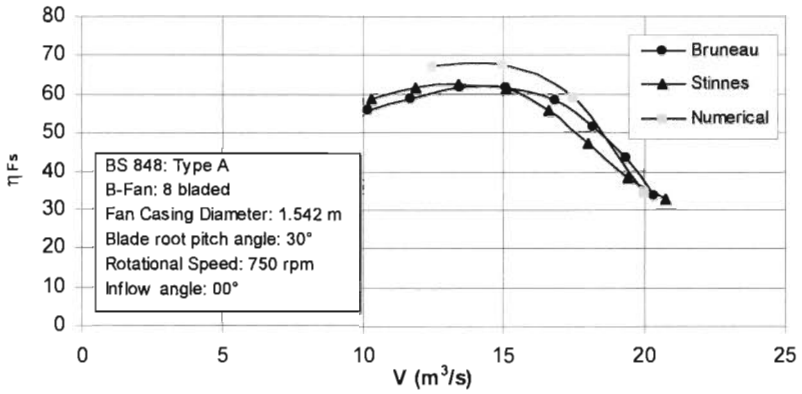

Figure 6-8: Fan static efficiency vs. Volume flow rate for a blade root pitch angle of 30°

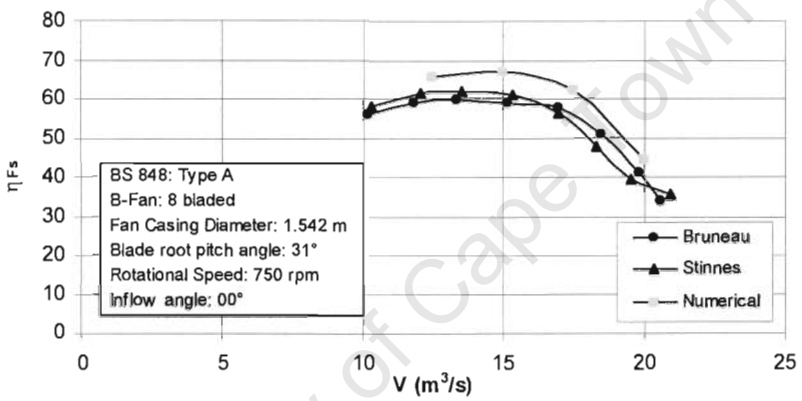

Figure 6-9: Fan static efficiency vs. Volume flow rate for a blade root pitch angle of 31°

6.1.2 *Computational grid for angled upstream flow ducts of 0°, 14°, 27° and 45°*

The computational grid used to model off-axis upstream flow conditions was based on the physical model of Stinnes and von Backström [19]. This experimental model is described in Chapter 4 of this report. Upstream inlet ducts, similar to those used experimentally, were used to create the cross-flow component into the fan. An atmospheric free exit region was specified downstream of the fan, as described earlier in this chapter. The computational grid used for the simulations is depicted in figures 6-10 to 6-12 below.

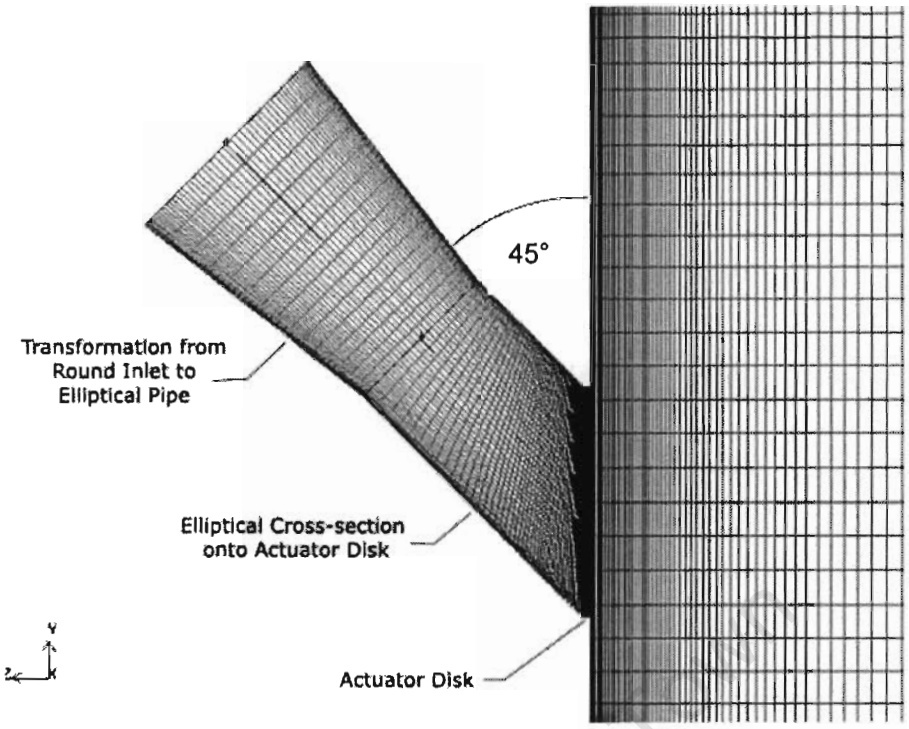

Figure 6-10: 45° Upstream duct, showing the elliptical and transformation sections of the duct, and the actuator disk and atmospheric regions

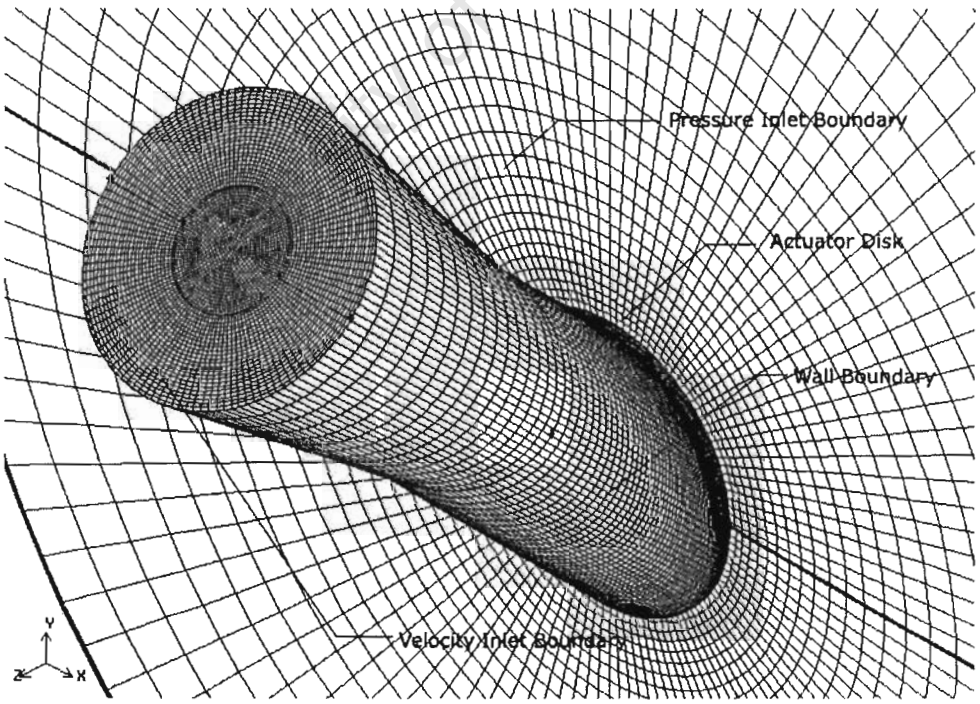

Figure 6-11: 45° Upstream duct geometry, showing boundary conditions assigned in the region of the actuator disk

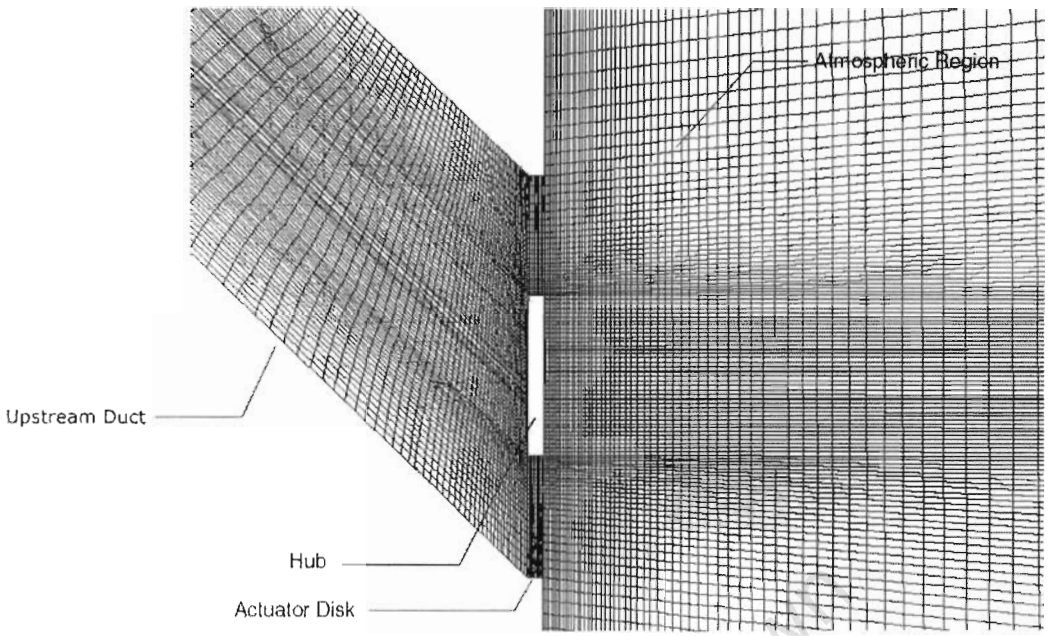

Figure 6-12: Computational grid in the region of the actuator disk

6.2 Results and discussion

The numerical results for simulations with off-axis upstream conditions are shown in the following sections in graphic form, together with experimental data from Stinnes and von Backström [19]. The results indicate characteristics consistent with those predicted for upstream flows aligned with the fan axis. Fan static pressure rise is accurately predicted, with fan power consumption and fan static efficiency low and high respectively.

6.2.1 Fan static pressure rise

As noted earlier for the axial flow upstream condition, numerical agreement with experimental data for the fan static pressure is excellent over the range of flow-rates tested. In figures 6-13 and 6-19, the adverse effect on fan static pressure created by off-axis flow is shown experimentally for flow rates between 10 and 20 m^3/s, for blade pitch angles of 30 and 31 degrees. In figures 6-14 and 6-20, this trend is confirmed by the numerical results. In addition, the accuracy of the numerical predictions for static pressure rise is demonstrated graphically in figures 6-15 to 6-18, and 6-21 to 6-24.

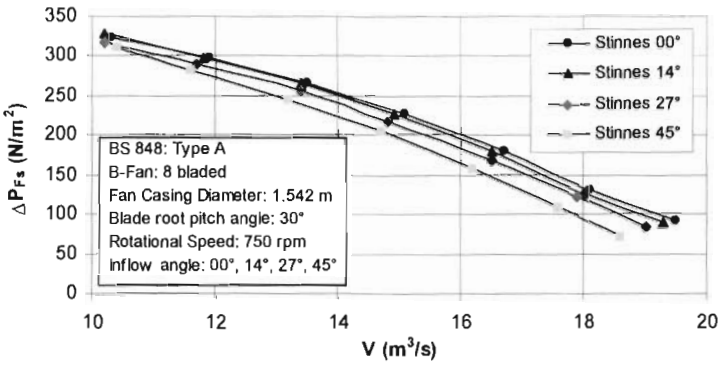

Figure 6-13: Experimental data for Fan static pressure rise vs. Volume flow rate for a blade root pitch angle of 30° and inlet angles of 00°, 14°, 27° and 45°

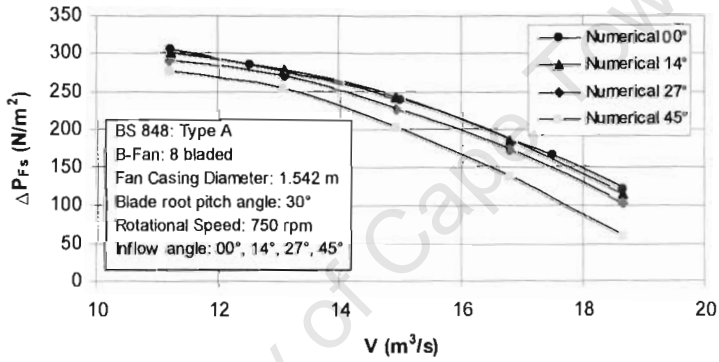

Figure 6-14: Numerical results for Fan static pressure rise vs. Volume flow rate for a blade root pitch angle of 30° and inlet angles of 00°, 14°, 27° and 45°

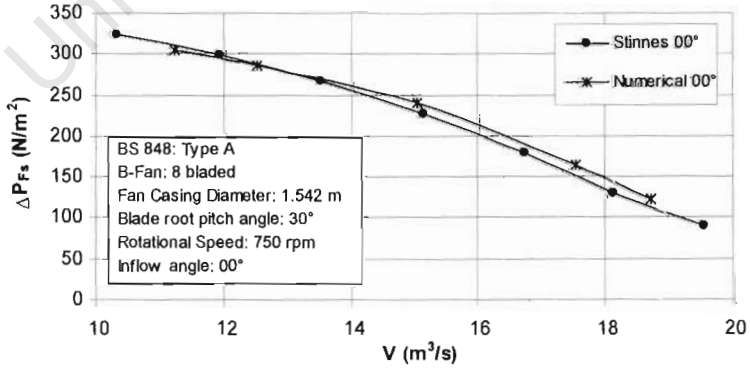

Figure 6-15: Fan static pressure rise vs. Volume flow rate for a blade root pitch angle of 30° and inlet angle of 00°

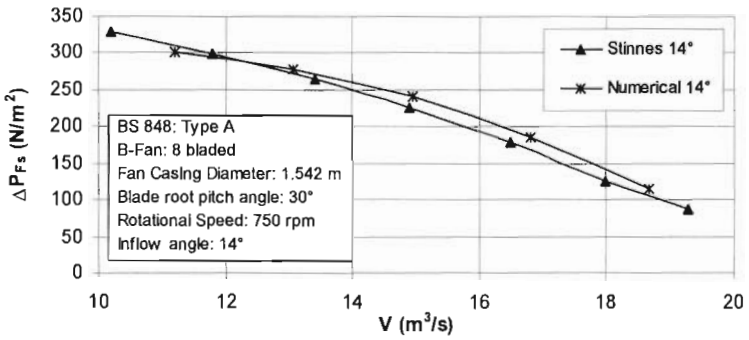

Figure 6-16: Fan static pressure rise vs. Volume flow rate for a blade root pitch angle of 30° and inlet angle of 14°

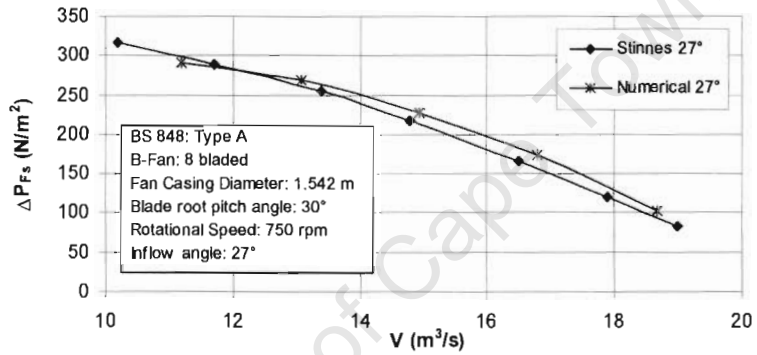

Figure 6-17: Fan static pressure rise vs. Volume flow rate for a blade root pitch angle of 30° and inlet angle of 27°

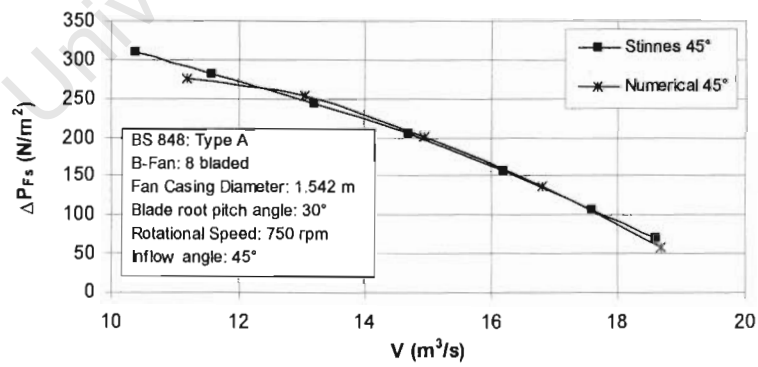

Figure 6-18: Fan static pressure rise vs. Volume flow rate for a blade root pitch angle of 30° and inlet angle of 45°

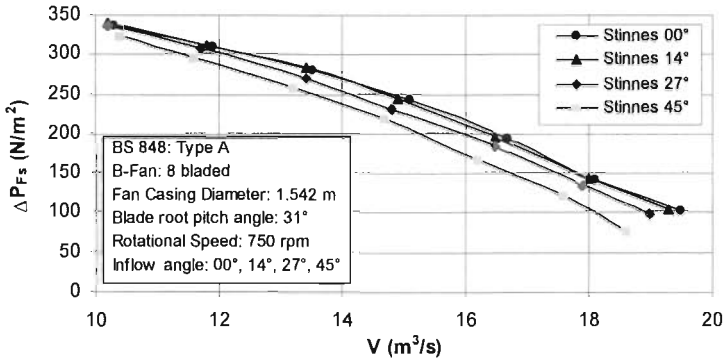

Figure 6-19: Experimental data for Fan static pressure rise vs. Volume flow rate for a blade root pitch angle of 31° and inlet angles of 00°, 14°, 27° and 45°

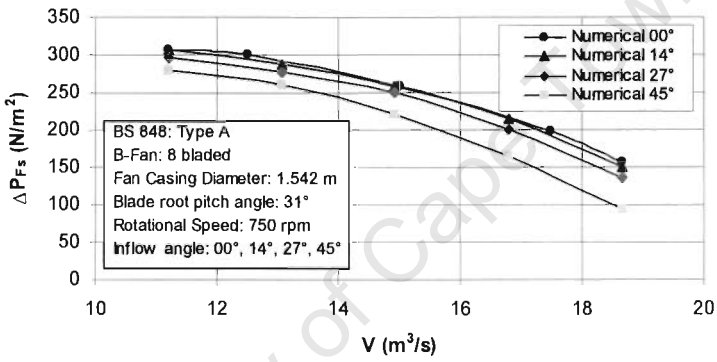

Figure 6-20: Numerical results for Fan static pressure rise vs. Volume flow rate for a blade root pitch angle of 31° and inlet angles of 00°, 14°, 27° and 45°

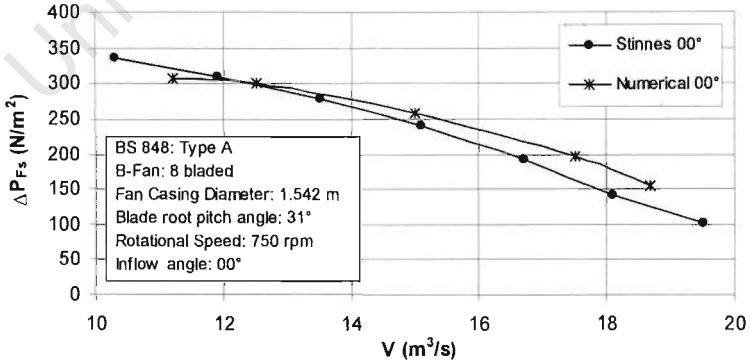

Figure 6-21: Fan static pressure rise vs. Volume flow rate for a blade root pitch angle of 31° and inlet angle of 00°

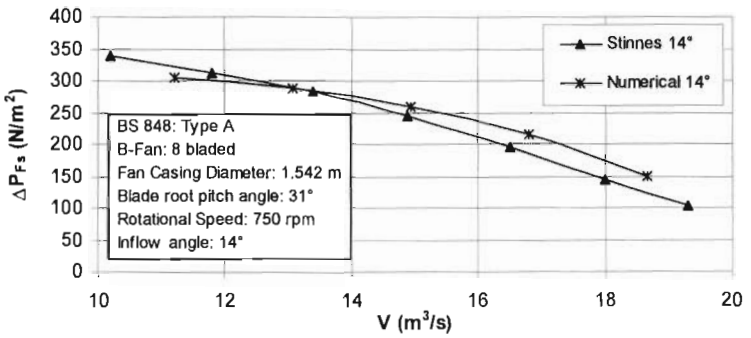

Figure 6-22: Fan static pressure rise vs. Volume flow rate for a blade root pitch angle of 31° and inlet angle of 14°

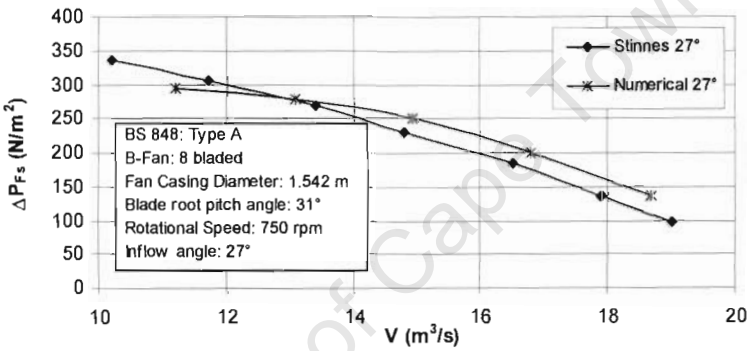

Figure 6-23: Fan static pressure rise vs. Volume flow rate for a blade root pitch angle of 31° and inlet angle of 27°

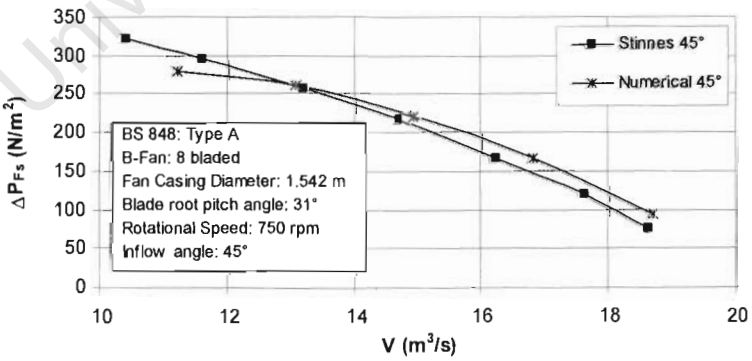

Figure 6-24: Fan static pressure rise vs. Volume flow rate for a blade root pitch angle of 31° and inlet angle of 45°

6.2.2 *Fan power consumption*

Consistent with results for axially aligned upstream flow, fan power consumption is under predicted by the model for cross-flow upstream conditions. As noted by Stinnes and von Backström [19], and demonstrated graphically in figures 6-25 and 6-31, off-axis upstream flow-angles of up to 45° have no measurable effect on fan power characteristics. This trend was confirmed by the computational model, with numerical results shown in figures 6-26 and 6-32. A comparison of individual curves for different cross-flow angles is shown in figures 6-27 to 6-30, and 6-33 to 6-36.

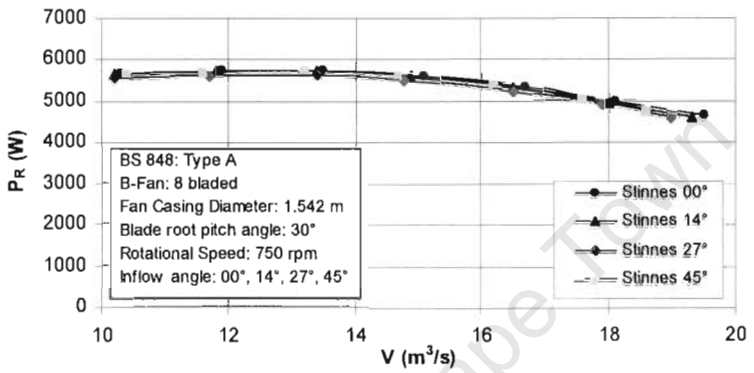

Figure 6-25: Experimental data for Fan power consumption vs. Volume flow rate for a blade root pitch angle of 30° and inlet angles of 00°, 14°, 27° and 45°

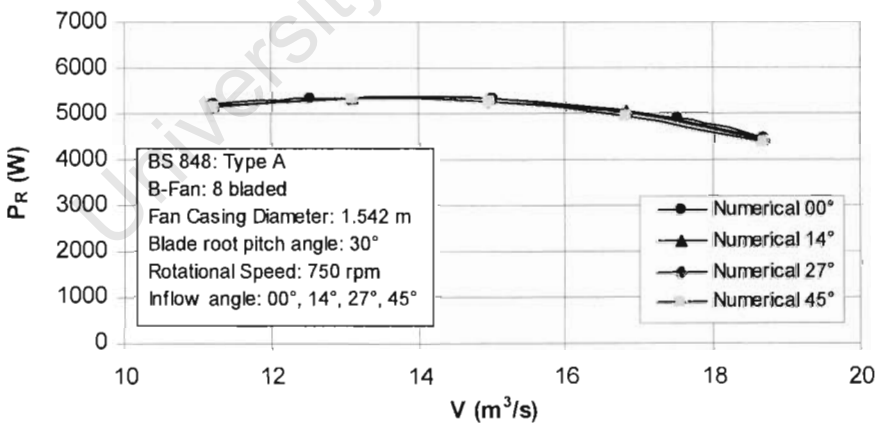

Figure 6-26: Numerical results for Fan power consumption vs. Volume flow rate for a blade root pitch angle of 30° and inlet angles of 00°, 14°, 27° and 45°

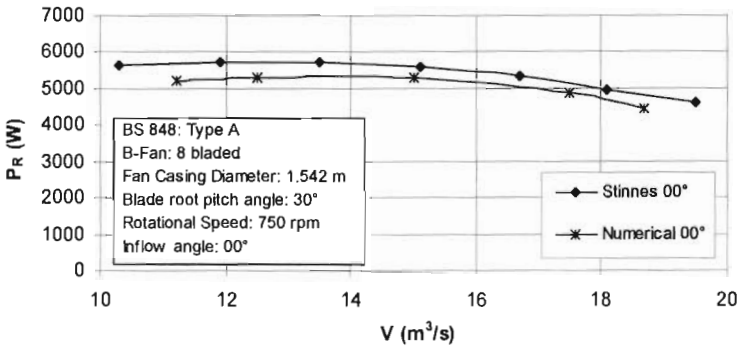

Figure 6-27: Fan static power consumption vs. Volume flow rate for a blade root pitch angle of 30° and inlet angle of 00°

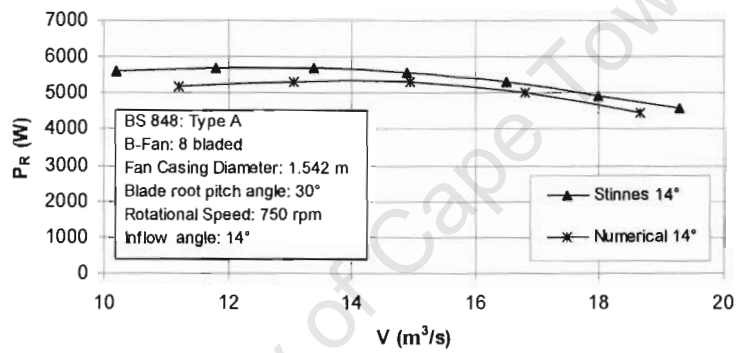

Figure 6-28: Fan power consumption vs. Volume flow rate for a blade root pitch angle of 30° and inlet angle of 14°

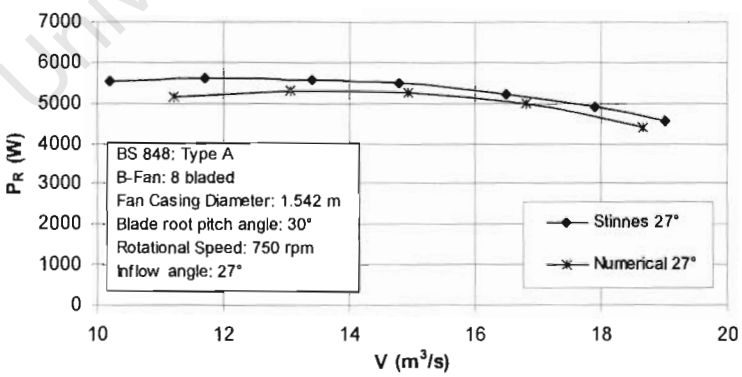

Figure 6-29: Fan power consumption vs. Volume flow rate for a blade root pitch angle of 30° and inlet angle of 27°

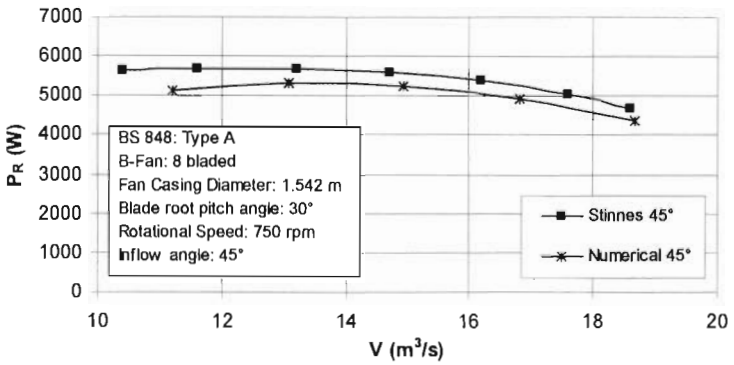

Figure 6-30: Fan power consumption vs. Volume flow rate for a blade root pitch angle of 30° and inlet angle of 45°

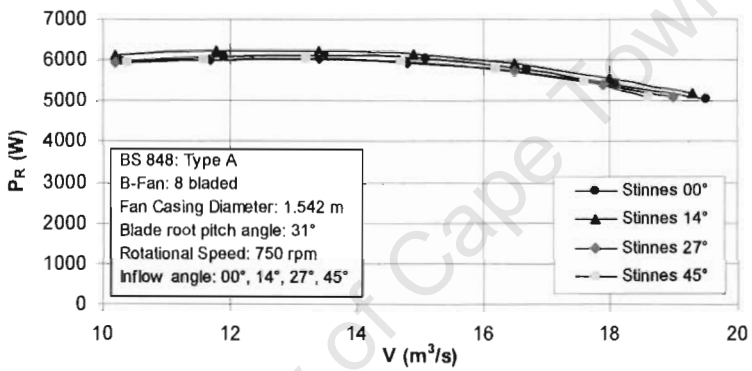

Figure 6-31: Experimental data for Fan power consumption vs. Volume flow rate for a blade root pitch angle of 31° and inlet angles of 00°, 14°, 27° and 45°

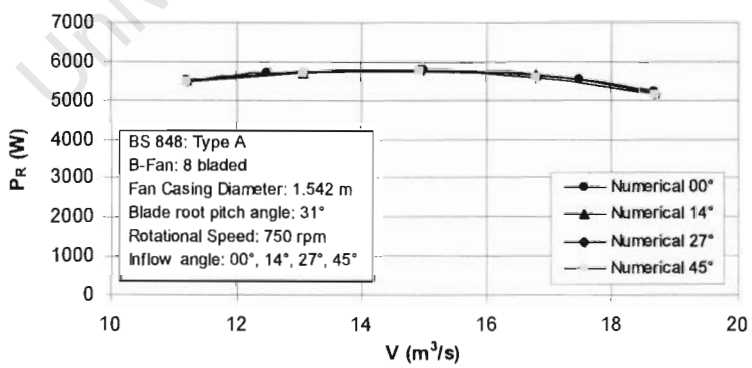

Figure 6-32: Numerical results for Fan power consumption vs. Volume flow rate for a blade root pitch angle of 31° and inlet angles of 00°, 14°, 27° and 45°

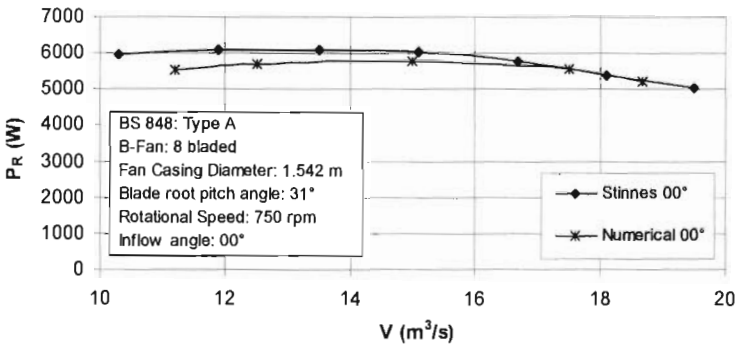

Figure 6-33: Fan power consumption vs. Volume flow rate for a blade root pitch angle of 31° and inlet angle of 00°

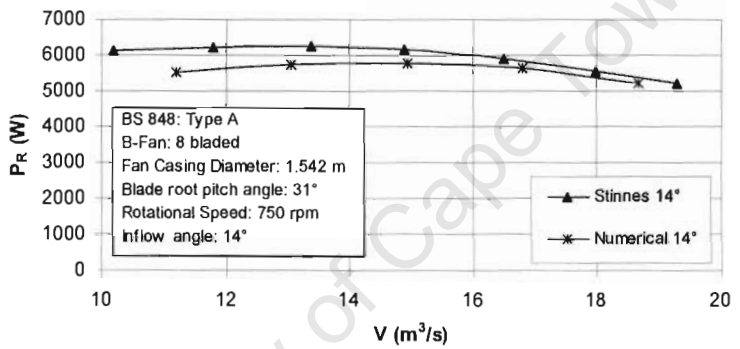

Figure 6-34: Fan power consumption vs. Volume flow rate for a blade root pitch angle of 31° and inlet angle of 14°

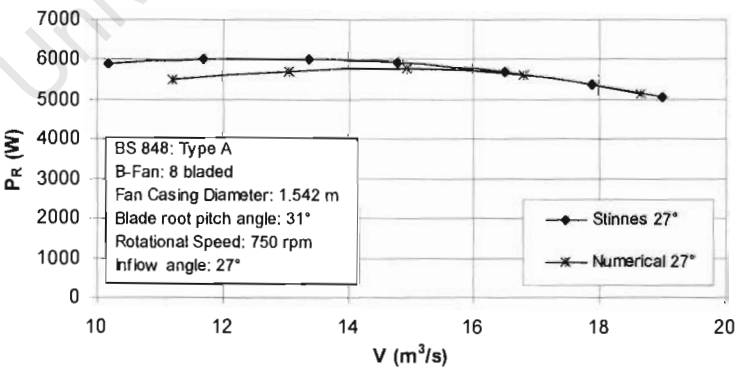

Figure 6-35: Fan power consumption vs. Volume flow rate for a blade root pitch angle of 31° and inlet angle of 27°

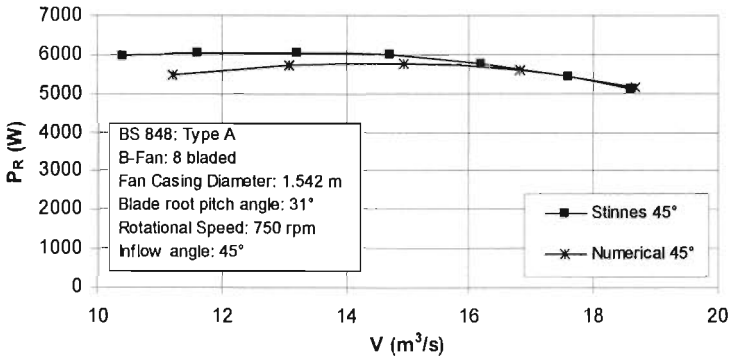

Figure 6-36: Fan power consumption vs. Volume flow rate for a blade root pitch angle of 31° and inlet angle of 45°

6.2.3 Fan static efficiency

Once again, characteristics of the rotor model for axial flow upstream conditions are carried over to off-axis upstream flows, with the static efficiency being over-predicted. However, a comparison between Figure 6-37, showing experimental data, and Figure 6-38, displaying numerical results, indicates that flow trends are well represented for the various upstream duct-angles. The same comparison may be made between figures 6-43 and 6-44, for a blade root pitch angle of 31°, while in the remaining figures individual comparisons are made for each of the off-axis flows simulated.

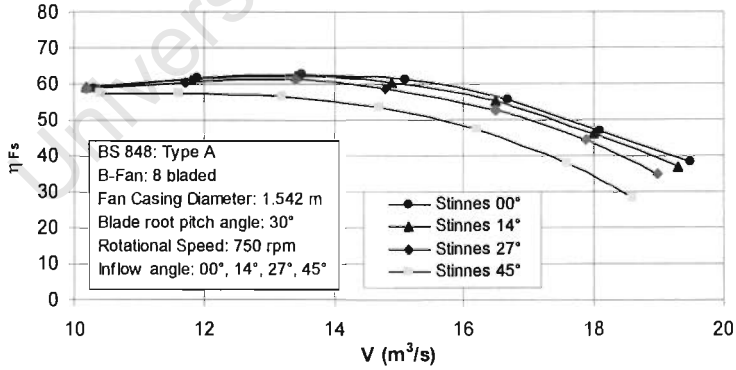

Figure 6-37: Experimental data for Fan static efficiency vs. Volume flow rate for a blade root pitch angle of 30° and inlet angles of 00°, 14°, 27° and 45°

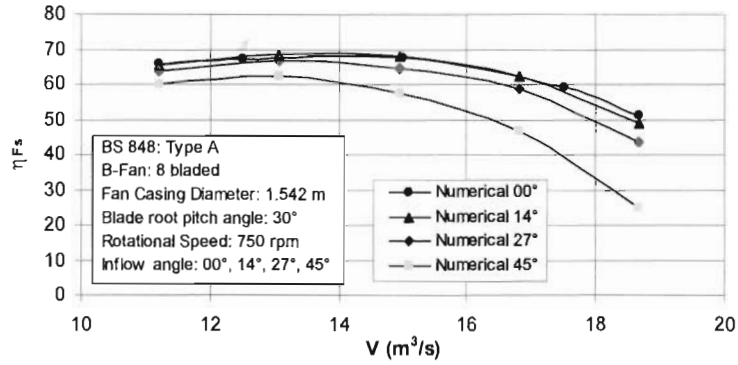

Figure 6-38: Numerical results for Fan static efficiency vs. Volume flow rate for a blade root pitch angle of 30° and inlet angles of 00°, 14°, 27° and 45°

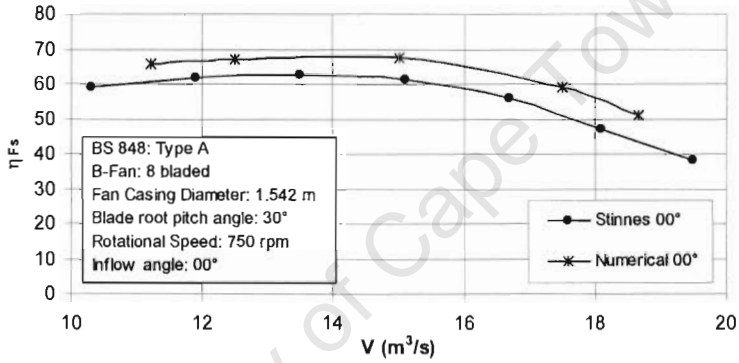

Figure 6-39: Fan static efficiency vs. Volume flow rate for a blade root pitch angle of 30° and inlet angle of 0°

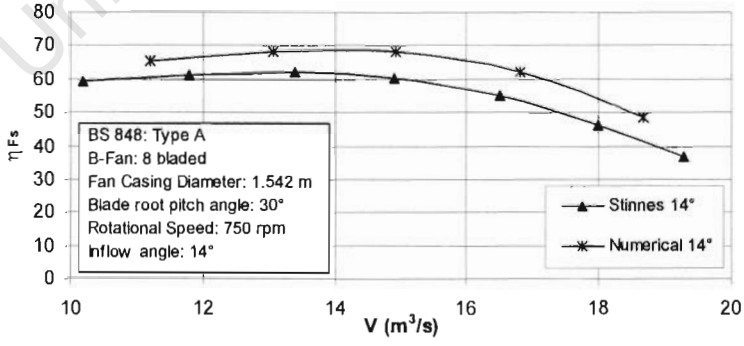

Figure 6-40: Fan static efficiency vs. Volume flow rate for a blade root pitch angle of 30° and inlet angle of 14°

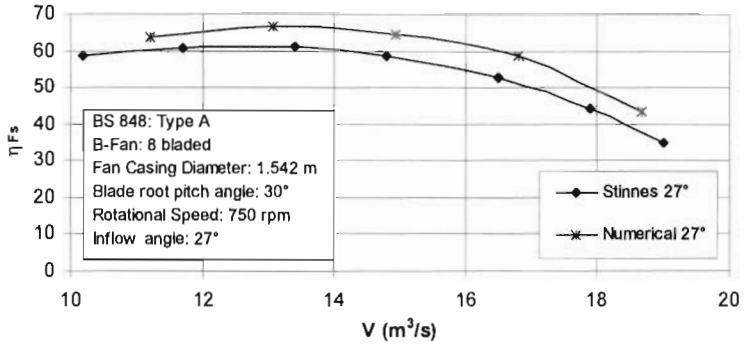

Figure 6-41: Fan static efficiency vs. Volume flow rate for a blade root pitch angle of 30° and inlet angle of 27°

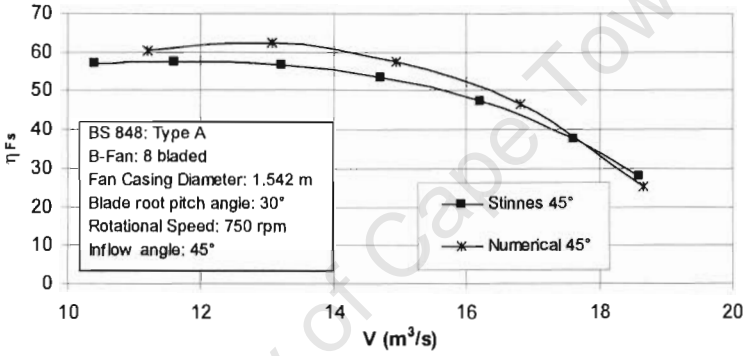

Figure 6-42: Fan static efficiency vs. Volume flow rate for a blade root pitch angle of 30° and inlet angle of 45°

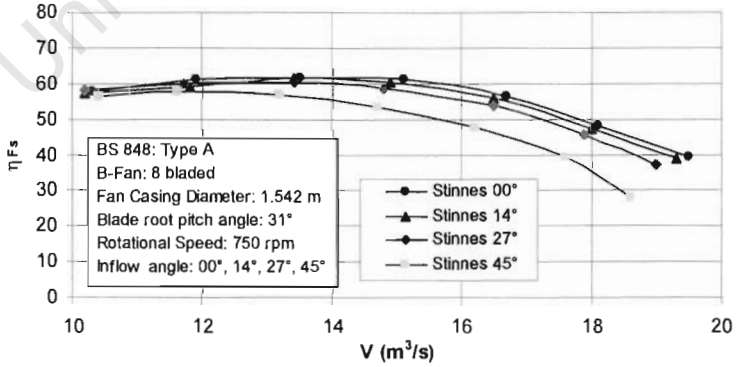

Figure 6-43: Experimental data for Fan static efficiency vs. Volume flow rate for a blade root pitch angle of 31° and inlet angles of 00°, 14°, 27° and 45°

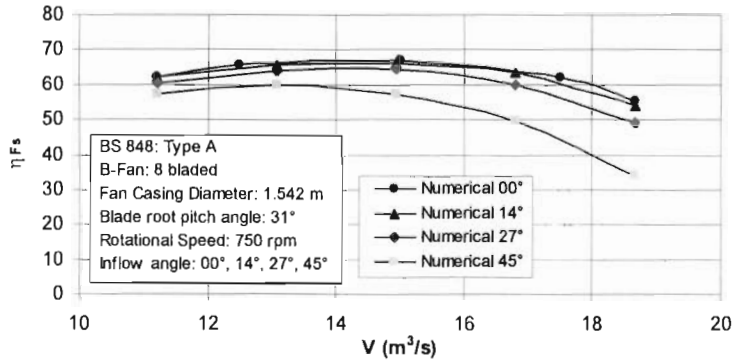

Figure 6-44: Numerical results for Fan static efficiency vs. Volume flow rate for a blade root pitch angle of 31° and inlet angles of 00°, 14°, 27° and 45°

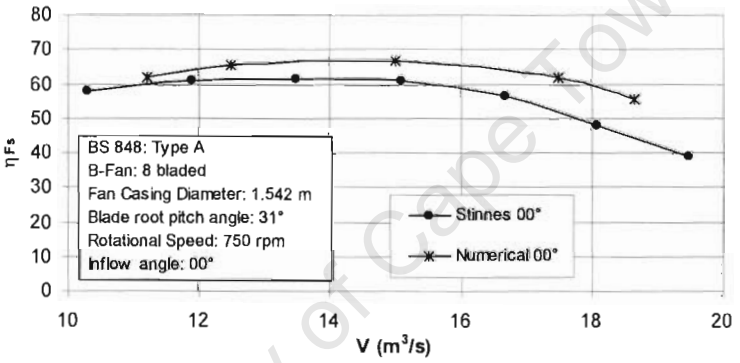

Figure 6-45: Fan static efficiency vs. Volume flow rate for a blade root pitch angle of 31° and inlet angle of 00°

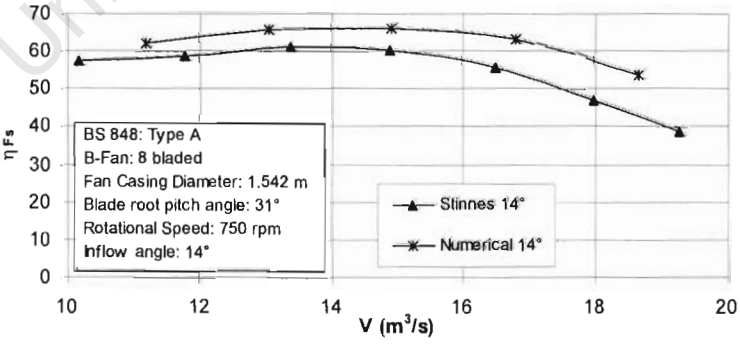

Figure 6-46: Fan static efficiency vs. Volume flow rate for a blade root pitch angle of 31° and inlet angle of 14°

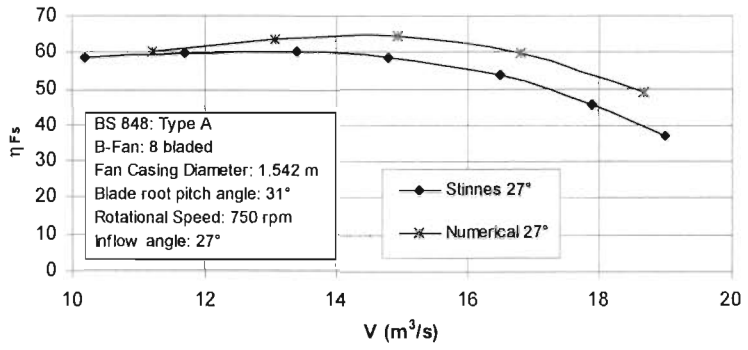

Figure 6-47: Fan static efficiency vs. Volume flow rate for a blade root pitch angle of 31° and inlet angle of 27°

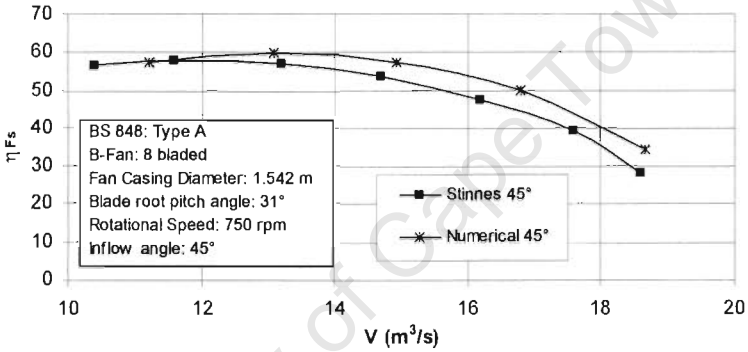

Figure 6-48: Fan static efficiency vs. Volume flow rate for a blade root pitch angle of 31° and inlet angle of 45°

7 APPLICATION OF THE ROTOR MODEL TO ANALYSIS OF AN HELICOPTER EXTERIOR FLOWFIELD

In previous chapters, the validity of using the developed rotor model to simulate the flow-field in the vicinity of a fan or rotor has been clearly demonstrated. Its ability to produce accurate downstream flow characteristics corresponding to flow-rate, angle of attack, and upstream approach angle, will allow the application of this model to the analysis of helicopter exterior flow-fields.

A series of numerical simulations, integrating the rotor-model with the CIRSTEL (Combined Infra-Red Suppression and Tail rotor Elimination) helicopter fuselage, were carried out to demonstrate the capabilities of the model. No experimental data was available for validation purposes. However, the model was used to produce flow characteristics for a series of helicopter flight conditions, which are shown in graphical terms. The flight conditions investigated were hover with no ground effect, hover close to the ground, take-off, vertical ascent, and level forward flight.

In this chapter, the CIRSTEL project is briefly described, together with a description of the rotor model configuration, computational grid, and boundary conditions used for this investigation. The results for each simulation are discussed, with the characteristics of the exterior flow-field around the helicopter presented graphically.

7.1 Description of the CIRSTEL Helicopter prototype

In order to determine the performance of the rotor model when coupled with an helicopter geometry, the rotor-model was integrated with the fuselage of a modified Alouette III helicopter, the CIRSTEL prototype, developed by Denel Aviation. The reasons for choosing this particular helicopter were related to the reported poor performance of the air intake openings cut into the modified Alouette III structure. Simulations were carried out focusing on the external flow-field characteristics around the helicopter fuselage, with the expectation that this information would aid in the synthesis of more effective air intake designs. A configuration of the prototype helicopter is shown in Figure 7-1 below, followed by a brief explanation of the CIRSTEL concept.

Figure 7-1: A configuration of the CIRSTEL prototype helicopter [21]

The CIRSTEL prototype incorporates the use of a specially modified tail-boom system to eliminate the need for a tail rotor. Slots along the length of the tail-boom blow air tangentially along the boom surface, relying on what is known as the Coanda effect to create circulation around the boom (The Coanda effect describes the tendency of fluid to follow a solid surface which is slightly curved away from the stream). When subjected to downwash from the rotor, the aerodynamic interactions along the tail-boom result in an horizontal lift vector, countering the main rotor torque. Manoeuvring adjustments are controlled through the use of tail thruster vents.

This concept, often termed NOTAR, for "NO TAil Rotor", is shown schematically below. In addition to the elimination of the tail rotor, CIRSTEL introduces several unique features aimed at in increased efficiency and control of the circulation boom system, as well as reduction of the infra-red signature of the exhaust gases.

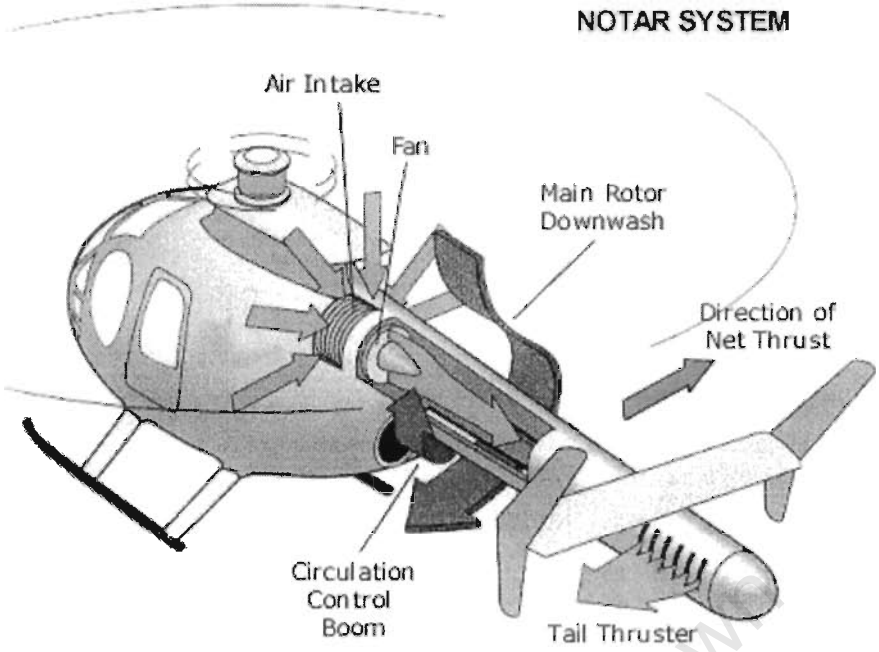

Figure 7-2: A schematic representation of the NOTAR concept employed on the CIRSTEL prototype [21]

7.2 Rotor Model Configuration

In order to use the rotor model successfully as a representation of the CIRSTEL main rotor, critical information about the rotor system was required. This included the rotational speed, blade profiles and dimensions, and number of blades. The characteristics used in this investigation for the prototype Alouette III CIRSTEL main rotor are given in Table 7-1 below. These values were used as inputs in the rotor model code, as well as defining the construction of the actuator disk within the computational domain.

Table 7-1: Main rotor characteristics for the Alouette III CIRSTEL prototype [21]

Rotational speed (rpm)	Number of blades	Blade profile	Blade chord (m)	Rotor diameter (m)	Hub diameter (m)	Blade angle of twist (deg/m)
350	3	NACA 0012	0.265	11.02	2.30	-1.66

Lift and drag characteristics for the rotor blades are described as a function of effective angle of attack for angles from -180° to 180°, shown in Figure 7-3 below. For small angles of attack, these curves were obtained from experimentally generated airfoil lift and drag characteristics for the NACA 0012 profile. For the range of attack angles for which experimental data was not available, the aerodynamic characteristics of a flat plate were used, being smoothly integrated with the airfoil data to produce continuous lift and drag curves.

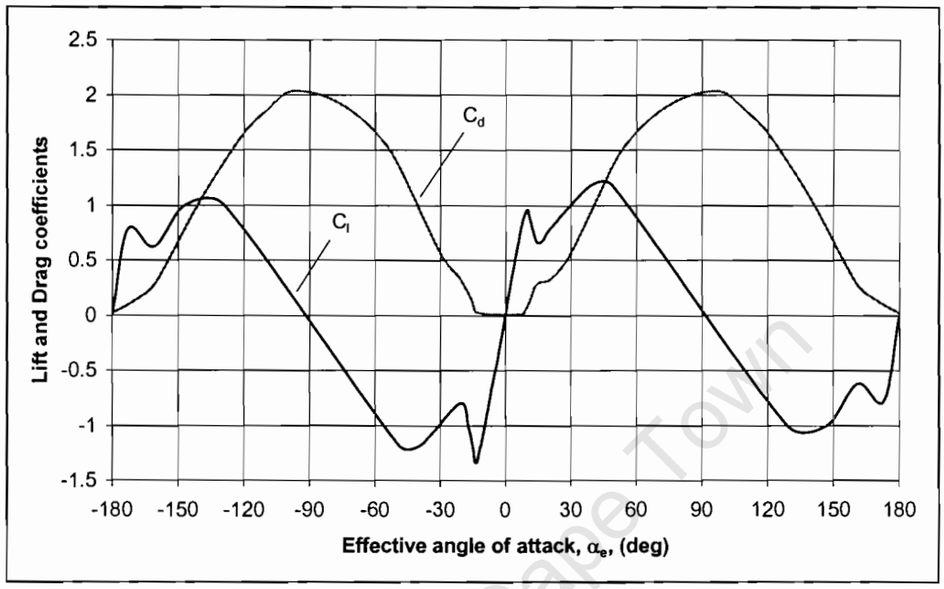

Figure 7-3: Lift and drag coefficients as a function of angle of attack, used for calculation of the aerodynamic forces at the blade elements defined in the rotor model [21]

A subroutine was included in the rotor model to define the cyclic pitch profile of the rotor in forward flight. It is necessary in helicopters to vary the blade pitch angles as a function of azimuth angle, to account for the free-stream velocity component in forward flight. Controlling the geometric angle of attack of the blades serves to keep the effective angle of attack constant for advancing and retreating blades. This is to prevent pitching moments being created by unequal aerodynamic load characteristics along diametrically opposing blades. In the current simulations, the relationship

between the geometric angle of attack and the rotor azimuth angle is described by the equation

$$\gamma = A_0 - A_1 \cos\psi - B_1 \sin\psi - \frac{r}{R}\alpha_t \qquad (27)$$

where A_0 is the collective pitch angle, A_1 and B_1 define the cyclic pitch angle, r is the element radial position, R is the rotor tip radius, and α_t the angle of twist at the rotor tip.

In this investigation, the cyclic pitch coefficients A_1 and B_1 were not optimised. Values for these coefficients were estimated based on values reported by Chaffin and Berry [6], for similar rotor characteristics and advance ratios. An example of the coefficients used for an advance ratio of 0.15 is given in Table 7-2 below. (The advance ratio is a commonly used value used to describe the velocity of a helicopter with respect to its rotor speed. It is defined as the ratio of free-stream velocity and rotor blade tip-speed, $\mu = v_\infty / v_t = v_\infty / \Omega.R$)

Table 7-2: Cyclic pitch values used for forward flight at an advance ratio of 0.15 [6]

Advance ratio, μ	A0	A1	B1	r/R	$\gamma_{t\,(deg)}$
0.15	12.0	-1.11	3.23	0.75	-7.24

Figure 7-4 shows the corresponding geometric angle of incidence as a function of azimuth angle. The azimuth angle is measured clockwise when viewed from above, with the zero–angle vector pointing rearwards along the helicopter fuselage, the global negative x-axis.

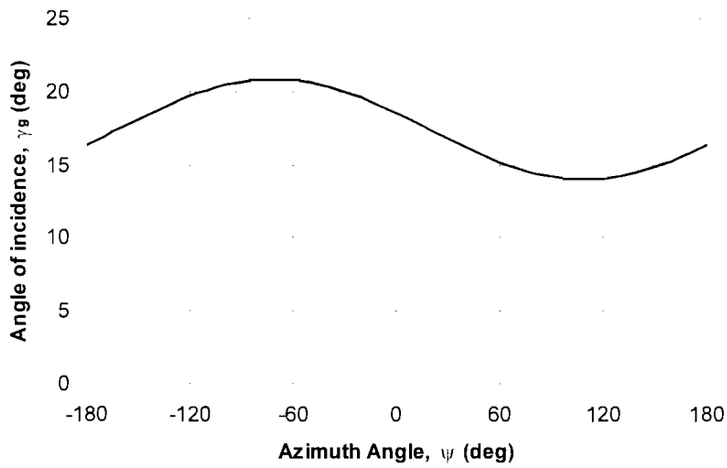

Figure 7-4: Geometric angle of attack shown as a function of rotor azimuth angle

7.3 Computational Grid

The fuselage structure of the CIRSTEL helicopter was obtained in a solid model format from a postgraduate student who had completed some previous work on the CIRSTEL, Mr. René Heise, of the University of Stellenbosch [21]. The geometry model used in this investigation did not include any of Mr. Heise's modifications to the air intakes, being the original CIRSTEL prototype structure shown in Figure 7-1.

The computation grids for this investigation were created in the Fluent pre-processor, Gambit. Apart from the structured actuator disk region, the computational domain was meshed using an unstructured grid. This allowed relatively simple manipulation of the grid density around the non-regular shape of the helicopter fuselage.

In order to simplify the process of modifying the shape and size of the atmospheric region modelled for the various flight conditions, a block containing just the helicopter and actuator disk, as well as closely surrounding atmosphere, was created and meshed. With this geometry retained, only the surrounding region of atmosphere modelled in the computational domain need be changed for different simulation scenarios.

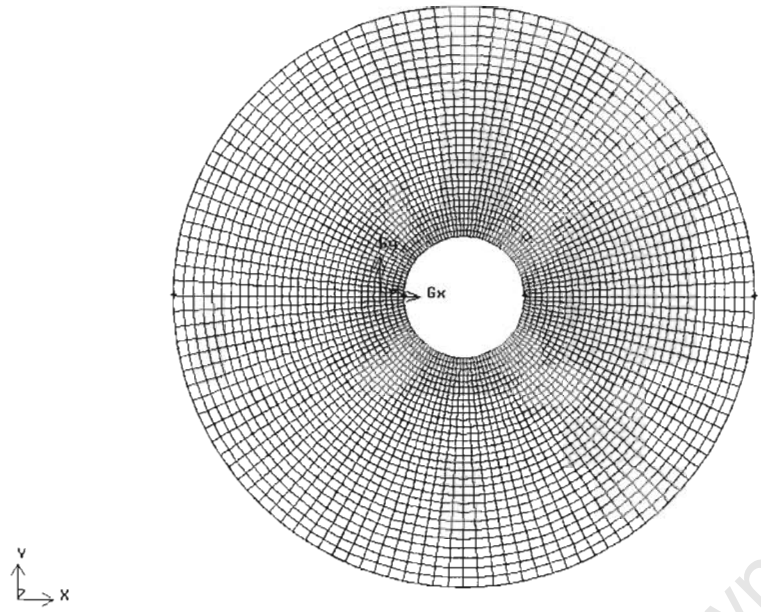

Figure 7-5: Plan view of the actuator disk grid used to model the rotor for simulations of the CIRSTEL helicopter exterior flow-field

As required by the rotor model code, the actuator disk region was meshed using a regular structured grid, shown in Figure 7-5 above. 30 elements were used in the radial direction, spaced at a progressive size ratio of 1.02 to keep the proportions of the cells regular. 120 equally spaced elements were used around the circumference, to make up an actuator disk containing 3600 cells. A thickness of 40mm was used for the actuator disk, upstream and downstream disks, with an axial spacing of 160mm between zones. The dimensions of the actuator disk were based on the Alouette III main rotor dimensions, described in Table 7-1. In Figure 7-6 below, a section through the actuator disk region shows the different zones used in the rotor model.

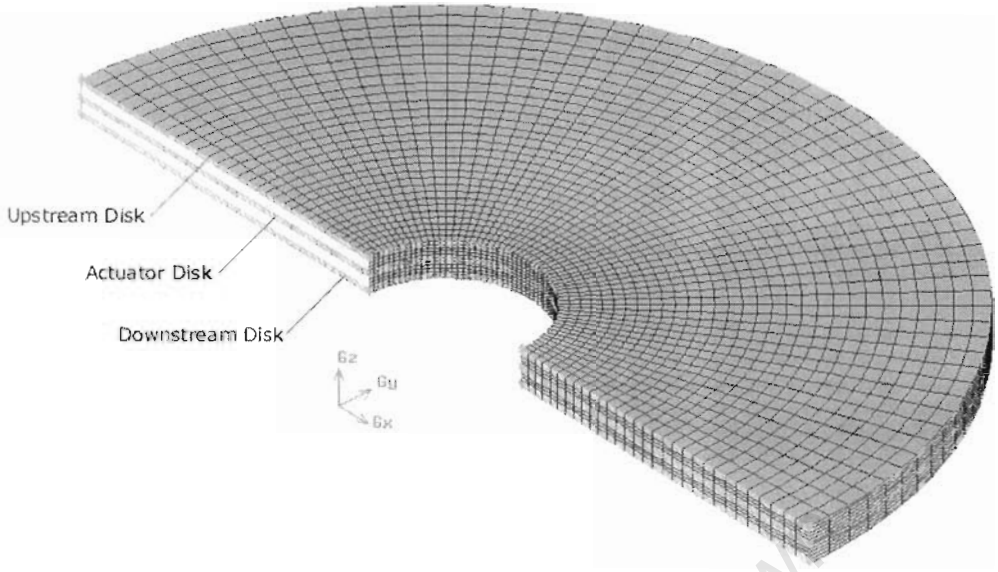

Figure 7-6: A section view through the actuator disk region, showing the disk-zones used in the rotor code

In the region surrounding the helicopter and actuator disk, sharp gradients in flow properties were expected due to the rotor downwash and flow interactions around the body-structure. A sizing function was used to refine the unstructured mesh size in this critical region, and to control the rate at which the grid would become progressively courser moving outwards towards the domain boundaries.

An initial grid size of 120mm was specified for meshing the helicopter fuselage, using a growth rate of 1.05 (The growth rate defines the size ratio of the current row of elements to the previous row's elements). Other size function values used for controlling the grid structure are given in Table 7-3 below, with the meshed fuselage of the CIRSTEL shown in Figure 7-7.

Table 7-3: Size function values used to refine the computational grid in the region of the helicopter

	Initial element size (mm)	Element growth rate	Maximum element size (mm)
Helicopter body	120	1.05	400
Actuator disk region: Up/Downstream faces	160	1.05	400
Actuator disk region: Edge faces	40	1.2	400
Helicopter region boundaries	240	1.1	1000

Figure 7-7: Computation grid describing the CIRSTEL helicopter fuselage

The use of size functions allowed greater control over the computational grid. This permitted the total number of grid elements to be reduced significantly, without necessarily sacrificing computational accuracy and stability, since the grid could be refined in critical regions, while retaining a course structure in the majority of the computational domain. This is demonstrated in figures 7-8 to 7-11, showing the

CIRSTEL fuselage and structured actuator disk region embedded in an unstructured mesh. Mesh refinement in the locality of the helicopter is evident, with the grid becoming increasingly course towards the domain boundaries.

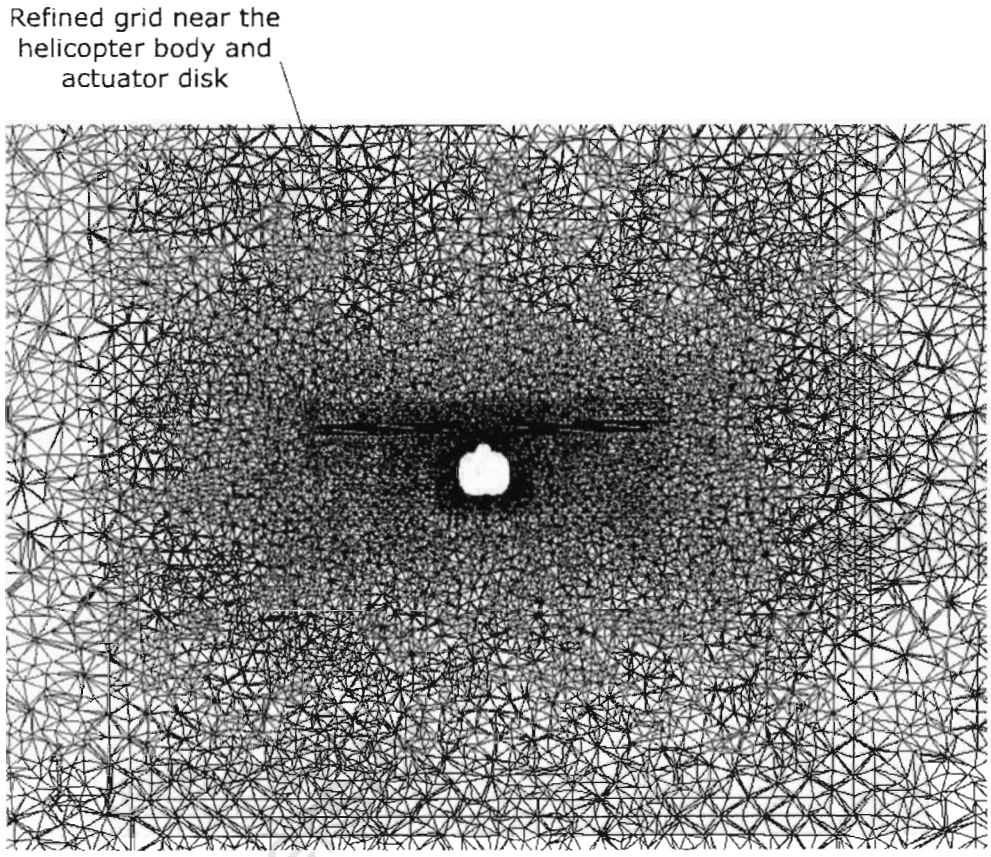

Figure 7-8: Computational grid around the helicopter fuselage

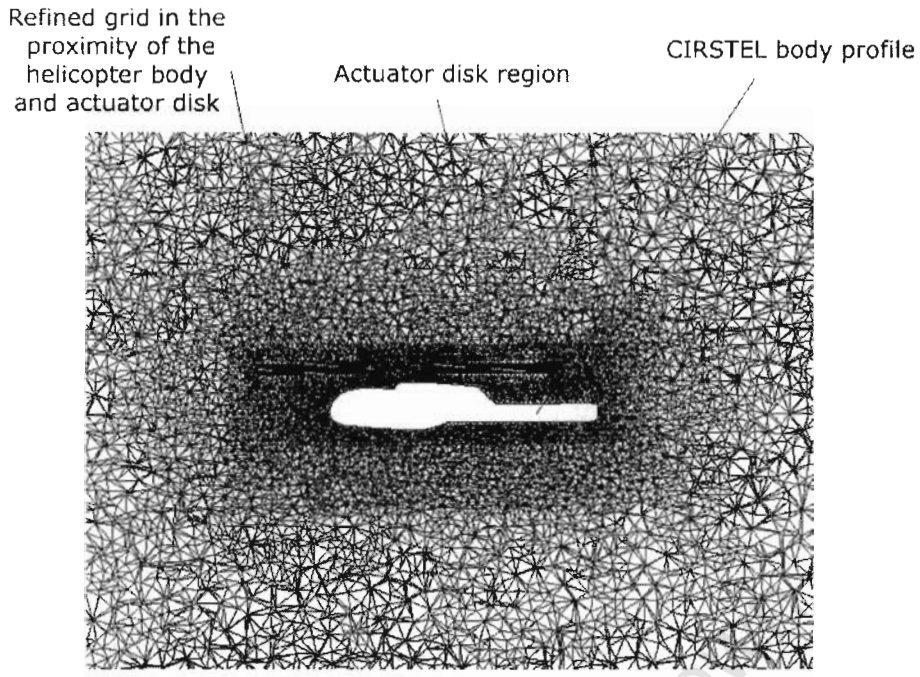

Figure 7-9: Computational grid around the helicopter fuselage

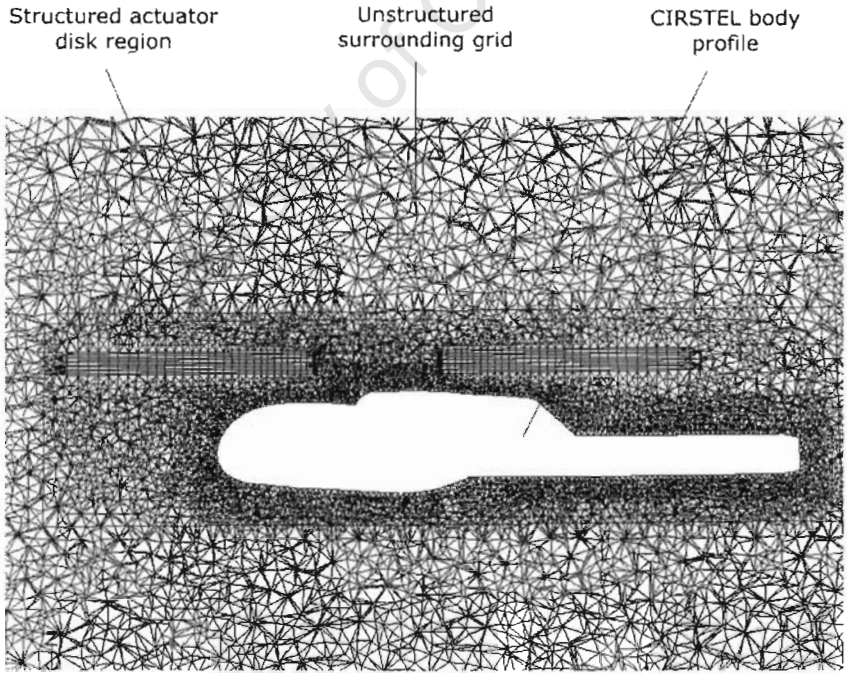

Figure 7-10: Detailed view of the computational grid around the helicopter fuselage, showing the structured actuator disk region embedded within an unstructured grid

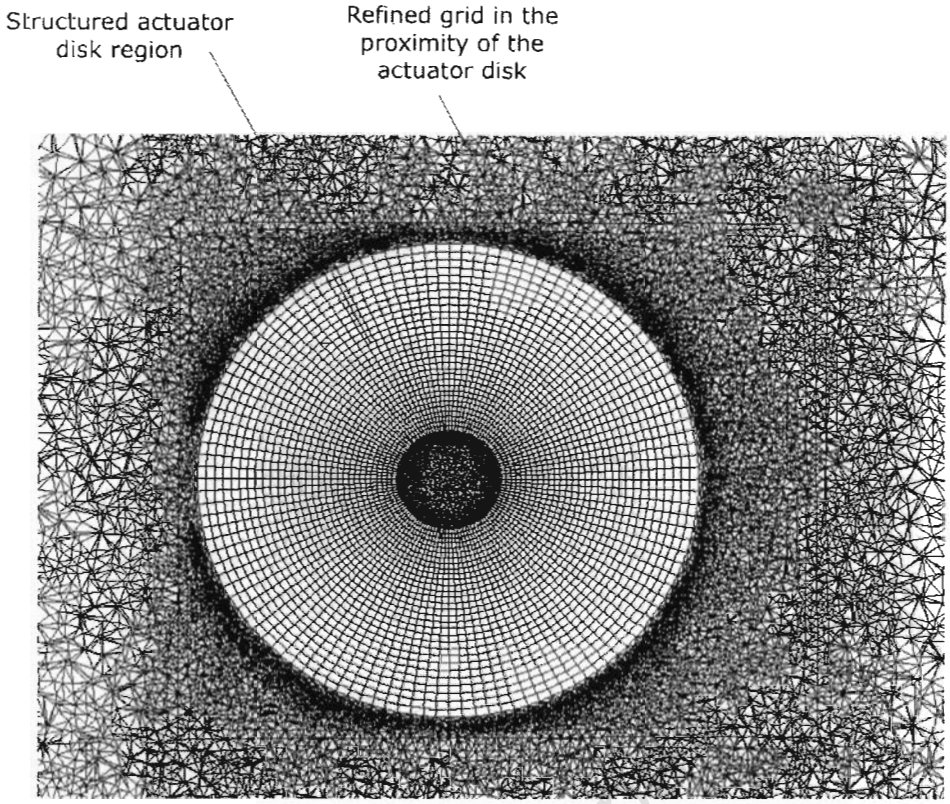

Figure 7-11: Plan view of the computational grid in the region of the actuator disk

On average, between 1.7 and 2.1 million grid elements were used in each simulation, depending on the size and shape of the atmospheric region used. This information, together with dimensions for each computational domain, is summarized in Table 7-4 below.

Table 7-4: Computation domain sizes for the CIRSTEL flight conditions investigated

Flight condition	Computational domain: X, Y, Z (m)	Number of grid elements
Hover, no ground effect	35x35x35	1875230
Hover, 15m	35x35x35	1875230
Hover, 5m	50x50x25	2048369
Take-off	40x40x15	1730166
Vertical ascent	30x30x50	2092668
Level forward flight	60x30x40	1897602

7.4 Boundary conditions

A combination of different boundary conditions were used for each flight condition simulated. A full comparative study of different boundary condition options was not possible however, as no experimental data was available for validation purposes. The primary concern was therefore numerical stability and convergence of the solution. Residuals for the velocity, turbulence and continuity equations were used in establishing convergence. The boundary conditions referred to here are described more fully in section 3.4 of this report.

For both cases of hover, and take-off, the flow within the computational domain was generated entirely by the rotor itself. Initial simulations were carried out for the conditions of hover, first with no ground effect, and then with a Wall boundary added 15m below the helicopter. All boundaries, besides that directly below the helicopter, were defined as Pressure Inlet boundaries. The boundary conditions used for the hover condition are represented in Figure 7-12 below.

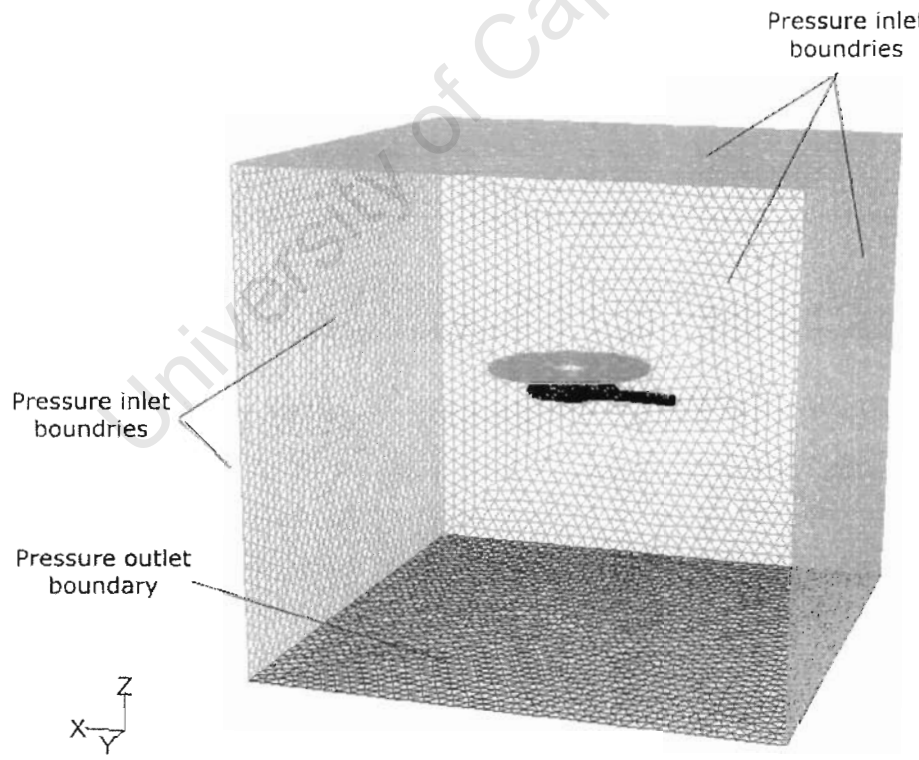

Figure 7-12: Boundary conditions applied to the hover simulations with no ground effect

The boundary conditions applied to the helicopter take-off simulation are shown in Figure 7-13 below. These were similar to the hover conditions, the difference being the close proximity of a Wall boundary directly below the helicopter fuselage. Other boundaries were specified as Pressure Inlet boundaries.

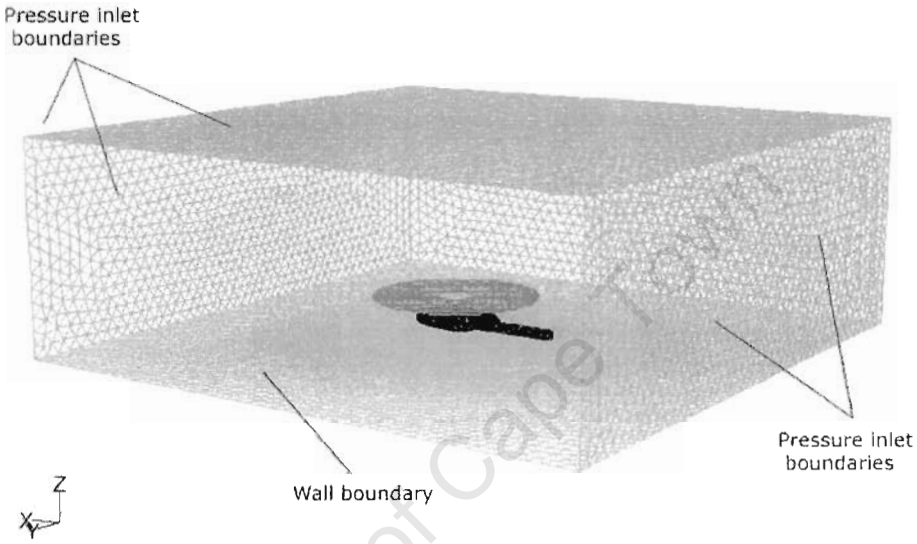

Figure 7-13: Boundary conditions applied to helicopter take-off simulations

In simulations where the helicopter was not stationary, such as vertical ascent and forward flight, a Velocity Inlet boundary was used, defining the magnitude and direction of the free-stream velocity. Directly downstream of the Velocity Inlet faces, a Pressure Outlet boundary was used. Wall boundaries with zero shear (i.e. no viscous friction at the wall) were used on the sides of the computational domain, parallel to the free-stream direction. Boundaries for both vertical and forward flight are shown in figures 7-14 and 7-15 respectively.

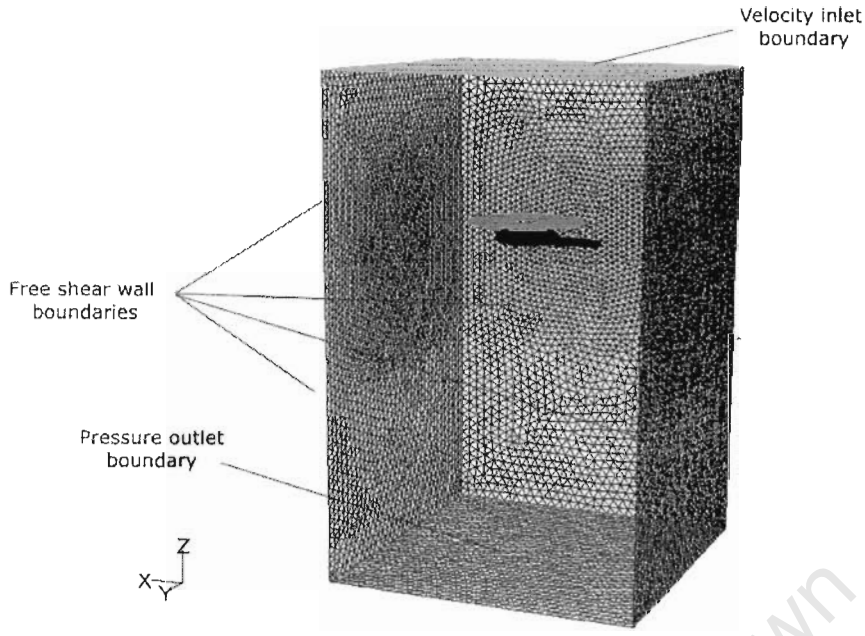

Figure 7-14: Boundary conditions applied to the vertical ascent simulations

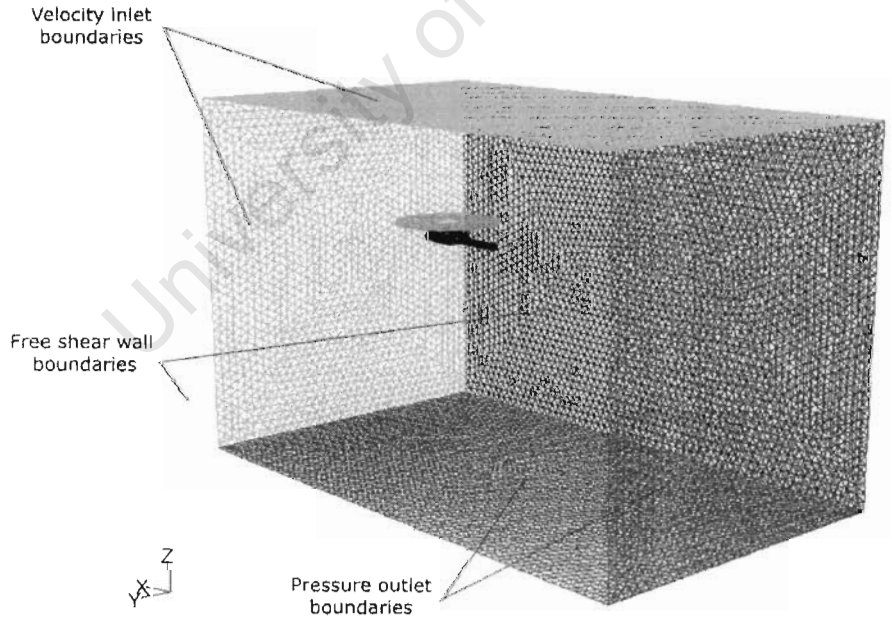

Figure 7-15: Boundary conditions applied to the forward flight simulations

7.5 Numerical results and discussion

The following sections describe numerical results obtained for simulations using the CIRSTEL helicopter fuselage, integrated with the developed rotor model. As previously mentioned, the thrust and pitching moments of the main rotor were not optimised due to the lack of sufficient physical data for this helicopter. This is of consequence particularly in forward flight, due to the interaction between free-stream velocity, and advancing and retreating rotor-blades.

Results are reported chiefly in graphic terms, with the aim being a realistic representation of the helicopter external flow-field, and a demonstration of the potential of the current rotor model for application to more detailed analyses. The results of simulations of the CIRSTEL fuselage with coupled rotor model are presented below, including, hover, with and without ground effect, take-off, vertical ascent and level forward flight.

7.5.1 Hover (no ground interaction)

Simulations completed for the condition of hover, with no ground effect, yielded the graphic results shown in the following figures. Static pressure contours on the fuselage surface are shown in figure 7-16 and 7-17. The asymmetry of the contours is due to the swirl created by the rotating rotor blades. High pressure regions are clearly visible on upper portions of the fuselage, directly below the rotor, while on the sides of the fuselage, near the root of the tail-boom, low pressure regions are evident. It is in this area that the circulation control fan air intakes were cut for the CIRSTEL prototype.

Figure 7-18 demonstrates the velocity magnitude contours around the helicopter fuselage and rotor. The rotor downwash is evident by the higher velocities produced beneath the actuator disk, on either side of and below the fuselage.

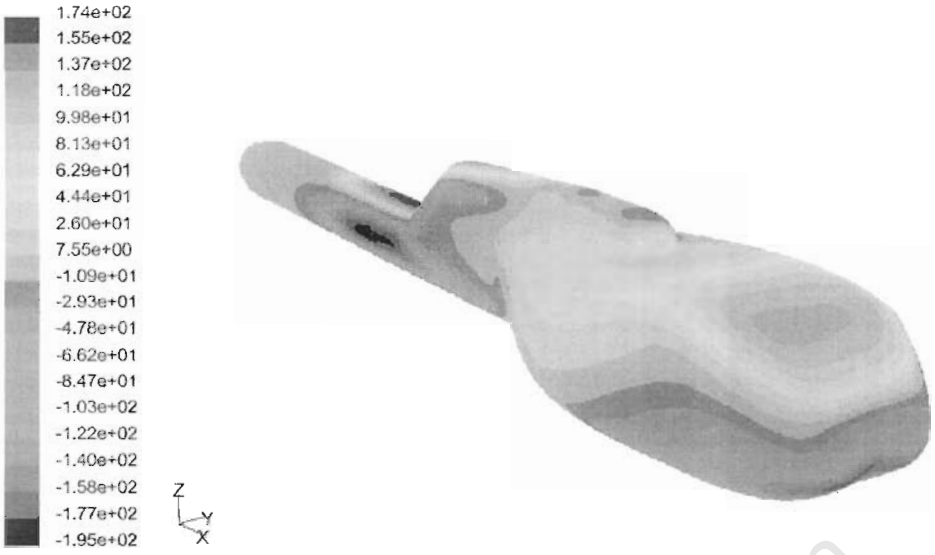

Figure 7-16: Contours of static pressure on the helicopter fuselage surface (Pa)

Figure 7-17: Side and Top views of fuselage surface static pressure contours (Pa)

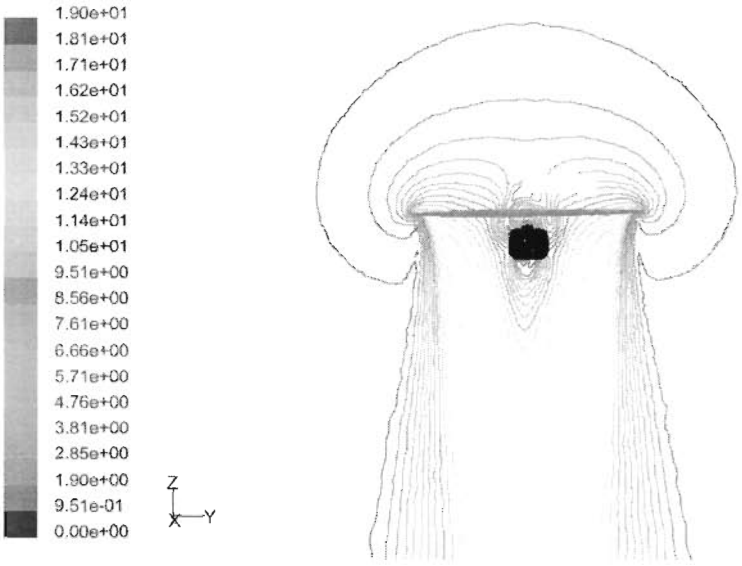

Figure 7-18: Contours of velocity magnitude surrounding the helicopter, shown on the transverse centre-plane of the rotor (m/s)

7.5.2 Hover (15m above the ground plane)

In hover, 15m above the ground, static pressure contours on an XZ plane along the helicopter longitudinal axis are shown in Figure 7-19 below. Static pressure is elevated in the regions between the rotor and the fuselage, with the effect of the ground shown by elevated pressure contours rising from the ground surface below the helicopter.

In Figure 7-20, path-lines are shown for flow through the rotor, initiated above the transverse centre-line of the rotor. The swirl induced by the rotor is demonstrated by the rotation of the path-lines by the time the ground is reached.

Figure 7-19: Contours of static pressure surrounding the helicopter, shown on the helicopter longitudinal centre-plane (Pa)

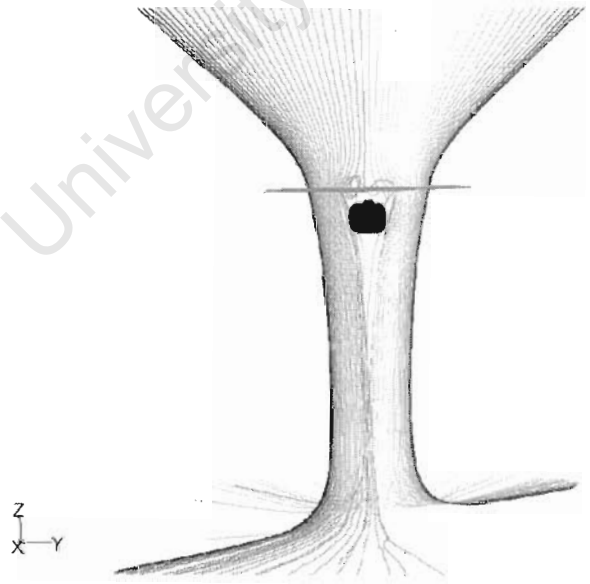

Figure 7-20: Particle path-lines, coloured according to particle, released within the transverse centre-plane of the rotor

7.5.3 Hover (5m above the ground plane)

In hover close to the ground, the interactions between the rotor downwash and the ground are significant. In Figure 7-21, static pressure contours over the fuselage surface are shown. Again, a low pressure region is evident in the region of the CIRSTEL tail-boom fan air-intakes.

Figure 7-22 displays the orientation of the helicopter with respect to the ground, demonstrating the high pressure region created on the ground by the rotor downwash. Figure 7-23 shows the velocity magnitude contours surrounding the helicopter, again on a vertical plane corresponding with the aircraft's longitudinal axis. Path-lines are shown in Figure 7-24 on the same plane. The effects of vortices formed near the rotor hub may be noted in both these figures.

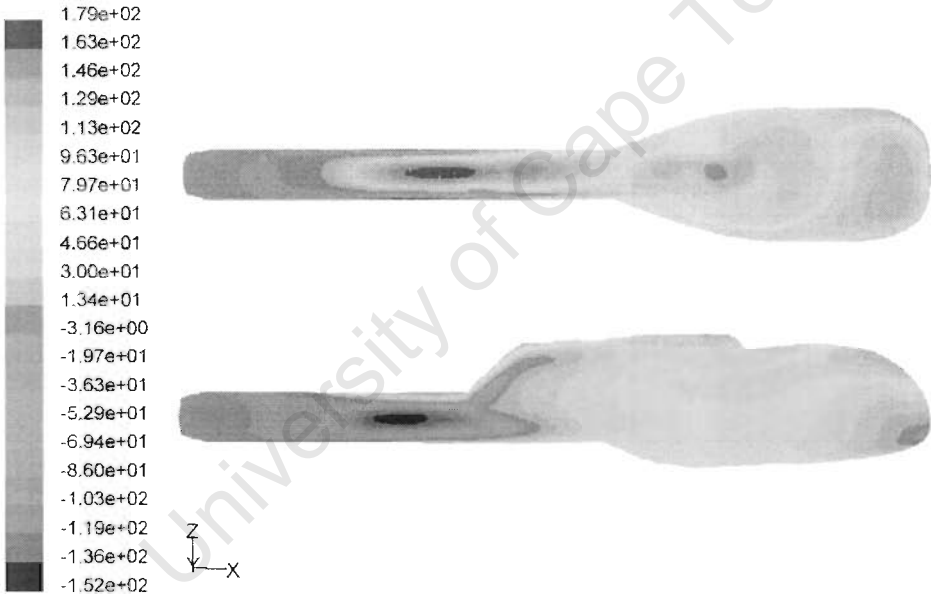

Figure 7-21: Side and Top views of fuselage surface static pressure contours (Pa)

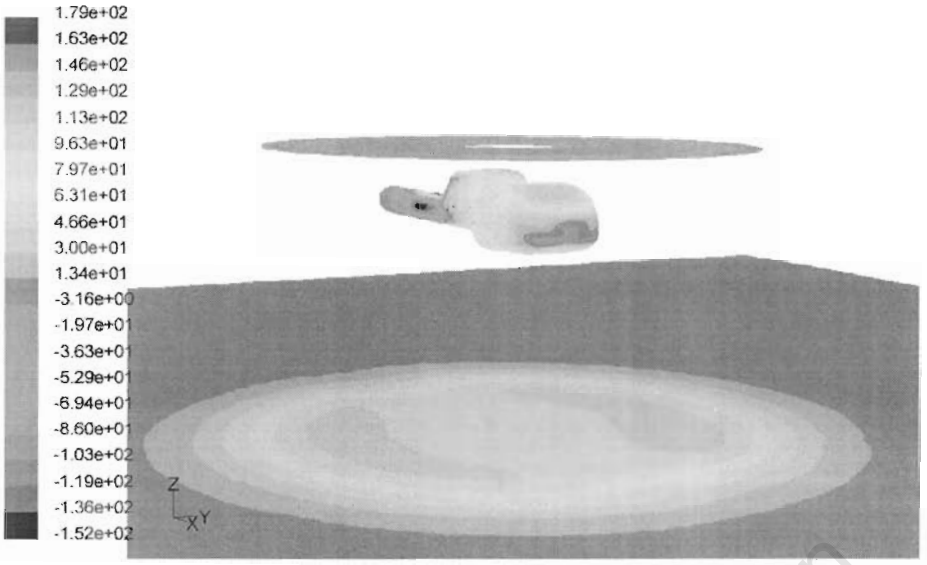

Figure 7-22: Contours of static pressure on the helicopter fuselage and the ground surface 5m below it (Pa)

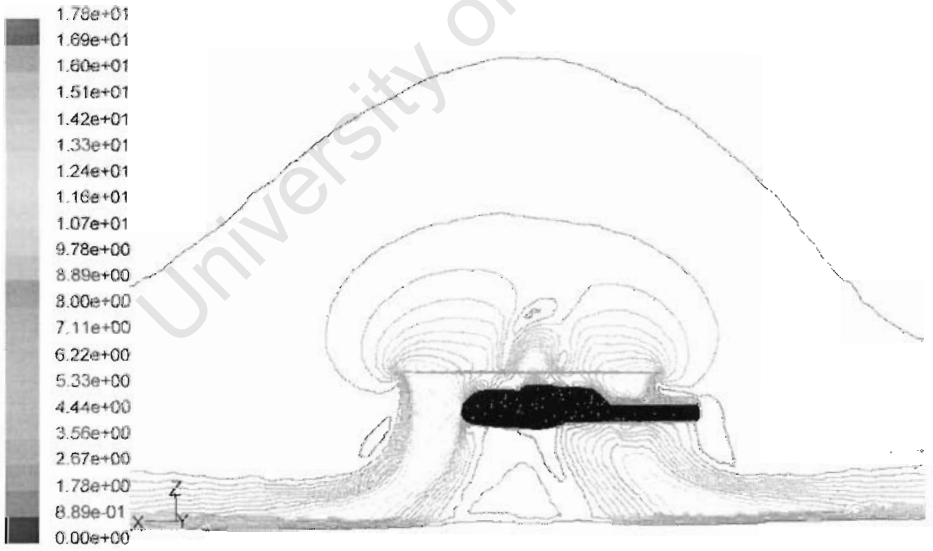

Figure 7-23: Contours of velocity magnitude surrounding the helicopter, shown on the helicopter longitudinal centre-plane (m/s)

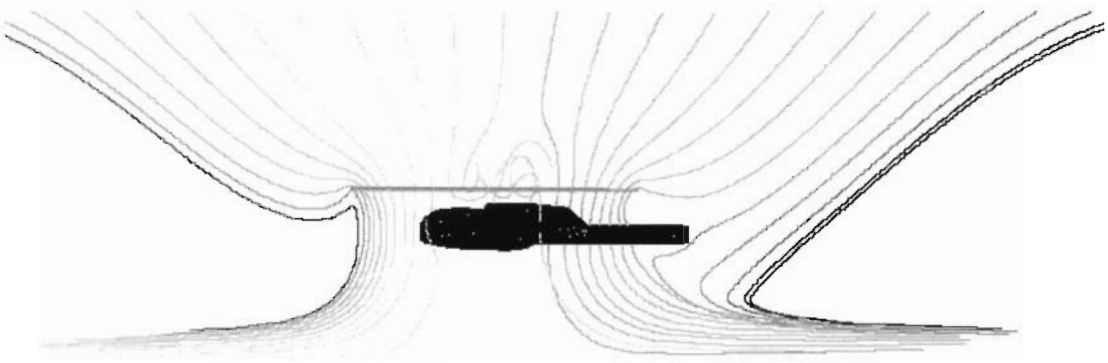

Figure 7-24: Particle pathlines, coloured according to particle, released within the longitudinal centre-plane of the rotor

7.5.4 Take-off

During take-off, the interaction between rotor, fuselage and ground is extremely complex. In Figure 7-25, contours of static pressure on the fuselage surface show elevated pressures caused by the downwash, both directly from the rotor, and indirectly via the ground. Air static pressure contours, displayed in Figure 7-26 on the helicopter longitudinal centre-plane, also show the higher pressures below the rotor being reflected by the ground-plane.

Figures 7-27 and 7-28 display velocity magnitude contours in the helicopter external flow-field. The effects of vortices created near the rotor hub are clearly seen, with Figure 7-29 demonstrating strong flow re-circulation in this region.

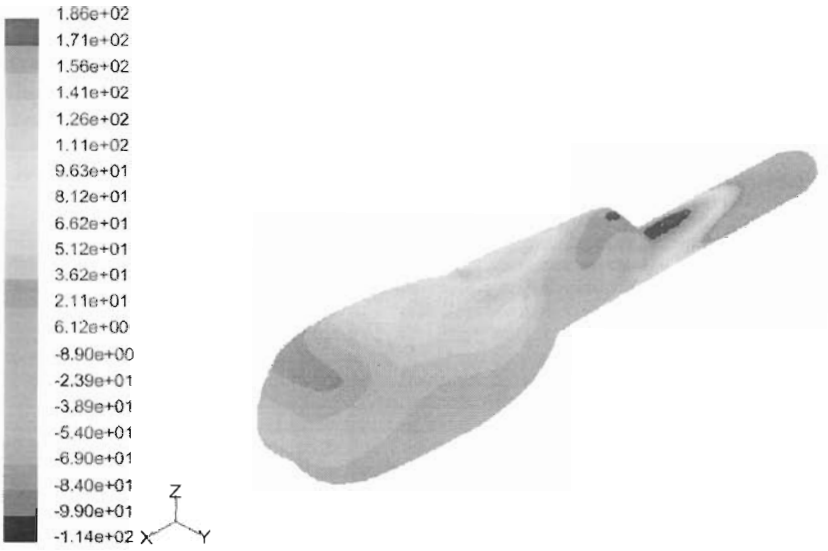

Figure 7-25: Contours of static pressure over the helicopter fuselage surface (Pa)

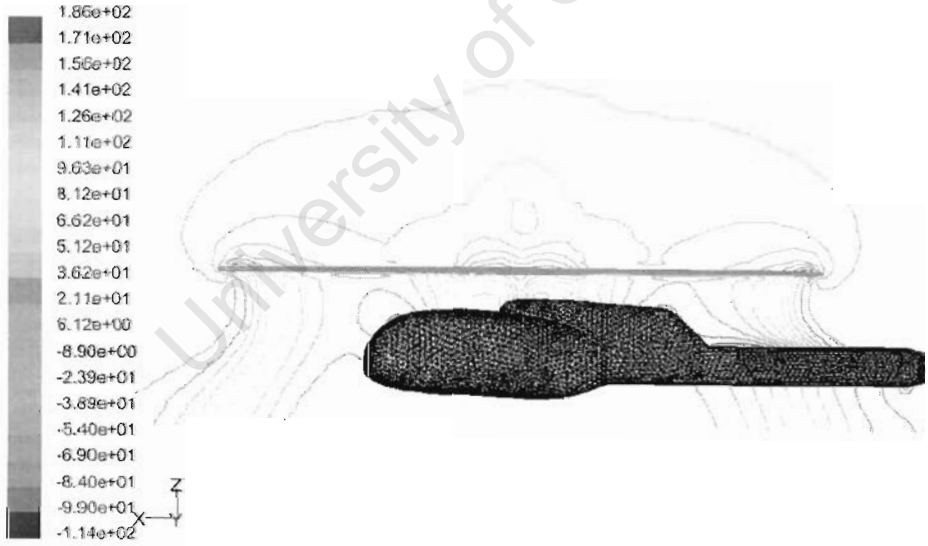

Figure 7-26: Contours of static pressure surrounding the helicopter, shown on the helicopter longitudinal centre-plane (Pa)

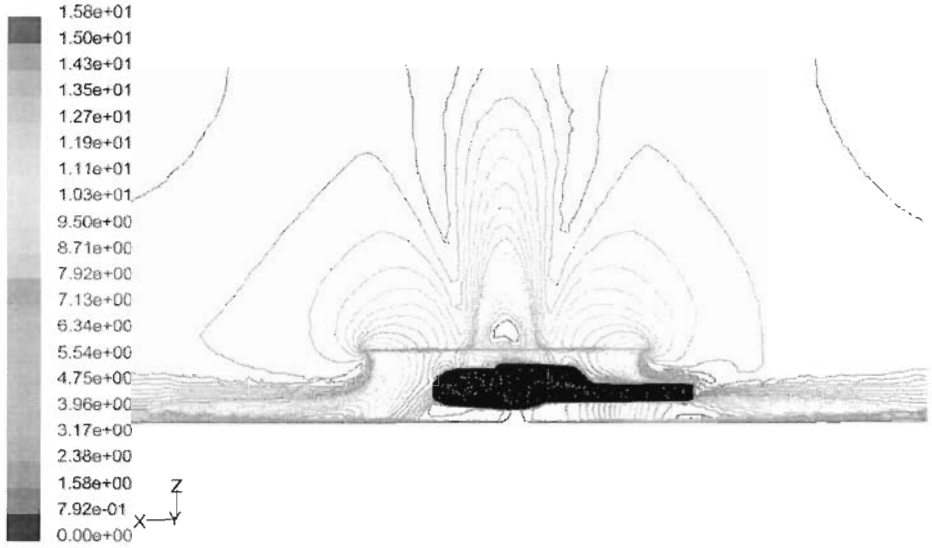

Figure 7-27: Contours of velocity magnitude surrounding the helicopter, shown on the helicopter longitudinal centre-plane (m/s)

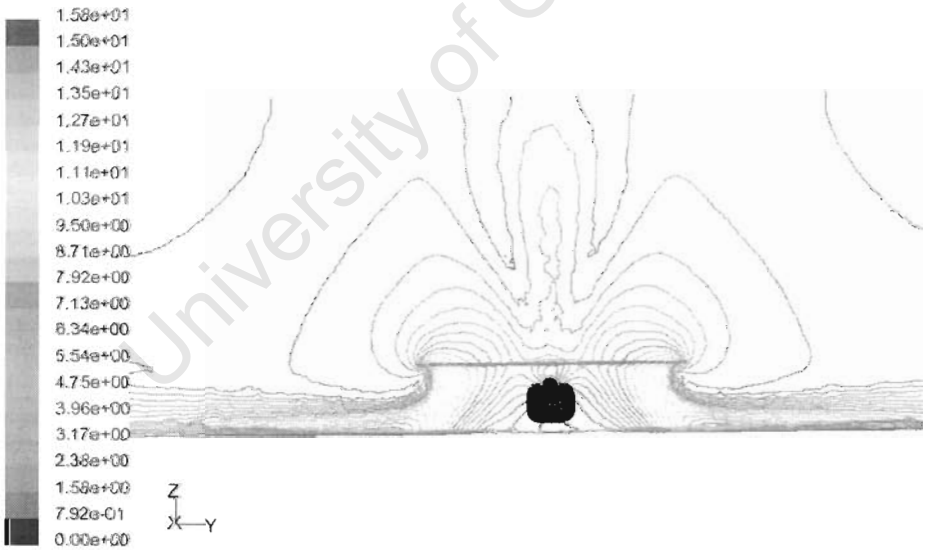

Figure 7-28: Contours of velocity magnitude surrounding the helicopter, shown on the rotor transverse centre-plane (m/s)

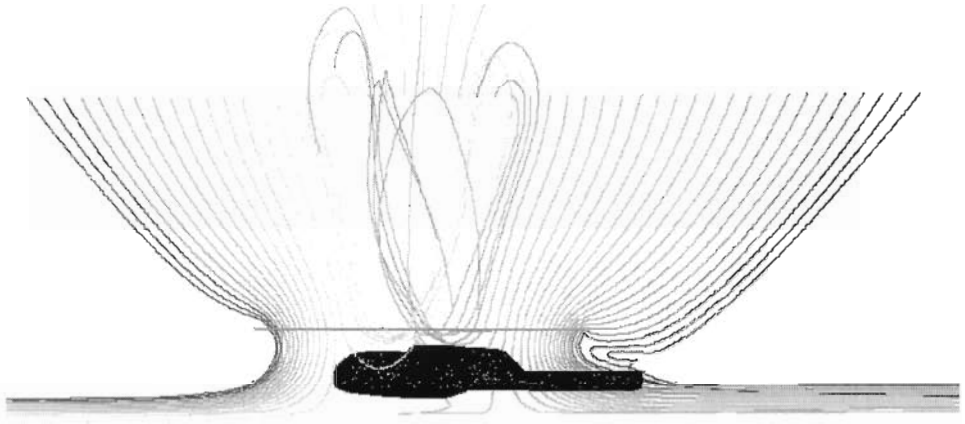

Figure 7-29: Particle pathlines, coloured according to particle, released within the transverse centre-plane of the rotor

7.5.5 Vertical ascent

Ascent velocities of 2 and 4m/s were simulated, with results obtained for the helicopter climbing at 4m/s shown in figures 7-30 and 7-31.

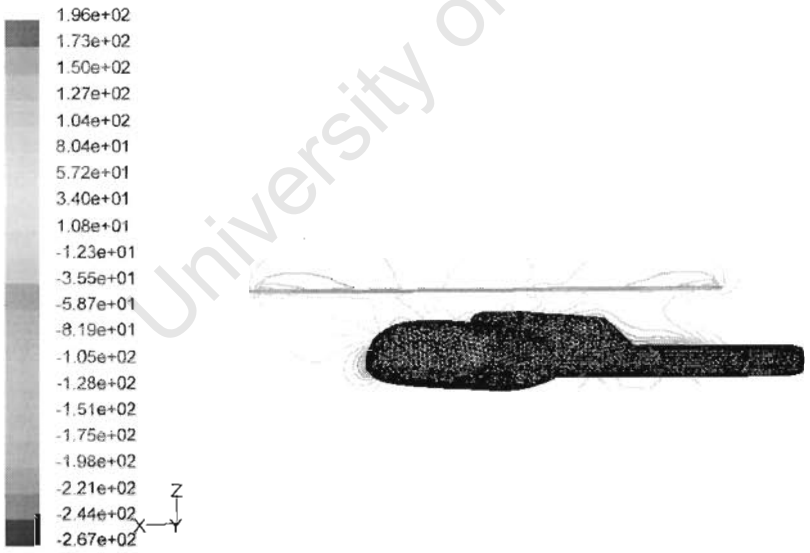

Figure 7-30: Contours of static pressure surrounding the helicopter, shown on the helicopter longitudinal centre-plane (Pa)

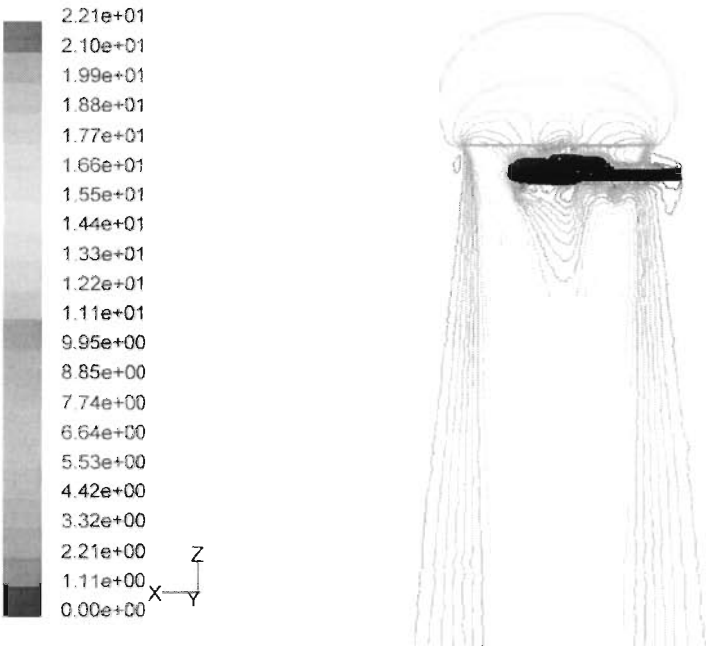

Figure 7-31: Contours of velocity magnitude surrounding the helicopter, shown on the helicopter longitudinal centre-plane (m/s)

7.5.6 Forward flight

With the helicopter in forward flight, the main rotor is subjected to proportionately large off-axis flow components. In addition, the rotor's rotation relative to the free-stream may result in reversed flow over the inboard sections of the retreating blades, particularly at high advance ratios. These factors, combined with the interactions between the rotor wake and fuselage, make forward flight an extremely complex aerodynamic problem to model.

In validating the rotor model, the accuracy and numerical stability of the code was demonstrated for the B-fan in chapters 5 and 6 of this report. In the current application as an helicopter rotor, the model again proved to be numerically stable for a wide range of off-axis upstream flow conditions. Advance ratios between 0.01 and 0.15 were simulated, with results using an advance ratio of 0.05 given graphically below.

In figures 7-32 and 7-33, static pressure contours are given over the surface of the CIRSTEL fuselage. Contours of velocity magnitude around the helicopter are shown in Figure 7-34, while the path-lines in figures 7-35, 7-36 and 7-37 demonstrate the flow

characteristics of the rotor-wake. The vortices created by interactions between the rotor blades and the free-stream are clearly evident in figures 7-35 and 7-36. Figure 7-37 shows the helicopter fuselage almost entirely submerged in the rotor wake.

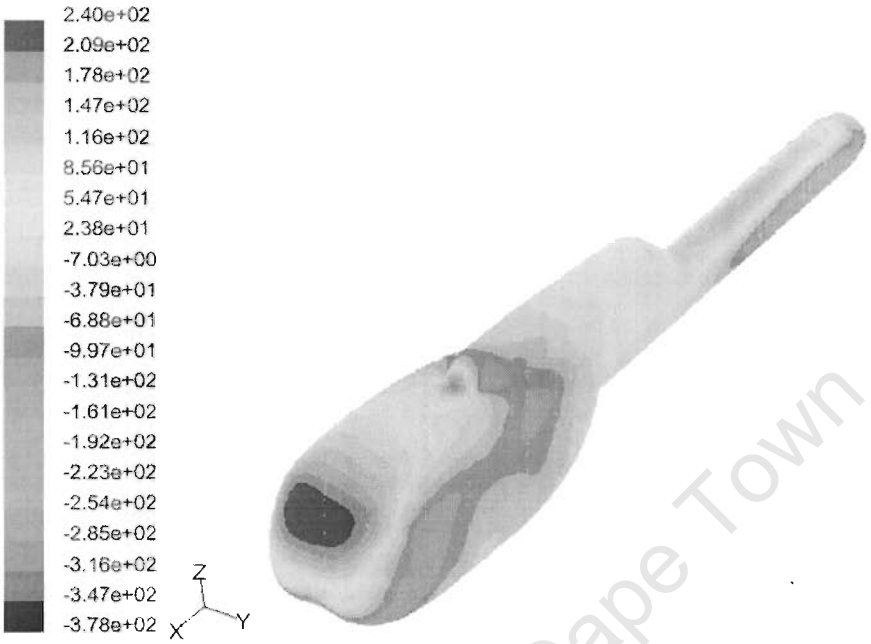

Figure 7-32: Contours of static pressure on the helicopter fuselage surface (Pa), $\mu = 0.05$

Figure 7-33: Side and Top views of fuselage surface static pressure contours (Pa) , $\mu = 0.05$

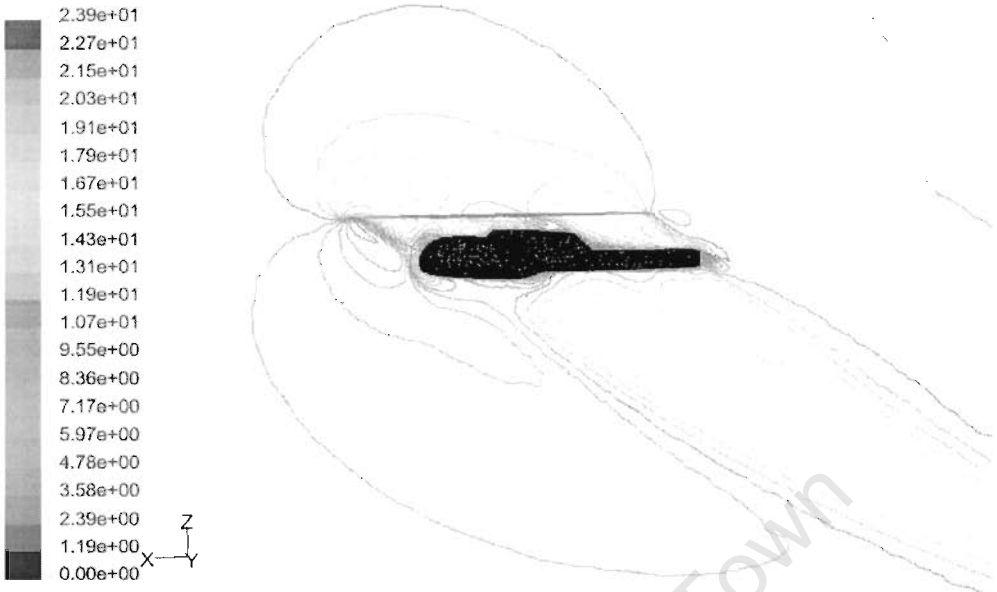

Figure 7-34: Contours of velocity magnitude surrounding the helicopter, shown on the rotor longitudinal centre-plane (m/s) , $\mu = 0.05$

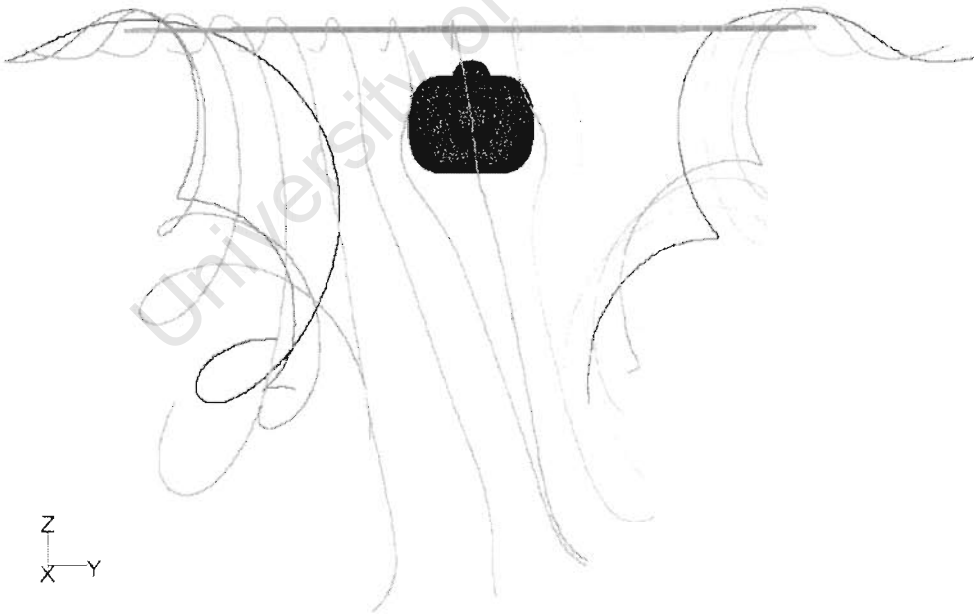

Figure 7-35: Particle pathlines coloured according to particle, $\mu = 0.05$

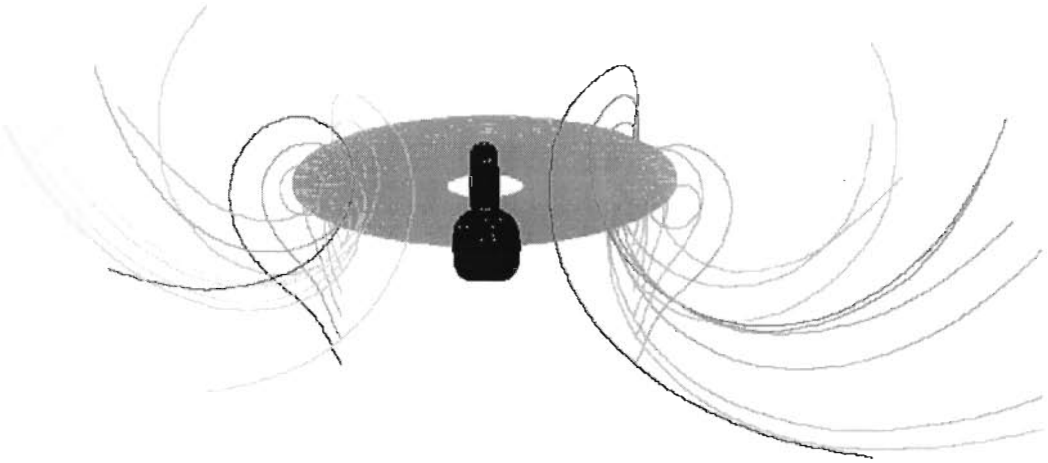

Figure 7-36: Particle pathlines coloured according to particle, $\mu = 0.05$

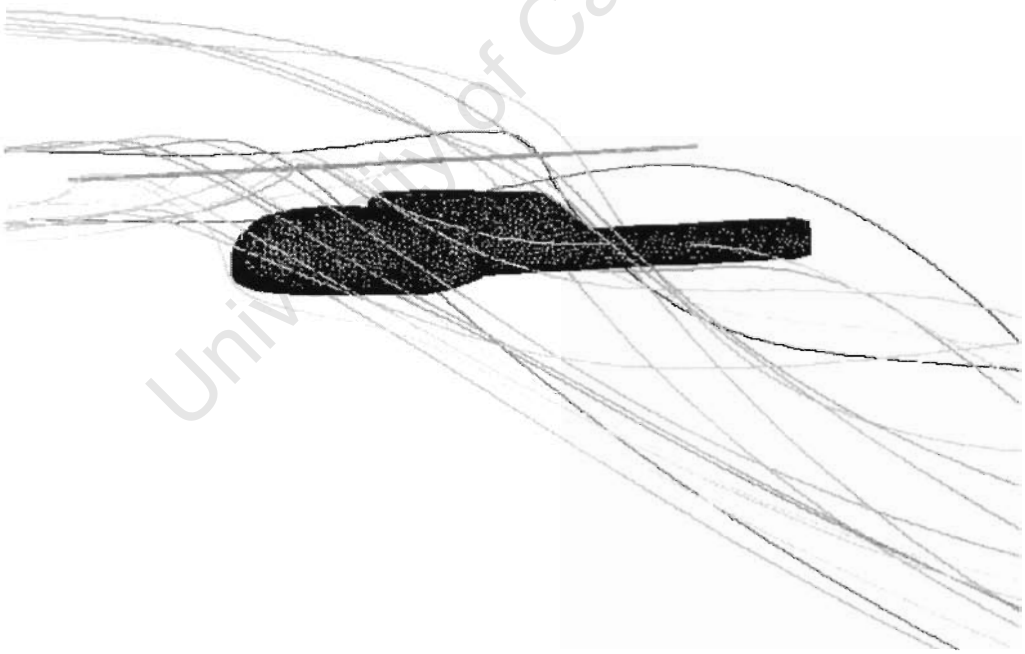

Figure 7-37: Particle pathlines coloured according to particle, $\mu = 0.05$

8 CONCLUSIONS AND RECOMMENDATIONS

This report has presented the development, validation and application of a numerical rotor model, developed for use in simulations of an helicopter exterior flow-field. The report has demonstrated the suitability of using the rotor model for analysis of flow-fields in the vicinity of a fan or rotor, including helicopter flow-fields where the rotor downwash is of aerodynamic importance.

In Chapter 1, an overview was given of some past and present modeling techniques used in the analysis of rotary-wing flow-fields. A numerical modeling methodology was selected, based on a combination of actuator disk and blade element theories, with the influence of the rotor being applied through the use of momentum source terms in the governing flow equations. Chapter 2 presented a mathematical description of this methodology, which was implemented through the use of user-defined functions, written in the C programming language, in the commercially available CFD code, *Fluent*.

The numerical modeling strategy for validating the rotor model was described in Chapter 3. This included a description of the governing equations, the discretisation practices and boundary conditions used, and the computational grid. Chapter 4 briefly described the sources of experimental fan-data used for validation purposes in this investigation.

The successful validation of the rotor model was described in chapters 5 and 6, in which the numerical results were presented and discussed, including results for analyses with axially aligned and off-axis upstream flow inlets. The measured fan parameters used in the validation process were fan static pressure rise, fan power consumption, and fan static efficiency, in accordance with BS 848 [20]. In general, the rotor model was demonstrated to predict fan characteristic trends consistently over the range of flow-rates and fan geometries tested, for both axial and off-axis upstream flow conditions. Numerical values for the fan static efficiency were in excellent agreement with the physical data, while fan power consumption and fan static efficiency were under and over-predicted respectively.

Based on the successful validation of the numerical rotor model, the code was used to model the exterior flow-field of the CIRSTEL helicopter. Chapter 7 described the integration of the rotor model with the CIRSTEL fuselage, presenting graphic representations of the flow-field solution. The interactions between rotor downwash, fuselage, and the ground, were successfully captured by the numerical solution.

It is recommended that this rotor model fulfills the aims of this investigation, and may be suitably applied in analyses involving the effects of a fan or rotor on the surrounding flow-field. This would include the analysis of helicopter external flow-fields.

List of References

[1] Von Mises, R. *Theory of flight*, McGraw-Hill Book Company Inc., London, 1945.

[2] Rajagopalan, RG, Mathur, SJ. Three dimensional analysis of a rotor in forward flight. *J. Am. Helicopter Soc.* 1993; **38**: pp14-25.

[3] Le Bouar, G, Costes, M, Leroy-Chesneau, A, Devinant, P. Numerical simulations of unsteady aerodynamics of helicopter rotor in manoeuvring flight conditions. *Aerospace Science and Tech.* 2004; **8**: pp11-25.

[4] Tadghighi, H. Simulation of rotor-body interactional aerodynamics: an unsteady rotor source distributed disk model. *Proceedings of the Am. Helicopter Soc., 57th Annual Forum, Washington, DC.* 2001.

[5] Fejtek, I, Roberts, L. Navier-Stokes computation of wing/rotor interaction for a tilt rotor in hover. *AIAA J.* 1992; **30**(11): pp2595-2603.

[6] Chaffin, MS, Berry, JD, Navier-Stokes simulation of a rotor using a distributed pressure disk method. *Proceedings of the Am. Helicopter Soc., 51st Annual Forum, Fort Worth, TX.* 1995.

[7] Lee, JK, Kwon, OJ. Predicting aerodynamic rotor-fuselage interactions by using unstructured meshes. *Trans Japan Soc. Aero. Space Sci.* 2002; **44**(146): pp208-216.

[8] Combes, JF, Marie, L. Numerical modelling of the flow in a cross-flow fan. *Fluid Machinery* 1994; **195**: pp29-34.

[9] Pericleous, KA, Patel, MK. The modelling of tangential and axial agitators in chemical reactors. *PhysicoChemical Hydrodynamics* 1986; **8**(2): pp105-123.

[10] Schetz, JA, Pelletier, D, Mallory, DA. Experimental and numerical investigation of a propeller with three-dimensional inflow. *J. Propulsion* 1988; **4**(4): pp341-349.

[11] Thiart, GD, von Backström, TW. Numerical simulation of the flow field near an axial flow fan operating under distorted inflow conditions. *J. Wind Engineering and Industrial Aerodynamics* 1993; **45**: pp189-214.

[12] Löstedt, P. Accuracy of a propeller model in inviscid flow. *J. Aircraft* 1995; **32**(6): pp1312-1321.

[13] Meyer, CJ, Kröger, DG. Numerical simulation of the flow field in the vicinity of an axial flow fan. *International J. Numer. Meth. Fluids* 2001; **36**: pp947-969.

[14] Le Chuiton, F. Actuator disk modelling for helicopter rotors. *Aerospace Science and Tech.* 2003.

[15] Hoerner, SF, Borst, HV. *Fluid-dynamic lift*, Published by Mrs. L.A. Hoerner, 1975.

[16] Hoerner, SF. *Fluid-dynamic drag*, Published by the author, 1965.

[17] White, FM. *Viscous Fluid Flow*, McGraw-Hill Book Company Inc., 1991.

[18] Bruneau PRP. The design of a single rotor axial flow fan for cooling tower application. Thesis for the degree of Master of Engineering (Mechanical), University of Stellenbosch, South Africa, 1994

[19] Stinnes, WH, von Backström, TW, Effect of cross-flow on the performance of air-cooled heat exchanger fans. *Applied Thermal Engineering* 2002; **22**: pp1403-1415.

[20] British Standards Institution, Part 1: Methods of testing performance. *Fans for general purposes BS 848* 1980.

[21] Heise, R. Implementation of a two-stream fan in the CIRSTEL helicopter. *Dissertation for the degree of Master of Science (Mechanical Engineering) at the University of Stellenbosch, South Africa.* 2002.

[22] Leonard, B. P. Mokhtari, S, ULTRA-SHARP Non-oscillatory Convection Schemes for High-Speed Steady Multidimensional Flow, NASA TM 1-2568 (ICOMP-90-12), NASA Lewis Research Center, 1990.

APPENDIX A:

Analysis and discussion of the modeling methodology for determining the relative velocity vector

As described in the modelling methodology for this rotor model, the flow velocity vector used by the code is obtained as an average of the solver flow velocity at specified points upstream and downstream of the actuator disk. This technique is used to determine an appropriate relative velocity vector for use with the airfoil tables. In most rotor codes however, the relative velocity vector is obtained from the solver at a position within the actuator disk itself. There are several fundamental problems associated with this approach, which are highlighted in this section. Also in this section, a comparison is made between results generated with the current rotor model using an upstream-downstream averaged velocity, and those generated using the same model, but reading the relative velocity vector within the actuator disk.

The fundamental problem with reading the velocity vector within the actuator disk relates to the use of 2-D airfoil tables to calculate the lift and drag coefficients. This lift and drag data is generated relative to a free-stream velocity measured well away from the airfoil itself. Logically, a similar approach should be taken for the reverse process, by which blade forces are obtained from the airfoil data. In the case of a rotating blade however, it is not good enough to merely obtain a velocity vector far upstream of the actuator disk, since the induced swirl at the fan must change the velocities significantly. It has been found that taking an average of upstream and downstream velocity vectors yields excellent results.

The axial position at which the velocity vectors are obtained is also critical, affecting both the numerical stability of the model, and the accuracy of the results. Through a process of trial and error, it was found that increasing the axial distance between the position at which velocity was measured, and the actuator disk, led to increased stability, while compromising the accuracy of the results. As this distance tended towards zero, the accuracy of the results again decreased, and was accompanied by increasing numerical instability. A compromise was eventually found, with the velocity readings taken at an axial position 4.5 times the actuator disk thickness from

the disk centre. This position was found to be more critical for the upstream velocity reading.

With the actuator disk geometry correctly adjusted, it was found that in simulations with an averaged velocity vector, numerical stability was extremely high, for a wide range of grid geometries. The results are the subject of this validation report. In contrast, on attempting to use the velocity vector from within the actuator disk, numerical stability problems were experienced in the region of the actuator disk. Results were only obtained by gradually increasing the momentum relaxation factor from 0.2 until the stability threshold was reached, typically 0.5 for axial inflow conditions. Simulations for off-axis upstream flows at 45° were attempted, but again numerical instabilities prevented a full investigation.

For the axial upstream flow condition, with an annular outlet duct, results were obtained using the flow velocities within the actuator disk, and are displayed in the figures below. The results are poor, being under predicted by as much as 50% in the case of fan static pressure rise. Fan power consumption and fan static efficiency are also well under-predicted.

From the results presented below, it is clear that the theoretical reasons for not reading the flow-field velocity within the actuator disk are supported by the numerical analysis. The upstream-downstream velocity-averaging technique used by the current model has proven to be numerically more robust, as well as producing more accurate results.

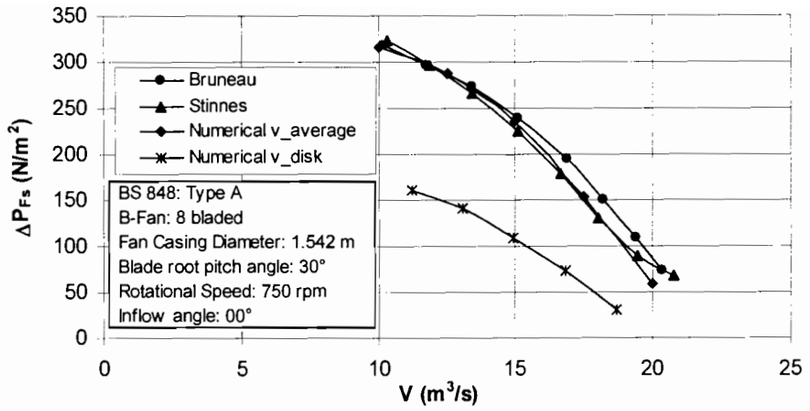

Figure a: Fan static pressure rise vs. Volume flow rate for a blade root pitch angle of 30°

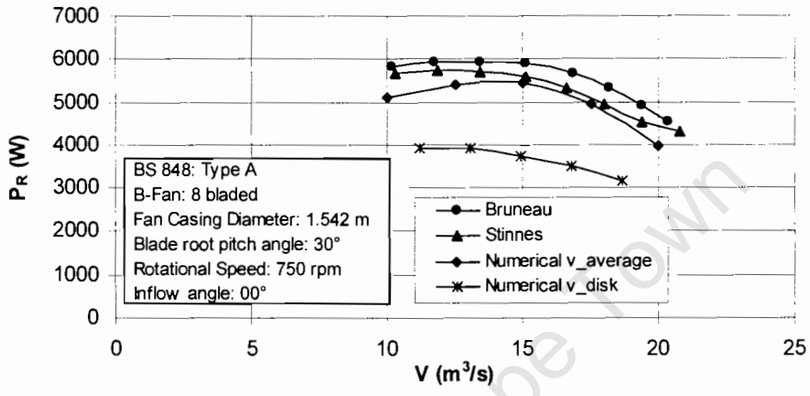

Figure b: Fan power consumption vs. Volume flow rate for a blade root pitch angle of 30°

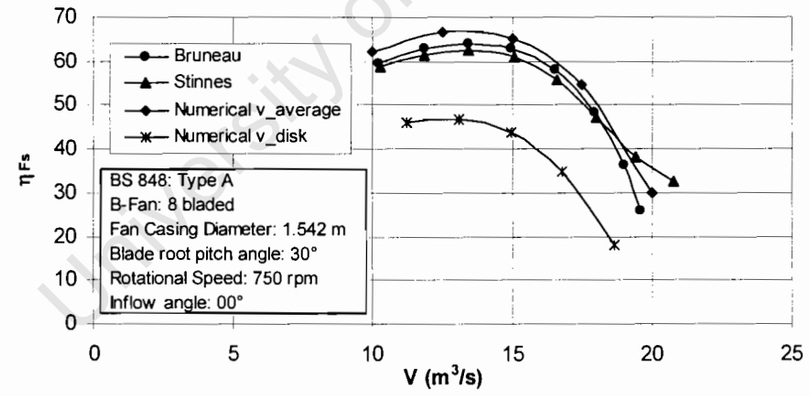

Figure c: Fan static efficiency vs. Volume flow rate for a blade root pitch angle of 30°

APPENDIX B:

Numerical results presented in tabular form

The numerical results generated during the validation process are given below in tabular form. These values correspond to simulations run for the b-fan, with characteristics given in Table 2 of this report, and repeated here for convenience. Air density was nominally set at 1.2 kg/m^3.

Table a: B-Fan characteristics

Fan Casing Diameter (mm)	No. of blades	Rotational Speed (rpm)	Hub-to-tip diameter ratio, d_{FH}/d_{FC}	Blade profile	Root stagger angle (°)
1542	8	750	0.40	NASA-LS	28-32

Table b: Numerical results for the annular outlet duct with an axial inlet

Geometry 1: Annular Outlet Duct with Axial Inlet				
Blade root pitch angle	V	ΔP_{Fs}	P_R	η_{Fs}
	m^3/s	N/m^2	W	-
29°	10.000	311.51	4787.8	65.063
	12.500	273.55	4992.3	68.493
	15.000	209.52	4846.4	64.847
	17.500	119.58	4197.2	49.859
30°	10.000	316.94	5098.7	62.162
	12.500	287.64	5403.8	66.535
	15.000	235.51	5436.6	64.979
	17.500	154.36	4936.3	54.722
	20.000	59.16	3971.0	29.796
31°	12.500	297.56	5803.6	64.088
	15.000	254.53	5951.5	64.152
	17.500	180.88	5549.7	57.037
	20.000	93.64	4838.2	38.707
32°	12.500	305.26	6198.0	61.565
	15.000	267.79	6481.9	61.970
	17.500	209.57	6288.2	58.324
	20.000	127.41	5651.0	45.093

Table c: Numerical results for the atmospheric outlet with an axial inlet

Geometry 2: Atmospheric Outlet Duct with Axial Inlet				
Blade root pitch angle	V	ΔP_{Fs}	P_R	η_{Fs}
	m^3/s	N/m^2	W	-
30°	12.500	284.94	5302.6	67.171
	15.000	238.89	5300.3	67.607
	17.500	164.11	4865.7	59.022
	20.000	66.66	3876.0	34.397
31°	12.500	299.55	5696.1	65.735
	15.000	258.38	5793.7	66.896
	17.500	197.61	5561.7	62.178
	20.000	104.80	4725.2	44.357

Table d: Numerical results for the atmospheric outlet with an off-axis inlet

Geometry 3: Atmospheric Outlet Duct with Off-Axis Inlet					
Blade root pitch angle	V	ΔP_{Fs}	P_R	η_{Fs}	Fan Inlet Angle
	m^3/s	N/m^2	W	-	
30°	11.205	304.51	5189.0	65.754	0°
	12.500	284.94	5302.6	67.171	
	15.000	238.89	5300.3	67.607	
	17.500	164.11	4865.7	59.022	
	18.675	121.47	4453.1	50.940	
	11.205	301.44	5166.4	65.377	14°
	13.072	277.36	5312.1	68.255	
	14.940	242.20	5311.9	68.120	
	16.807	186.14	5025.1	62.257	
	18.675	115.91	4429.5	48.866	
	11.205	291.27	5139.9	63.497	27°
	13.072	269.63	5303.8	66.456	
	14.940	226.56	5244.1	64.544	
	16.807	173.42	4985.5	58.466	
	18.675	102.29	4397.4	43.439	
	11.205	275.50	5132.4	60.148	45°
	13.072	253.13	5313.1	62.281	
	14.940	201.15	5240.0	57.349	
	16.807	136.98	4938.7	46.618	
	18.675	58.83	4379.3	25.085	
31°	11.205	306.71	5521.1	62.245	0°
	13.072	299.55	5696.1	65.735	
	14.940	258.38	5793.7	66.896	
	16.807	197.61	5561.7	62.178	

31°	18.675	155.73	5230.7	55.599	0°
	11.205	305.99	5511.9	62.203	
	13.072	287.48	5720.7	65.693	
	14.940	257.34	5793.4	66.362	14°
	16.807	213.76	5665.7	63.412	
	18.675	149.94	5198.9	53.860	
	11.205	295.36	5490.0	60.282	
	13.072	277.86	5697.2	63.757	
	14.940	250.32	5793.1	64.555	27°
	16.807	199.35	5611.3	59.711	
	18.675	135.67	5164.2	49.061	
	11.205	279.36	5487.4	57.044	
	13.072	260.70	5704.9	59.739	
	14.940	219.87	5745.4	57.174	45°
	16.807	165.37	5578.3	49.828	
	18.675	93.76	5146.7	34.020	